Exponentially Tapered Bimorph Piezoelectric Vibration Energy Harvester

Submitted By
Mikkel F. Reske-Nielsen

IN PARTIAL FULFILLMENT OF THE REQUIREMENTS FOR THE DEGREE

OF MASTERS OF SCIENCE IN MECHANICAL ENGINEERING

TUFTS UNIVERSITY

School of Engineering

Medford, MA 02155

November 2012

Committee Members

Professor Robert D. White, Department of Mechanical Engineering, Tufts University

Professor Jason Rife, Department of Mechanical Engineering, Tufts University

Professor Masoud Sanayei, Department of Civil & Environmental Engineering, Tufts University

Abstract

This thesis examines the effectiveness of an exponentially tapered piezoelectric plate for use as a vibration energy harvester (VEH). Typically piezoelectric energy harvesters have been designed as cantilever beams or "cymbal" type structures. For these devices there is a known resonant frequency at which displacement is maximized to produce maximum power. While this can produce good results for applications in which a device vibrates at a specific frequency, many environmental vibration sources are wide-band and random.

The exponentially tapered plate investigated in this work was 55.88mm in length and tapered exponentially from an initial width of 9.4mm to a final width of 71.12mm. The effectiveness of this type of structure was investigated to determine how well this system functioned as a broadband vibration energy harvester. Experimental and computational analyses demonstrated the presence of an evanescent cut-off frequency of approximately 3800 Hz below which very little energy is transferred from the input into the plate. The result of this is very inefficient power conversion at or below this cut-off frequency. Since this is a critical feature of this type of energy harvester this structure will only be effective at higher frequencies above the cut-off.

The mounting assembly design itself was shown to accurately model an exponentially tapered plate using a square PZT plate rather than having to have the PZT custom milled to the desired shape. This greatly reduces the cost of the materials used and should be considered for use in future research related to exponentially tapered plates. In addition the experimental results showed that as the frequency of the input is increased, the amount of energy transmitted around the mounting structure and therefore into the plate from the sides increased. This makes the mounting structure more suitable for low frequency experimentation, below 3000Hz.

Acknowledgements

I would mainly like to thank my advisor Professor Robert White for agreeing to advise me on this work although it was unrelated to most of the other research he is involved with. His guidance through this process has been invaluable and I'm sure that it would not have been completed without his constant encouragement and advice.

I would also like to thank my other committee members Professor Jason Rife and Professor Masoud Sanayei. Thank you both for taking the time to be a part of this thesis work.

Alex, you deserve a special mention for all the support and understanding you have provided during this busy time in my life. Your reminders that there is more to life than work have helped me to balance my work with some well deserved time off that allowed me to complete this work. Without you this task would have been all the more difficult.

Table of Contents

Table of Figures

Table of Tables

Chapter 1

INTRODUCTION, CONTRIBUTIONS AND BACKGROUND

1.1 INTRODUCTION

The objective of this thesis was to examine the vibration mechanics of an exponentially tapered bimorph piezoelectric plate (Figure 6) with the goal of determining if this shape could be used to create a piezoelectric energy harvester with improved frequency response for broadband vibration, rather than being limited to a single tuned frequency (e.g. [1-4]). Since in many cases piezoelectric vibration energy harvesters (VEHs) are tuned to a specific frequency, but environmental vibration is not always narrow band, it would beneficial in many applications to have a device capable of generating a strong response at a number of frequencies along its length. This is similar to the frequency response of the mammalian cochlea, so inspiration was taken for the structure from the mechanics of the organ [5, 6]. Being able to use ambient vibrations to power wireless sensors is an intriguing idea and there is a large market potential as the overall wireless sensor market continues to grow. Microcontrollers and RF radio components continue to become more affordable as power requirements are reduced which is opening doors for new applications of energy harvesting technologies [7].

With this in mind there were two goals in conducting this research. The primary goal was to design a method to successfully evaluate the energy harvesting potential of an exponentially tapered plate since to the author's knowledge no experimental research has been done in this area. Some computational work on the development of "An electromechanical finite element model for piezoelectric energy harvester plates" was presented by De Marqui Junior, Erturk and Inman in 2009 [8]. The secondary goal was to present a comparison of the experimental results to existing finite element models for both a

purely structural model and a coupled piezoelectric finite element model. The goal here is to validate

the modeling approaches for potential future work in structural optimization. Several other shapes have

been investigated in literature (Table 1) but none were found that researched the use of exponentially

tapered plates.

Author	Piezoelectric Configuration investigated
Mateu and Moll, 2005 [9]	Rectangular and triangular cantilever
Roundy *et al, 2005* [10]	Trapezoidal cantilever
Baker *et a, 2005* [11]	Rectangular and trapezoidal cantilever
Mossi *et al, 2005* [12]	Unimorph pre-stressed bender
Danak *et al,2003 [13]*	Initially curved PZT unimorph
Yoon *et al, 2005* [14]	Initially curved PZT unimorph
Ericka *et al, 2005 [15]*	Unimorph circular membrane
Kim *et al, 2005* [16]	Clamped circular plates
Kim *et al, 2004* [17]	Piezoelectric 'cymbal'
Adhikari *et al, 2009* [18]	Stacked piezoelectric
Erturk *et al, 2009* [1]	Cantilever bimorph
Kim *et al, 2011* [19]	Unimorph and bimorph cantilever beam with distributed tip mass

Table 1 Examples of shapes of piezoelectric energy harvesters from literature

The first step was to develop a simple numerical model using fundamental plate theory and

modifying it to account for the exponentially tapered shape of the device, without accounting for

piezoelectric coupling. These results were found to be well matched to the structural finite element

model from COMSOL®. The finite element model was then expanded to include piezoelectric coupling,

again using COMSOL®. It was shown that the piezoelectric coupling has a significant effect on the

resonant frequencies of the device.

This was followed by the design and manufacture of the mounting assembly that allowed a

rectangular piezoelectric plate to be evaluated as an exponentially tapered plate. The structure was

fixed on two sides with a base excitation applied to the narrow end, in order to compare the frequency response to a similarly shaped cochlea model developed and analyzed by White [20]. The data gathered was then compared to the results obtained from the analysis of various cantilever type bimorph devices by other authors.

It was determined that in the configuration that was evaluated there was a severe attenuation of the power transferred from the base excitation through the device at low frequencies, limiting the usefulness of this device as an energy harvester. The evanescent effect observed prevented the observation of cochlear like mechanics in the tapered plate and limited the overall power output of the device. Although the power output from the device was lower than desired this was determined to be due to a low frequency evanescent cut-off that occurs using this configuration. This effect was not considered in early stages of the design. This provides a good lesson for future work with this type of device. In order to achieve cochlear like response, a coupling fluid must be added.

In addition, modeling methods were validated at low frequencies for a stiff support structure and the manufacturing methods and experimental techniques for mimicking exponentially tapered PZT plates were demonstrated successfully. Finally, methods for determining optimal load impedances were explored and demonstrated successfully.

1.2 Contributions

A great deal of research has been done in the field of piezoelectric energy harvesters, however the vast majority has been done on cantilever beams in various configurations. The focus of this work was to test a new and novel shape to see how it would compare to existing designs. No other work has considered the idea that the frequency analyzing characteristics of the cochlear might be used to "filter"

input vibrations and allow a single energy harvesting device to generate power consistently over a wide range of frequencies.

The demonstration of a low frequency evanescent cut-off frequency provides a useful result in that future researchers will be aware of this phenomenon and can factor it into their designs. This provides a starting point for future research that might consider using more flexible and less brittle piezopolymer materials [21] in a similar type of structure with the same goal of duplicating the frequency response characteristics of the mammalian cochlea. These types of materials may have properties that could avoid the evanescent wave issues that limited the success of the experiments presented in this work. In addition, in order to achieve truly cochlear-like characteristics, it is critical to include a second coupling medium analogous to the fluid that fills the cochlear ducts.

1.3 Background

1.3.1 Introduction to Piezoelectricity

Piezoelectric energy harvester technologies are small energy harvesters which can generate power in the µW–mW range. The focus of this type of device is not to replace renewable energy sources such as wind or solar but rather as an alternative to the conventional small scale chemical battery. They are of particular interest in the field of wireless sensors since unlike a conventional battery where power comes from a chemical source vibration energy harvesters utilize ambient vibrations to generate power. Piezoelectricity itself is a property of certain crystalline materials such as quartz, Rochelle salt and tourmaline and more modern materials such as PZT, AIN and ZnO [22].

Piezoelectricity was first discovered over 130 years ago by the Curie brothers [23] , but it was first postulated by Coulomb who theorized that it might be possible to create electricity through applied pressure. However it was not until some 75 years after his death that piezoelectricity would be formally discovered by Jacques and Pierre Curie in 1881 [22]. Other experiments had been done, but theirs was

4

the first in which the charges produced could not be attributed to friction or contact electricity [24]. The first real world application of the piezoelectric effect did not come until Langevin applied piezoelectric transducers to the problem of detecting submarines during World War I [23]. The work that he did yielded promising results however the technology was never applied in practice during the war [22]. Further applications were developed by Cady who used the piezoelectric effect to create crystal resonators that were used to stabilize oscillators in 1921 [25].

During the remainder of the 20th century the applications of the piezoelectric effect expanded greatly. These ranged from something as simple as a phonograph cartridge, to ultrasonic transducers that allow measurement of viscosity and elasticity in fluids and solids. During World War II a new class of materials known as ferroelectrics was developed which had piezoelectric constants many times greater than any natural materials, and directly led to the development of a lead zirconate titanate alloy, better known simply as PZT [26]. PZT is now a commonly used piezoceramic and also material used in this thesis. Typical modern applications of piezoelectric materials have been in sensor applications, where the charge output could be used to detect mechanical strains, for example accelerometers or microphones. In the late 1990s shunt damping, where the electrical output is used for damping rather than sensing, was developed [27]. This original vibration application was geared towards the reduction of vibrations due to the joule heating and therefore energy dissipation that occurs in the materials. This idea of shunt damping was further developed to be used for power harvesting, where rather than dissipating the energy generated, it is used to power another device. With the shrinking of integrated circuits less and less power is needed to operate electrical devices, and the relatively low power available from piezoelectric materials is now usable.

Since this early progress, the early and mid 20th century has seen a boom in research and development in the field of piezoelectric energy harvester systems. There are many ways in which

piezoelectric materials can be configured in order to try to extract the most power possible from the device; this includes varying the shape, material and electrode pattern, changing poling and stress directions, and tuning of devices to specific resonant [10-12, 16, 18].

In particular VEHs make use of the so-called "direct effect", in which an applied strain causes an electric field to be induced across the crystal. The inverse is also true whereby an applied electric field causes the crystals to deform. This is known as the converse effect. This bi-directional relationship is a result of the crystalline structure of piezoelectric materials. It is the result of an uneven charge distribution within the crystals of a piezoelectric material; thus when a mechanical strain is applied, polarization of the internal charge results in the generation of a measureable surface charge.

1.3.2   Cochlear Mechanics

Since this thesis is motivated by the frequency response characteristics of the mammalian cochlear it is useful to have some introductory knowledge on the mechanics of this natural acoustic sensor. The cochlea is a single part of a network of bones and membranes that together form the ear and allows us to interpret pressure variations in the environment as sound [28]. The cochlea itself serves to differentiate the frequencies of this sound. This is facilitated by the basilar membrane found inside of the cochlear. The basilar membrane varies in thickness, width and stiffness all along its length as it spirals through the cochlea as shown in Figure 1.
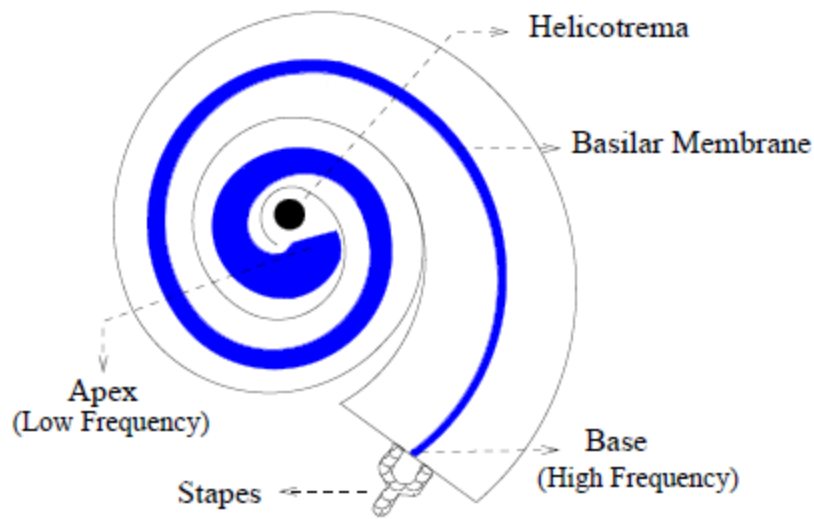
Figure 1 Simplified picture showing variable width basilar membrane traveling down the cochlear duct (Taken from [20] with permission)

The changing impedance of the basilar membrane means that high frequency sounds amplify motions near the base of the cochlea, because the basilar membrane is stiffer and has less effective mass there. Low frequency sounds have a greater effect near the apex since here it is more flexible and has greater effective mass [29]. In addition, the fluid in the ducts performs an important continuous coupling along the membrane, and complex mechanics and active cells in the Organ of Corti act to modify membrane motion. The wideband fitting is the characteristic that we are interested in, since the ability to induce motion in different parts of a device depending on frequency would allow the device to generate power at a number of frequencies rather than just a single one as with most existing cantilever energy harvesters. This frequency response is shown in Figure 2, which illustrates how as you move further from the base of the basilar membrane the resonant peak occurs at lower and lower frequencies. In this thesis the exponentially tapered plate provides an analogous situation where we have a higher stiffness at the narrow end which gradually decreases as we move away from the input.
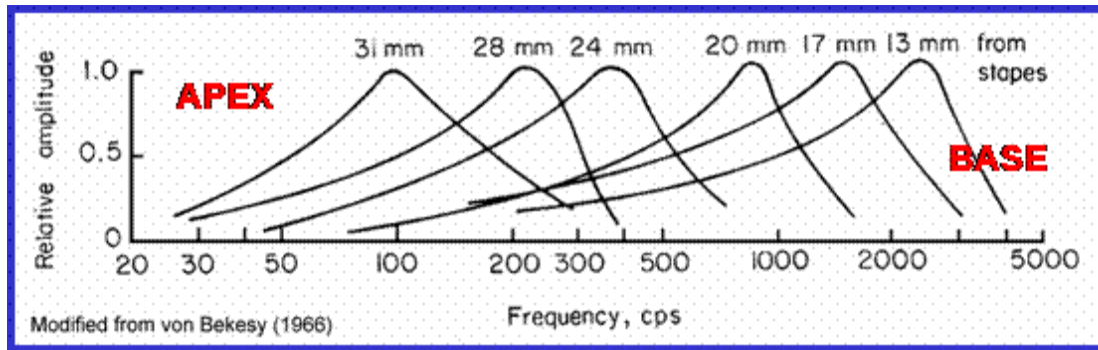
Figure 2 Frequency response at several distances from the stapes along the basilar membrane

1.3.3   Evanescent Waves

An evanescent wave is a near field standing wave that exhibits exponential decay with distance from the boundary at which it is formed. Evanescent waves became a very important factor in this work since this phenomenon directly influenced the ability to generate power using the structure under investigation. In this case we see an example of a low-frequency cut-off. The 1D artificial example of an anchored string shown in Figure 3 does a good job of explaining this phenomenon and can also be expanded to apply to waves in plates.
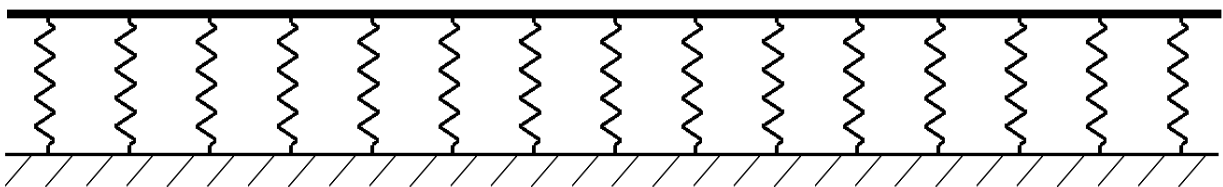
Figure 3 Anchored string in equilibrium position

We assume that the string is perfectly flexible but the springs apply a lateral stiffness to the string by virtue of the other end being attached to a parallel rigid anchoring. The springs are assumed to be

identical linear, uniformly spaced and close together. The return force added by the springs does not

require the string to be curved and acts equally at all wavelengths.

The stiffness added by the springs is defined as σ per unit length which applies an additional force

at each location. Adding this to the standard equation of motion for vibrating string the new equation of

motion of the string becomes:

$$\frac{\partial^2 \psi}{\partial t^2} \approx \frac{T}{\mu}\left(\frac{\partial^2 \psi}{\partial z^2}\right) - \left(\frac{\sigma}{\mu}\right)\psi \tag{1.1}$$

Where T is the tension in the string and μ is the mass per unit length, $\Psi(z,t)$ is the vertical

deflection of the string, t is time, and z is the coordinate along the string. We also apply the following

definitions:

$$c = \sqrt{\frac{T}{\mu}}$$
$$\omega_c \equiv \frac{\sigma}{\mu} \tag{1.2}$$

Where c is the wave speed and ω_c is the cut-off frequency. We can rewrite this equation to the
standard form known as the Klein-Gordon equation [30]:

$$\frac{\partial^2 \psi}{\partial t^2} = c^2 \left(\frac{\partial^2 \psi}{\partial z^2}\right) - \omega_c^2 \psi \tag{1.3}$$

From here we can find the dispersion relation that relates driving frequency, ω, with the wavenumber,
k :

$$\omega^2 = c^2 k^2 + \omega_c^2 \tag{1.4}$$

The resulting dispersion curve is plotted in Figure 4 where we can see the low frequency cut-off at
$\omega = \omega_c$.
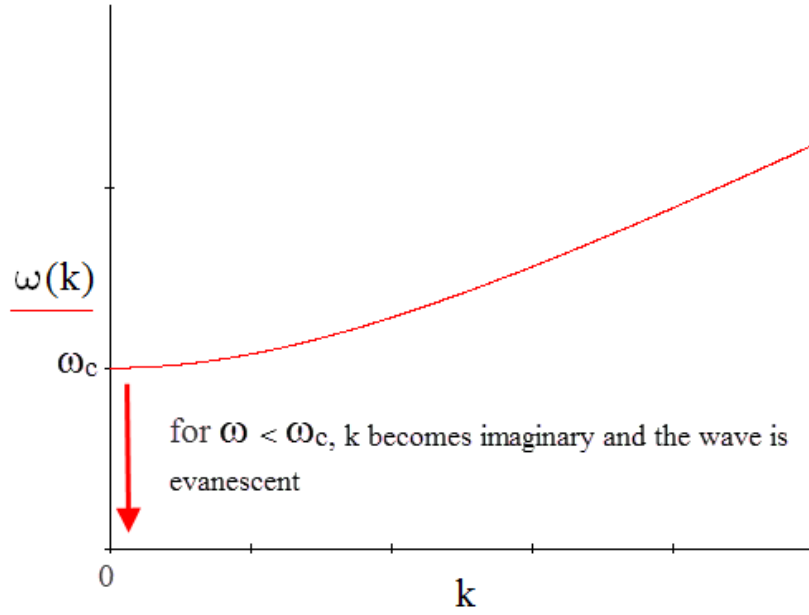
Figure 4 Dispersion curve for an anchored string

Note that the wave number is,

$$k = \frac{\sqrt{\left(\omega^2 - \omega_c^2\right)}}{c} \tag{1.5}$$

which will be imaginary if $\omega < \omega_c$. While the full derivation is too involved for inclusion in this work it

can be shown that when the wavevector becomes imaginary the solution to the wave equation

becomes:

$$\psi = e^{-\kappa z} \operatorname{Re}\left[De^{i\omega t} \right] \tag{1.6}$$

where κ is the magnitude of the imaginary part of the wavevector k. There are two key observations to

be made from this solution.

(1) The phase angle component does not depend on z, meaning that all points on the string vibrate

in phase with each other.

(2) The resulting shape of the string is now exponential and decays as we move along the string away from the driven end.

This is a qualitatively different response than is seen for $\omega > \omega_c$, where there will be travelling waves in the string. The resulting shape of the string is shown in Figure 5. And will be seen to be almost identical to what is seen in the numerical model, the FEA models and also in the experimental results.
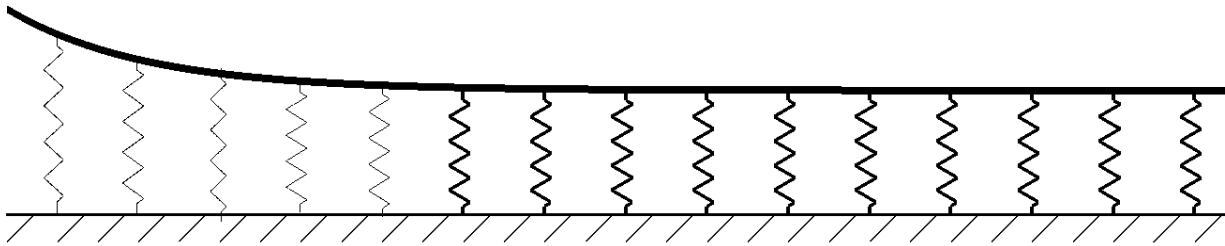
Figure 5 Evanescent wave on an anchored string

A similar type of response is observed in the tapered plate, at low frequencies the response is evanescent, and we only see travelling waves at higher frequencies above the cut-off frequency. This is actually different from the cochlea; in the cochlea the fluid coupling medium plays a strong role in the mechanics allowing propagating waves at low frequencies, and waves cut off and become evanescent only at higher frequencies on some parts of the basilar membrane.

Chapter 2   Structural Plate Model

Two methods have been used to develop a solution for the vibration response of the

exponentially tapered plate shown in Figure 6. The first is the finite difference method which is used to

obtain a numerical solution to the governing differential equation. The second is a finite element

analysis using COMSOL® that also incorporates the piezoelectric effect which has been omitted from the

finite difference solution for simplicity. This will be discussed further in the following FEA modeling

chapter.
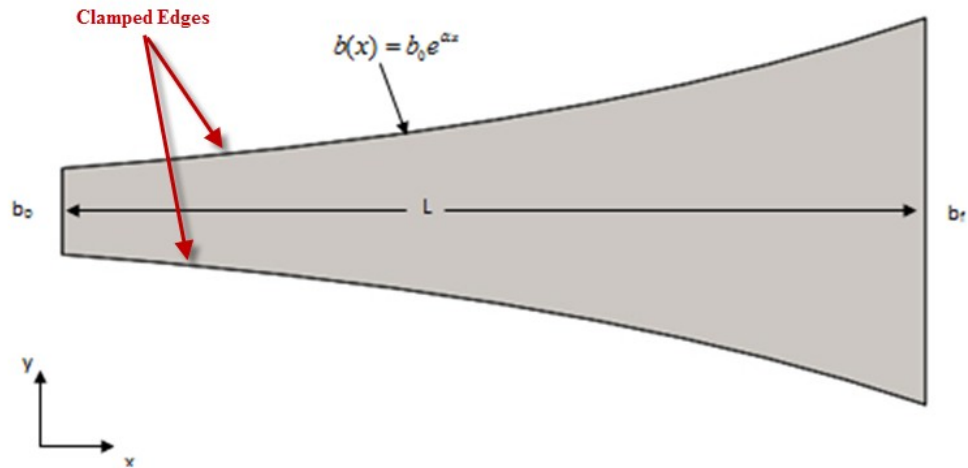
Figure 6 Top view of exponentially tapered plate, tapered edges are clamped

The symbols used in the equations to follow are defined in Table 2

Symbol	Parameter	Units
E	Young's Modulus y-direction	N/m^2
b_0	Initial width of plate	Meters
b_f	Final width of plate	Meters
ρ	Density	kg/m^3
ν	Poisson's ratio	Unitless
h	Plate thickness	Meters
L	Plate length	Meters
m_a	Mass per unit area of plate	kg/m^2
P	Input Displacement	Meters
ω	Frequency	rad/s

Table 2 Numerical modeling notation

2.1 Finite Difference

In this case the device being investigated is a thin plate therefore the Kirchoff-Love plate operator [31] is used. Before reducing the order of the model the governing equation for bending motion of an orthotropic plate neglecting damping effects is [32]:

$$\frac{\partial^2}{\partial x^2}\left[D_{xx}\frac{\partial^2 w}{\partial x^2}+D_{xy}\frac{\partial^2 w}{\partial y^2}\right]+2\frac{\partial^2}{\partial x \partial y}\left[D_{sh}\frac{\partial^2 w}{\partial x \partial y}\right]+\frac{\partial^2}{\partial y^2}\left[D_{xy}\frac{\partial^2 w}{\partial x^2}+D_{yy}\frac{\partial^2 w}{\partial y^2}\right]+m_a\frac{\partial^2 w}{\partial t^2}=0 \text{ (2.1)}$$

The orthotropic plate bending stiffnesses [33] are defined as:

$$D_{yy} = \frac{E_y^2 h^3}{12\left(E_x - v_{xy}^2 E_y\right)} \qquad\qquad D_{xy} = \frac{v_{xy} E_x E_y h^3}{12\left(E_x - v_{xy}^2 E_y\right)}$$

$$D_{xx} = \frac{E_x E_y h^3}{12\left(E_x - v_{xy}^2 E_y\right)} \qquad\qquad D_{xh} = \frac{1}{6} G_{xy} h^3$$

where w is the normal plate displacement, h is the plate thickness, E_y is the modulus of elasticity in the

y-direction, E_x is the modulus of elasticity in the x-direction, G_{xy} is the shear modulus, and v_{xy} is

Poisson's ratio, however since the PZT plate is only mildly orthotropic the derivation will be done

assuming an isotropic material. For the isotropic case the equation simplifies to:

$$D\left(\frac{d^4 w}{dx^4} + 2\frac{d^4 w}{dy^2 dx^2} + \frac{d^4 w}{dy^4}\right) - m_a \frac{\partial^2 w}{\partial t^2} = 0 \tag{2.2}$$

where $D = \dfrac{Eh^3}{12\left(1 - v^2\right)}$, and E is the isotropic modulus of elasticity and v is the isotropic Poisson's ratio.

One way to solve this differential equation is to use separation of variables as well as a reduction of

order. First we will use separation of variables and assume a solution of the form:

$$w(x, y, t) = \Psi(y) U(x, t) \tag{2.3}$$

Because the solution is assumed to be time-harmonic, the time dependency of the solution can be

written as:

$$U(x, t) = C_1 u(x) e^{-i\omega t} \tag{2.4}$$

For low frequencies we can assume that only the first lateral structural mode is excited. In this case

$\Psi(y)$ will be the shape of the assumed cross-modes for a clamped boundary condition [34].

$$\Psi(y) = \cos^2\left(\frac{y\pi}{b(x)}\right) \tag{2.5}$$

Where $b(x)$ is the function that represents the exponential variation of the width as shown in Figure 6 and is increasing as we move in the positive x-direction. In this case the factor by which the width increases is represented by α.

$$b(x) = b_0 e^{\alpha x}$$

$$\alpha = \left(\frac{1}{L}\right) \ln\left(\frac{b_f}{b_0}\right)$$

(2.6)

Plugging into equation (1.1) and evaluating the derivatives of $U(x,t)$ and since the cross modes:

$$D\left(\Psi \frac{d^4 U}{dx^4} + 2\Psi'' \frac{d^2 U}{dx^2} + \Psi'''' U\right) e^{-i\omega t} - m_a \omega^2 \Psi U e^{-i\omega t} = 0$$

(2.7)

In (2.7) we can see that the $e^{-i\omega t}$ factor can be cancelled and we multiply by the orthogonal cross-mode shape and then integrate over the varying width $b(x)$ to obtain:

$$D\left(\int_{-\frac{b(x)}{2}}^{\frac{b(x)}{2}} \Psi^2 dy \frac{d^4 U}{dx^4} + 2\int_{-\frac{b(x)}{2}}^{\frac{b(x)}{2}} \Psi\Psi'' dy \frac{d^2 U}{dx^2} + \int_{-\frac{b(x)}{2}}^{\frac{b(x)}{2}} \Psi\Psi'''' dy U\right) - m_a \omega^2 U \int_{-\frac{b(x)}{2}}^{\frac{b(x)}{2}} \Psi^2 dy$$

(2.8)

Evaluating the integrals we obtain:

$$\int_{-\frac{b(x)}{2}}^{\frac{b(x)}{2}} \Psi^2 dy = \frac{3b(x)}{8}$$

$$\int_{-\frac{b(x)}{2}}^{\frac{b(x)}{2}} \Psi \frac{d^2 \Psi}{dx^2} dy = -\frac{\pi^2}{2b(x)}$$

(2.9)

$$\int_{-\frac{b(x)}{2}}^{\frac{b(x)}{2}} \Psi \frac{d^4 \Psi}{dx^4} dy = \frac{2\pi^4}{b(x)^3}$$

This procedure results in a differential equation in only a single variable. Applying the appropriate boundary conditions for a plate with a harmonic input displacement at $x = 0$, $x = L$ is free and the exponentially varying sides are fixed:

$$\text{at } x = 0 : u(x) = P, \frac{\partial}{\partial x} u(x) = 0$$

$$\text{at } x = L : \frac{\partial^2}{\partial x^2} u(x) = 0, \frac{\partial^3}{\partial x^3} u(x) = 0$$

(2.10)

The boundary conditions for the exponentially varying edges are built into the function for the cross-modes.

Now that the governing equation has been simplified sufficiently and we have defined appropriate boundary condition the MATLAB® function bvp4c can be used to obtain a numeric solution. This function will provide numeric solutions to an ordinary differential equation (ODE) boundary value problem (BVP) when provided with a set of first order ordinary differential equations. The first step in obtaining a solution is to convert the fourth order ODE into the appropriate first order form. This is done by first rearranging the equation and renaming the coefficients that are a function of $b(x)$ as follows:

$$\Psi_1 = \frac{3b(x)}{8}$$

$$\Psi_2 = -\frac{\pi^2}{2b(x)}$$

$$\Psi_3 = \frac{2\pi^4}{b(x)^3}$$

(2.11)

This step only serves to simplify the equation during the conversion process, using these new variables and simplifying, we obtain:

$$\Psi_1 U'''' + 2\Psi_2 U'' + \left(\Psi_3 - \beta\right) U = 0$$

(2.12)

Where:

$$\beta = \frac{m_a \omega^2 \Psi_1}{D}$$

(2.13)

Now if we let:

$$
\begin{aligned}
U &= \theta_1 \\
U' &= \theta_1' = \theta_2 \\
U'' &= \theta_2' = \theta_1'' = \theta_3 \\
U''' &= \theta_3' = \theta_1''' = \theta_4
\end{aligned}
$$
(2.14)

And then substituting back into (2.12) and rearranging to solve for the highest order derivative, the

fourth order in this case, we obtain a set of first order ODEs suitable for use in bvp4c.

$$
\begin{bmatrix} \theta_1' \\ \theta_2' \\ \theta_3' \\ \theta_4' \end{bmatrix} =
\begin{matrix} \theta_2 \\ \theta_3 \\ \theta_4 \\ \dfrac{2\Psi_2 \theta_3 + (\Psi_3 - \beta)\theta_1}{\Psi_1} \end{matrix}
$$
(2.15)

Since bvp4c solves the equations numerically the three equations in (2.11) will be evaluated for a new

value of x for each iteration. The code used is shown in Appendix A.1 and the results are shown in the

results section of this chapter.

2.2 Structural FEA Analysis (COMSOL)

In this section, the motion of the plate will be evaluated using finite element analysis in order to

verify the validity of the numerical finite difference model the same plate model using COMSOL

Multiphysics® 4.2. This was done using the Solid Mechanics module and a linear elastic material model

and running a Frequency Domain analysis. Mesh settings were automatically set by the software using

the Physics-controlled mesh setting with Courser element size, this corresponds to a maximum element

size of 0.0177m and a minimum element size of 0.0037m. The centerline symmetry of the plate allows

the use of a symmetry constraint greatly reducing the solve time of the model. The model consists of

34609 elements, using a finer mesh was found to have no impact on the results obtained for the structural model. Material properties used for PZT-5H are shown in Table 3.

Symbol	Parameter	Value	Units
E	Young's Modulus y-direction	6.2e10	N/m^2
b_0	Initial width of plate	9.4e-3	Meters
b_f	Final width of plate	71.12e-3	Meters
ρ	PZT-5H Density	7800	kg/m^3
ν	PZT-5H Poisson's ratio	0.33	Unitless
h	Plate thickness	.127e-3	Meters
L	Plate length	55.88e-3	Meters
P	Input Displacement at x=0	1e-5	Meters

Table 3 Parameter values for structural analysis

The device was modeled as two plates of thickness h considered to form a union at the coincident face this allowed there to be at least two elements through the thickness of the part without having to manually modify the automatic physics based mesh settings. The plate was then driven by an input displacement at b_0 and left free at b_f per the boundary conditions specified for the numerical solution in eq. (2.10). The exponentially varying edges were given a fixed constraint. The mesh and boundary conditions are shown in Figure 7
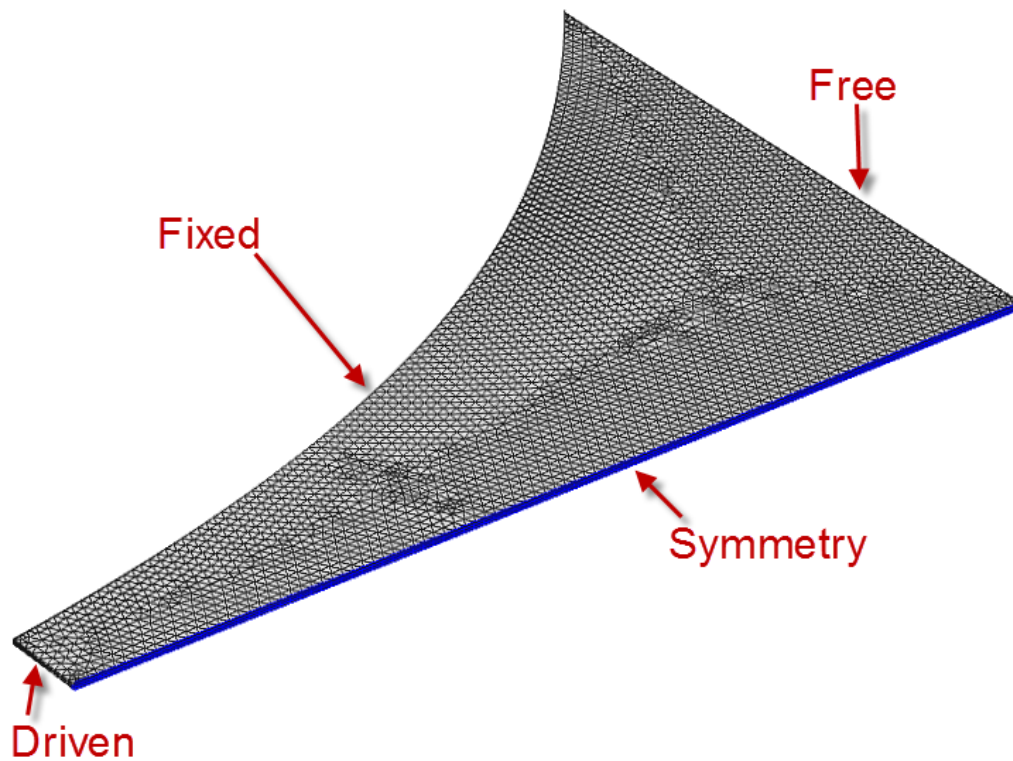
Figure 7 COMSOL® mesh and boundary conditions

2.3 **Results**

The solution obtained by the finite difference method can now be evaluated numerically using the

MATLAB function bvp4c (See Appendix A.1). The results for selected frequencies are shown below as 3D

plots of displacement. The results for each frequency are shown for both COMSOL® and Matlab®.

The first set of plots (Figure 8 and Figure 9) show the full plate at 100 Hz, it can clearly be seen that

by far the largest displacement is caused by the input displacement itself. What is seen here is a result of

evanescence of the structure. Therefore in the subsequent plots the first 20mm of the plate is omitted.

This allows the displacement pattern of the rest of the plate to be seen without being overshadowed by

the much larger input displacement and the FEA and numerical results can still be compared.

19
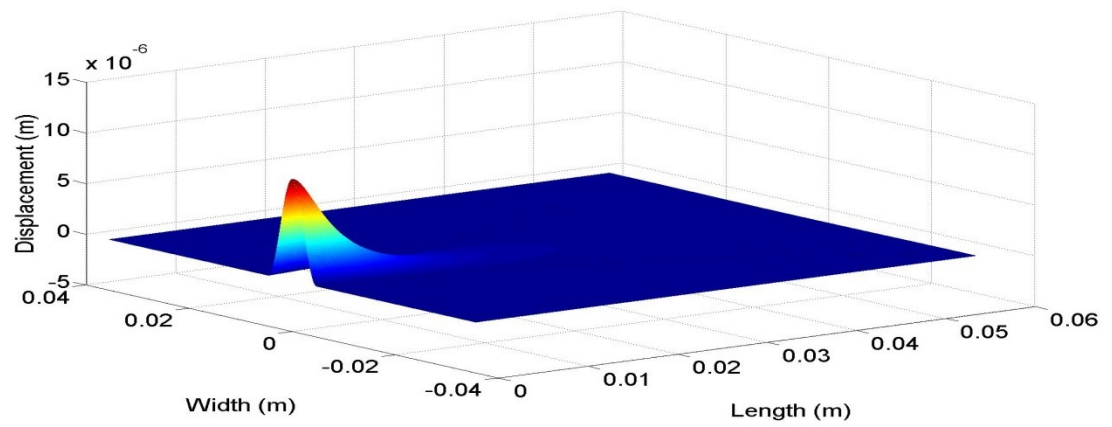
Figure 8 Full plate at 100 Hz showing evanescence (Matlab®)

In both Figure 8 and Figure 9 we see that the maximum displacement is at the base and is equal

to 1×10^{-5} m which is to be expected since this is the defined input at $x = 0$ in both cases.
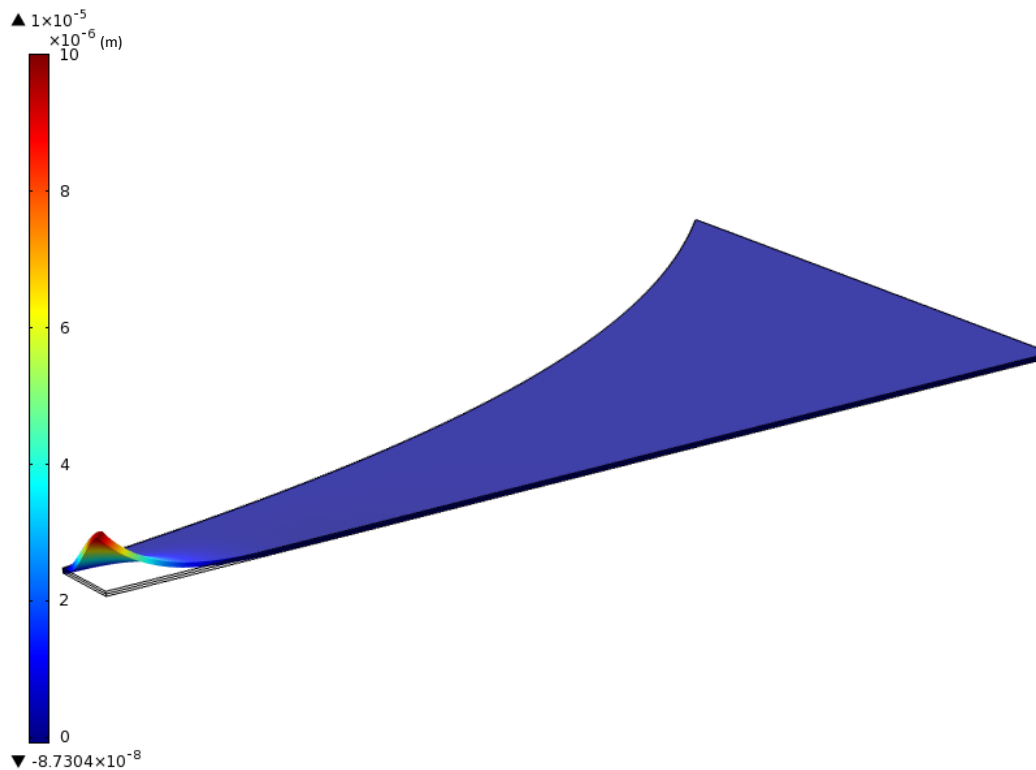
Figure 9 Full plate at 100 Hz showing evanescence (COMSOL®)
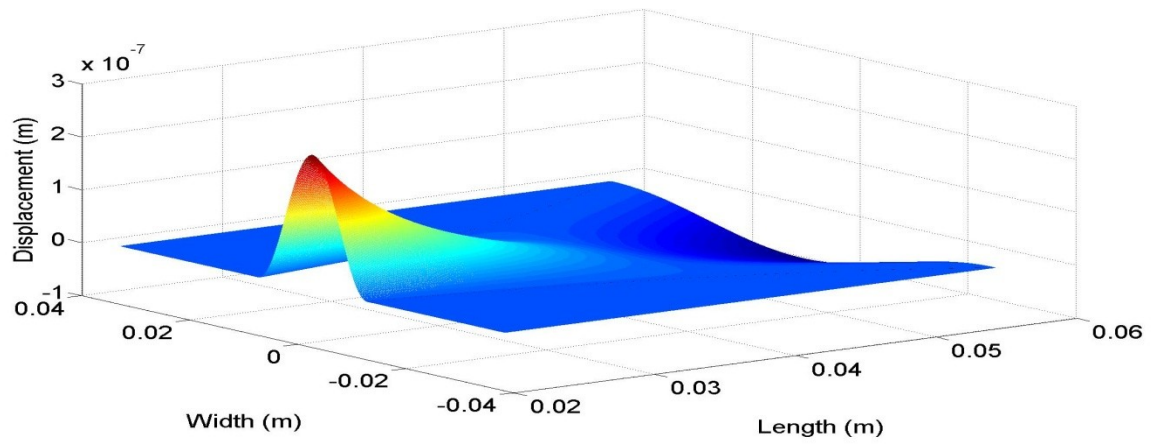
Figure 10 Displacement at 100 Hz (Matlab®)
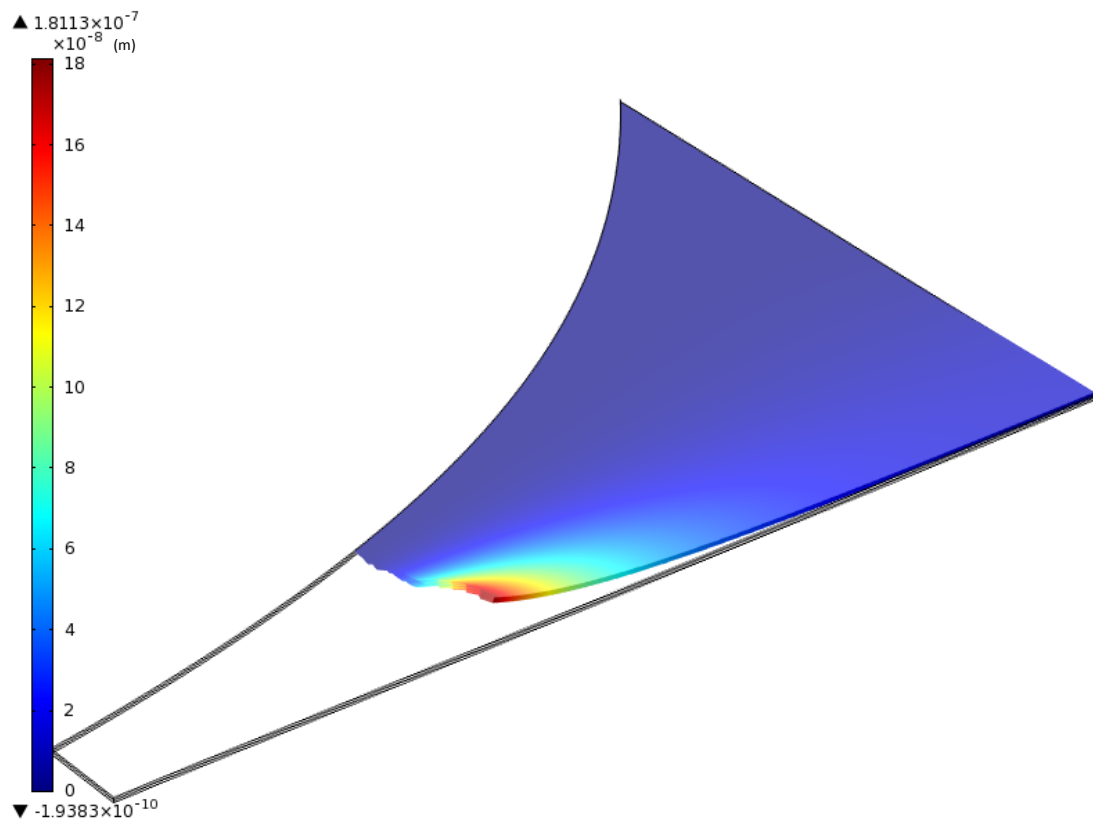
Figure 11 Displacement at 100 Hz (COMSOL®)

Figure 10 shows the results of the numerical solution from MATLAB® and the maximum

displacement at $\mathrm{x} \geq 20\mathrm{mm}$ at 100Hz is approximately $2.5 \times 10^{-7}\,\mathrm{m}$. The same set up run in COMSOL®

gives a maximum displacement of 1.81×10^{-7}, shown in Figure 11, which is very close to the simpler numerical MATLAB® solution.
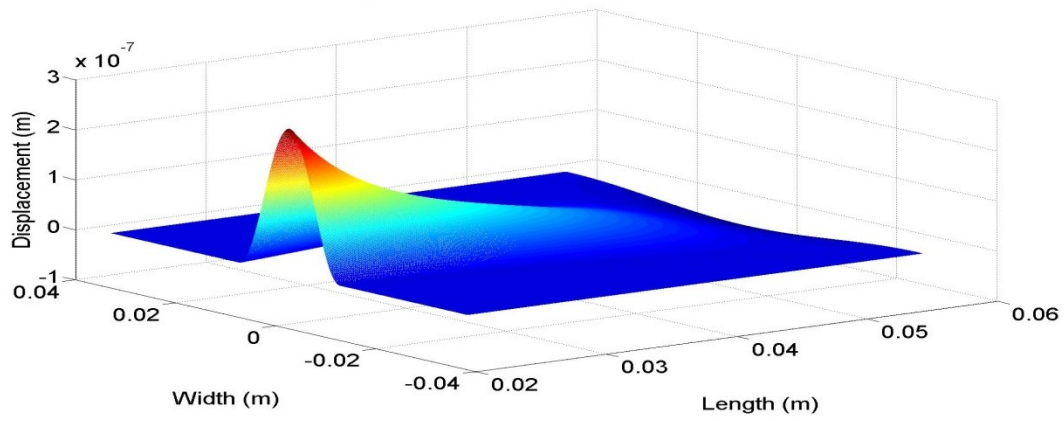
Figure 12 Displacement at 548 Hz (Matlab®)
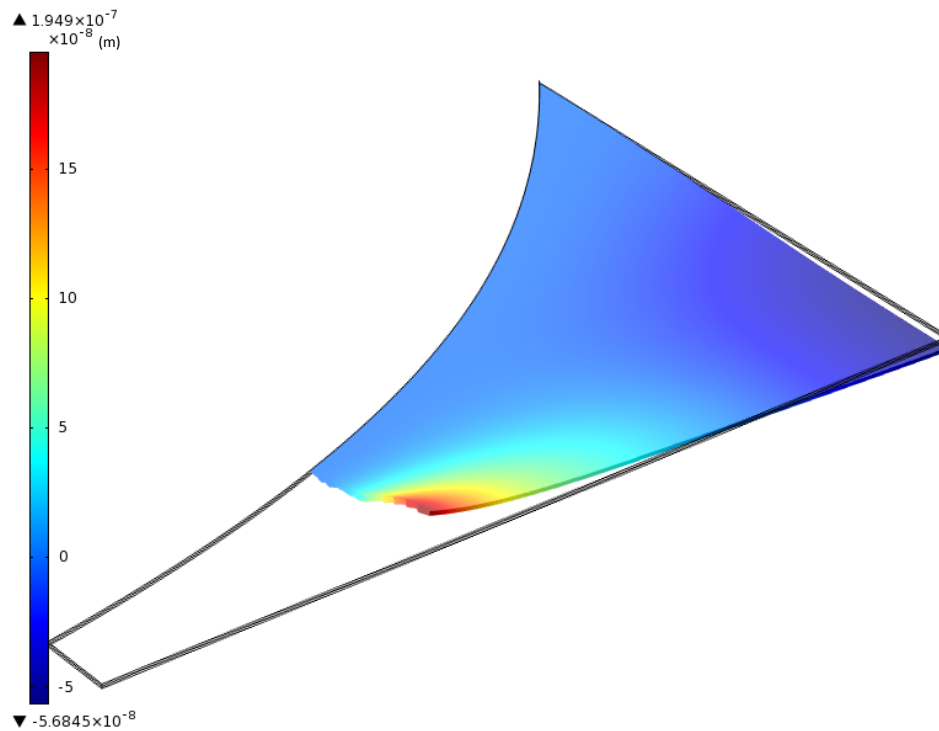
Figure 13 Displacement at 548 Hz (COMSOL ®)

In Figure 12 and Figure 13 the maximum displacements are approximately 3.0×10^{-7} and 1.95×10^{-7} respectively at 548Hz and we continue to see good agreement between the two solutions.
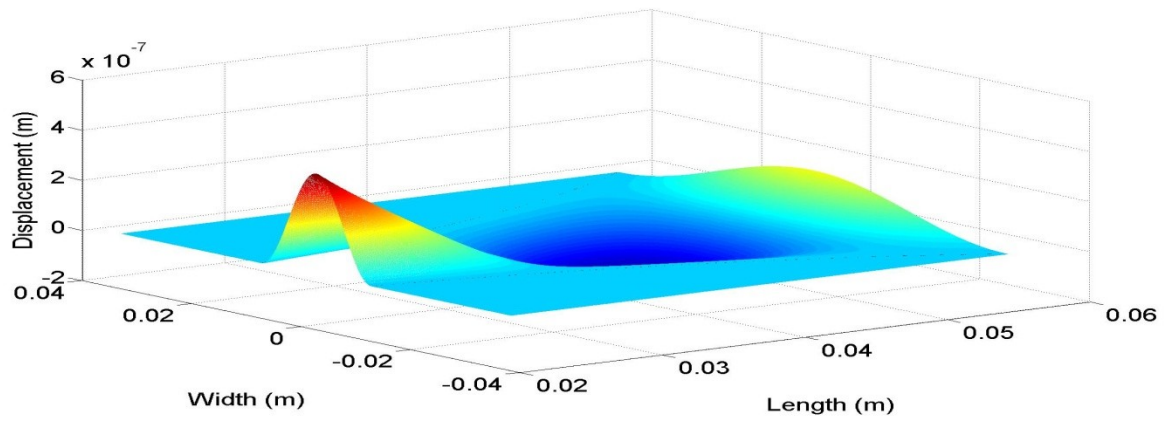
Figure 14 Displacement at 1282 Hz (Matlab®)
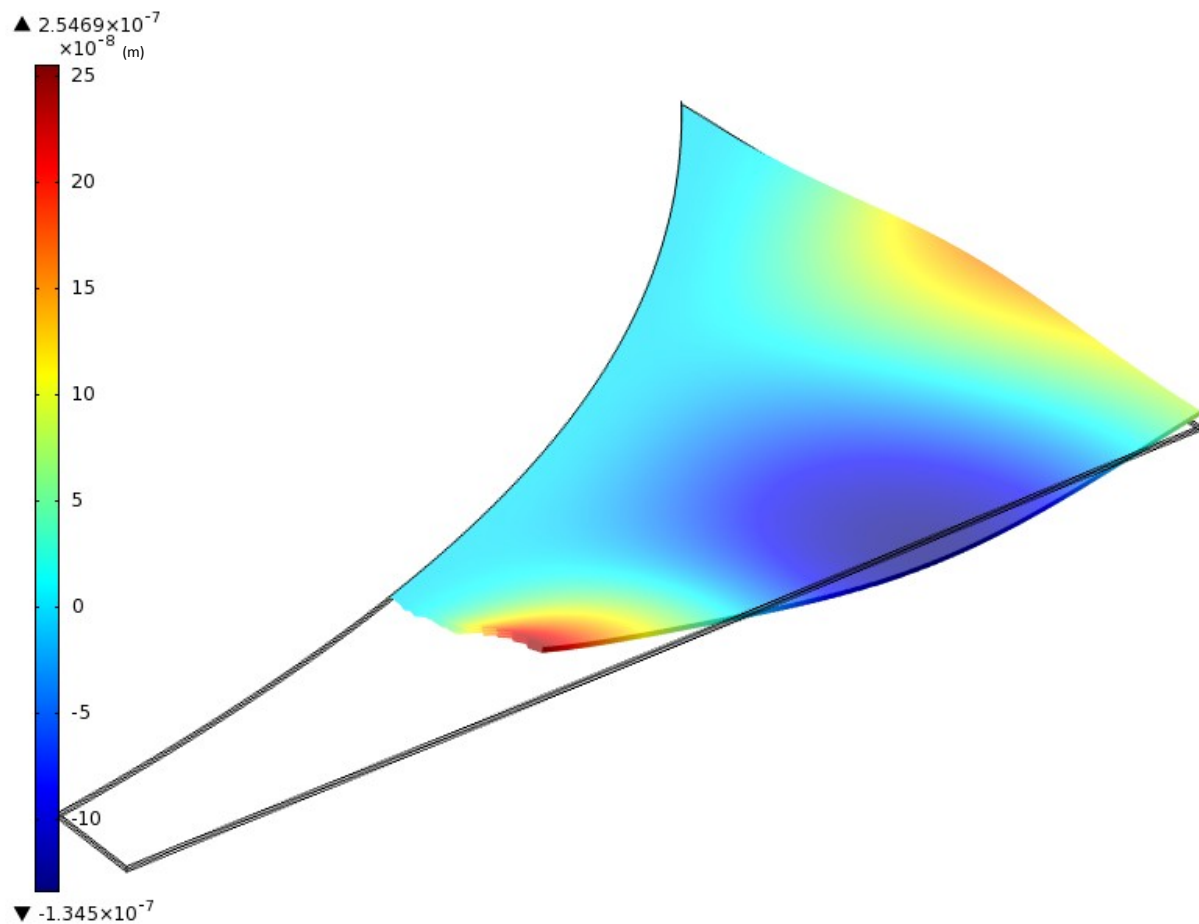
Figure 15 Displacement at 1282 Hz (COMSOL®)

Figure 14 and Figure 15 we see that once again there is good correlation between the numerical and simulation results, about 3.5 x 10⁻⁷ m and 2.5 x 10⁻⁷ m and the displacement shape of the plate is almost identical.
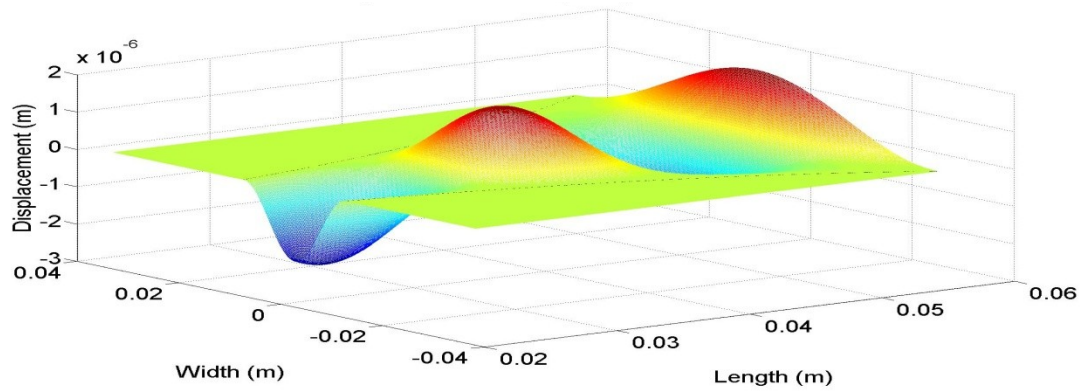
Figure 16 Displacement at 3000 Hz (Matlab®)
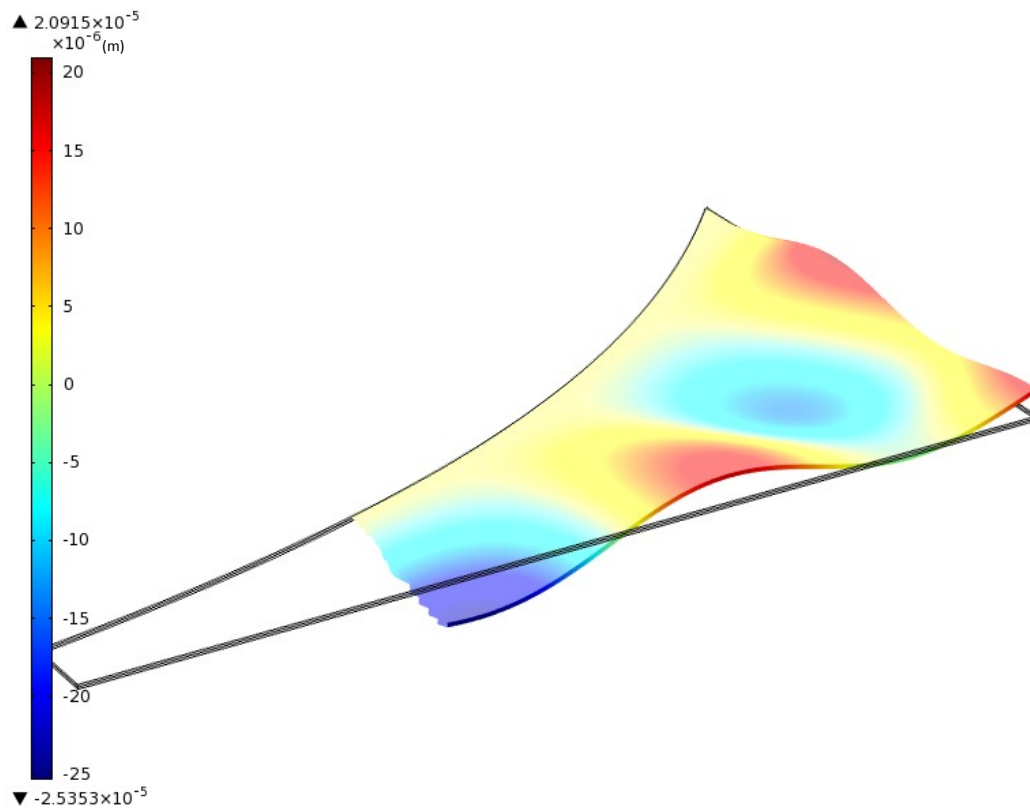
Figure 17 Displacement at 3000 Hz (COMSOL®)

In Figure 16 and

Figure 17 we begin to see a bigger divergence between the results as more complex cross-modes are introduced particularly at the wider end of the plate. Here we can also see that the maximum displacement locations are also moving, in the Matlab® results the peaks are shifted more towards the wide end of the plate. This is expected, since the Matlab® solution assumed a single first structural cross mode, but the FEA has full two dimensional freedom.

In order to determine the low frequency evanescent cut-off an additional simulation was run for the first 6 resonant frequencies (excluding the 1st mode, which showed no visible displacement away from the input) as calculated by an Eigenfrequency study. The results are shown in Figure 18. Here we see that already at the 3rd resonant mode, or around 1500Hz, the resulting maximum displacements along the length of the plate are greater than the input displacement applied.
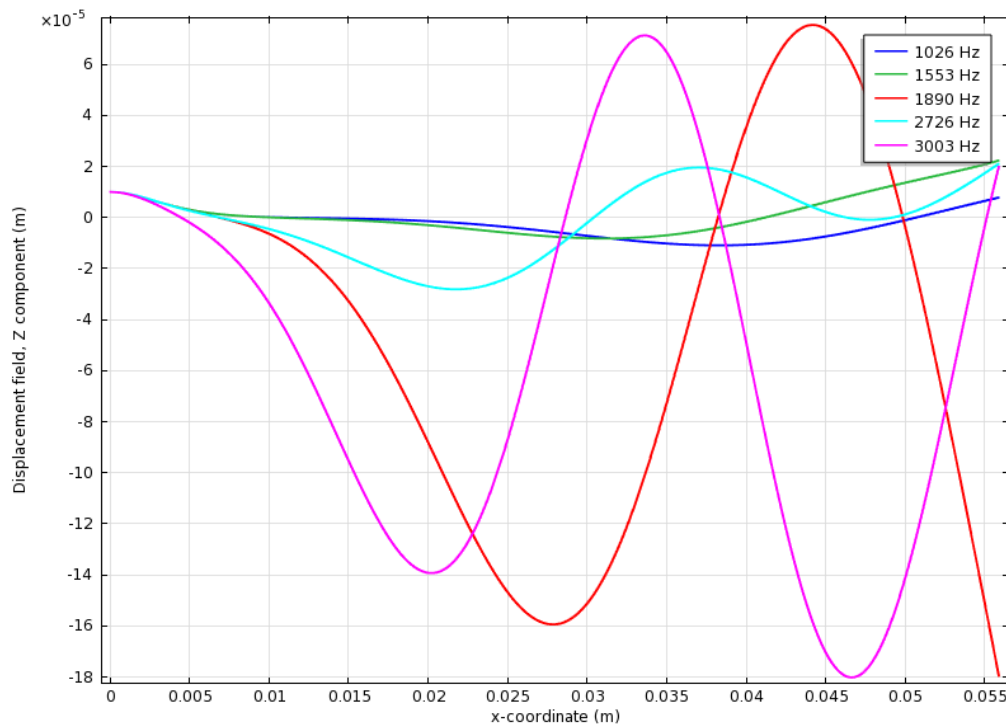
Figure 18 Displacement at centerline along length of plate near resonant frequencies for structural model

2.4 **Discussion**

The results show that at low frequencies wave propagation is limited and most of the displacement is at $x = 0$, due to the evanescent nature of the solution. As the frequency is increased, the waves begin to propagate further down the plate and we begin to see standing waves that generate greater displacements along the beam than at the input. It can also be seen that the cross-mode equation is an over-simplification of the problem at high frequencies. This will be seen in the next chapter, but for low frequencies the finite difference solution matches quite well with the FEA solution obtained, indicating that for a structural analysis the model is adequate. The effects of the piezoelectric effect will be discussed further in the next chapter. Already in the structural analysis we see the effects of the wave evanescence discussed in the introduction. This effect limits displacements in the structural model at low frequencies which will adversely affect the potential for power output in the structure even as the piezoelectric effect is introduced to the model. Although at this stage the evanescence is limited to frequencies below approximately 1500 Hz, a promising result that indicates that although this would still be a high frequency energy harvester there is potential to begin to see good output power at reasonably low frequencies.

Chapter 3   Piezoelectric Plate Model

Since the finite difference method of Chapter 2 neglected piezoelectric coupling further FEA analysis was done using COMSOL® 4.2. The FEA model was run for both the simpler structural case which would be expected to provide a good match to the solution obtained using the finite difference method, confirmed by the results shown in Chapter 2, and also using the Piezoelectric package available in COMSOL® where the structural solution is coupled with the piezoelectric properties of PZT-5H.

3.1 Voltage and Displacement Coupling in Bimorph Piezoelectric devices

The plate being analyzed is, as is often the case with energy harvester devices, in a bimorph configuration. Generally due to the brittle nature of piezoelectric materials these bimorph devices consist of two layers of piezoelectric material with a conducting shim in between. This shim is often made from brass. In this case the plate used was custom made and therefore only consisted of the two piezoelectric layers with no shim.

There are two basic configuration available for bimorph devices; series (Figure 19) and parallel (Figure 20). The poling is applied during the manufacturing process by applying a DC bias to the material at high temperatures. Once the material cools the dipoles are permanently aligned which maximizes the response to mechanical input [35].

For a series configuration the layers of the piezoelectric are poled in opposite directions. The result is that under bending one layer will be in tension and the other in compression. This results in the generated voltage field for each layer also being in opposite directions, and therefore the result is opposite terminals on either side of the plate.

When the bimorph is poled in parallel the layers are poled in the same direction, this means that a common terminal must be introduced between the two layers. This would involve electroding the interface between the layers which is quite cumbersome making a series configuration far simpler to deal with and parallel configuration are rarely seen in literature.
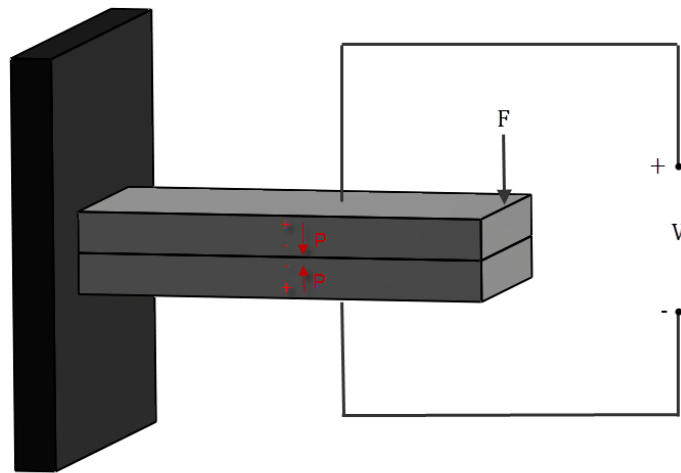
Figure 19 Series poled piezoelectric bimorph
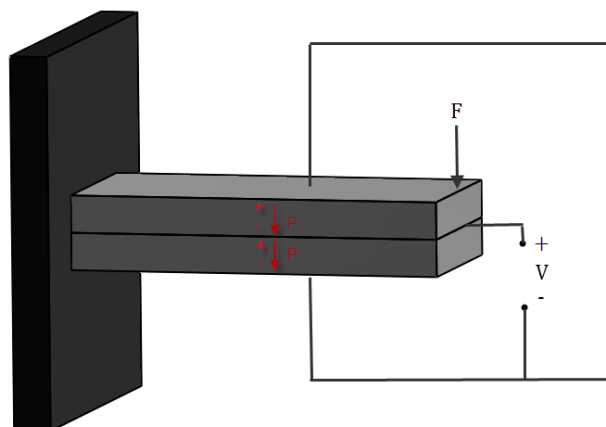
Figure 20 Parallel poled piezoelectric bimorph

When operated in series the circuit model for a bimorph device can be approximated as shown in Figure 21. The current sources shown in Figure 21 are in the same direction due to the opposite poling of the two layers of the bimorph device. The current sources come from the coupling to mechanical strain, and will give an output proportional to the surface integral of the total electric displacement over the surface of the plate.
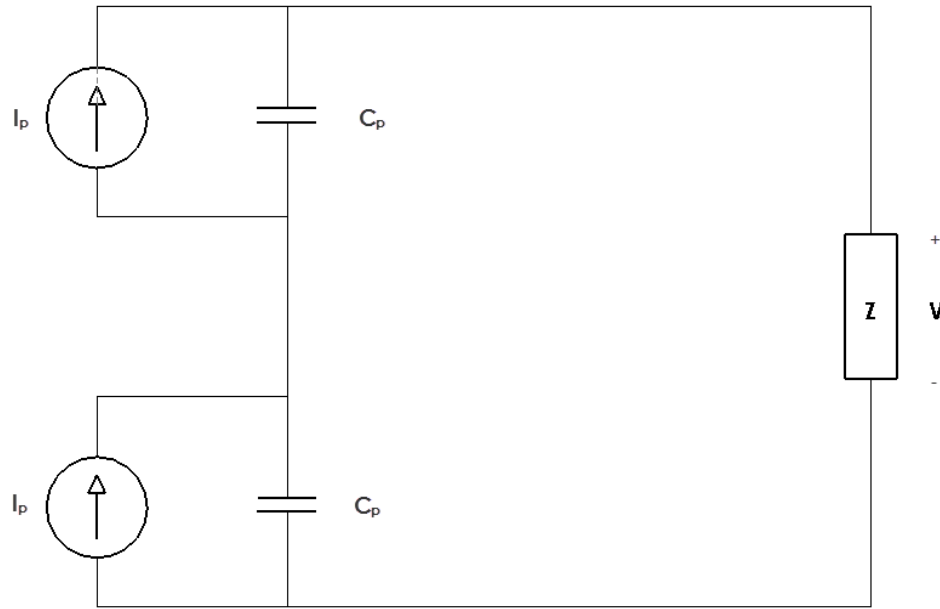
Figure 21 Circuit model for series poled bimorph

The load, Z, is connected across the plate. Power is dissipated in the load. The circuit can be evaluated using Kirchoff's Current Law yielding the expression below which will become useful in power output considerations in Chapter 4. The factor of 2 in the denominator is the result of there being two current sources.

$$I_p = \frac{C_p}{2}\frac{dV}{dt} + \frac{V}{Z} \tag{3.1}$$

3.2 Material Properties and Study Setup

Using the same geometry from the structural analysis a new study was created in COMSOL® using the built in Piezoelectric Device physics model. This model couples the mechanical domain to the electrical domain allowing the piezoelectric coupling effect to be taken into account. The following material properties and parameters were used in the piezoelectric FEA analysis of the device:

Symbol	Parameter	Value	Units
b_0	Initial width of plate	9.4e-3	Meters
b_f	Final width of plate	71.12e-3	Meters
ρ	PZT-5H Density	7800	kg/m^3
ν	PZT-5H Poisson's ratio	0.33	Unitless
h	Plate thickness	.127e-3	Meters
L	Plate length	55.88e-3	Meters
P	Input Displacement at x=0	1e-5	Meters

Table 4 Parameter values for Piezoelectric FEA analysis

As with the structural model, each of the two plates is of thickness h . In addition to these mechanical properties the following piezoelectric material properties were used from the built-in material library entry for PZT-5H in COMSOL® assuming the Strain-charge form.

Compliance matrix (symmetric):

$$
s^E = \begin{bmatrix}
1.65e-11 & -4.78e-12 & -8.45e-12 & 0 & 0 & 0 \\
 & 1.65e-11 & -8.45e-12 & 0 & 0 & 0 \\
 & & 2.07e-11 & 0 & 0 & 0 \\
 & & & 4.35e-11 & 0 & 0 \\
 & & & & 4.35e-11 & 0 \\
 & & & & & 4.26e-11
\end{bmatrix} \left[\frac{1}{Pa} \right]
$$

Coupling matrix:

$$d = \begin{bmatrix} 0 & 0 & 0 & 0 & 7.41\mathrm{e}-10 & 0 \\ 0 & 0 & 0 & 7.41\mathrm{e}-10 & 0 & 0 \\ -2.74\mathrm{e}-10 & -2.74\mathrm{e}-10 & 5.93\mathrm{e}-10 & 0 & 0 & 0 \end{bmatrix} \left[\frac{C}{N} \right]$$

Relative permittivity:

$$\varepsilon = \begin{bmatrix} 3130 & 0 & 0 \\ 0 & 3130 & 0 \\ 0 & 0 & 3400 \end{bmatrix}$$

These three matrices are required to solve the coupled equations which can be formed using:

$$D = \varepsilon E \qquad\qquad (3.2)$$

Where D is the electric charge density displacement, ε is the permittivity and E is the electric field strength.

Combined with Hooke's Law:

$$S = sT \qquad\qquad (3.3)$$

Where S is strain, s is compliance and T is stress.

We obtain the coupled equations:

$$\begin{aligned} \{S\} &= \left[s^E \right]\{T\} + \left[d^T \right]\{E\} \\ \{D\} &= [d]\{T\} + \left[\varepsilon^T \right]\{E\} \end{aligned} \qquad\qquad (3.4)$$

Or written in expanded matrix form we have:

$$
\begin{bmatrix} S_1 \\ S_2 \\ S_3 \\ S_4 \\ S_5 \\ S_6 \end{bmatrix} = \begin{bmatrix} s_{11}^E & s_{12}^E & s_{13}^E & 0 & 0 & 0 \\ s_{21}^E & s_{22}^E & s_{23}^E & 0 & 0 & 0 \\ s_{31}^E & s_{32}^E & s_{33}^E & 0 & 0 & 0 \\ 0 & 0 & 0 & s_{44}^E & 0 & 0 \\ 0 & 0 & 0 & 0 & s_{55}^E & 0 \\ 0 & 0 & 0 & 0 & 0 & s_{66}^E \end{bmatrix} \begin{bmatrix} T_1 \\ T_2 \\ T_3 \\ T_4 \\ T_5 \\ T_6 \end{bmatrix} + \begin{bmatrix} 0 & 0 & d_{31} \\ 0 & 0 & d_{32} \\ 0 & 0 & d_{33} \\ 0 & d_{24} & 0 \\ d_{15} & 0 & 0 \\ 0 & 0 & 0 \end{bmatrix} \begin{bmatrix} E_1 \\ E_2 \\ E_3 \end{bmatrix}
$$

(3.5)

$$
\begin{bmatrix} D_1 \\ D_2 \\ D_3 \end{bmatrix} = \begin{bmatrix} 0 & 0 & 0 & 0 & d_{15} & 0 \\ 0 & 0 & 0 & d_{24} & 0 & 0 \\ d_{31} & d_{32} & d_{33} & 0 & 0 & 0 \end{bmatrix} \begin{bmatrix} T_1 \\ T_2 \\ T_3 \\ T_4 \\ T_5 \\ T_6 \end{bmatrix} + \begin{bmatrix} \varepsilon_{11} & 0 & 0 \\ 0 & \varepsilon_{22} & 0 \\ 0 & 0 & \varepsilon_{33} \end{bmatrix} \begin{bmatrix} E_1 \\ E_2 \\ E_3 \end{bmatrix}
$$

As with the structural analysis the device was modeled using two bodies, one to represent the top plate and the other to represent the bottom plate of the bimorph configuration. In addition to providing a convenient method to obtain multiple mesh elements through the thickness of the plate, this configuration is required to capture the series poled nature of the plate. When dealing with bimorph piezoelectric plates, the poling of the two sandwiched plates is very important and will change the response characteristics of the device. The device being tested in this case is poled in series meaning that the poling of the two plates is in opposite directions as shown in Figure 19.

The following two base vectors are then defined in COMSOL and are assigned as the material coordinate system for their respective layers. In COMSOL® the default poling for piezoelectric materials is in the z direction so only the top layer material coordinate system need be modified:

	x	y	z
x_1	1	0	0
x_2	0	1	0
x_3	0	0	−1

Figure 22 Base vector Top layer

32

$$\begin{array}{c c c c} & \text{x} & \text{y} & \text{z} \\ \text{x}_1 & 1 & 0 & 0 \\ \text{x}_2 & 0 & 1 & 0 \\ \text{x}_3 & 0 & 0 & 1 \end{array}$$

Figure 23 Base vector Bottom layer

As with the structural model, the built in physics-controlled mesh settings were sufficient to obtain accurate results. However, in the case of the piezoelectric model a finer mesh was required and the default Normal element size was used. This gave a maximum element size of 0.0162m and a minimum size of 0.0029m. This gives a total of 93112 elements over the entire device. The same boundary conditions were used as for the structural analysis to keep the model as consistent as possible. However the piezoelectric model requires the definition of a zero charge terminal and a ground terminal, these correspond to the + and – voltage terminals shown in Figure 19 respectively. A frequency domain study was then run from 100Hz to 3000Hz in 10Hz increments. Note that the electrical boundary conditions are equivalent to an infinite load impedance, that is, an open circuit.

3.3 **Results**

The first results shown in Figure 24 are displacement plots of the plate at the same frequencies plotted in the structural analysis of Chapter 2. As will be seen in Chapter 4 the displacement plots obtained from COMSOL® for these frequencies do not correspond to the experimental results. The displacement plots are shown for these particular frequencies because these are resonant frequencies in the structural model.
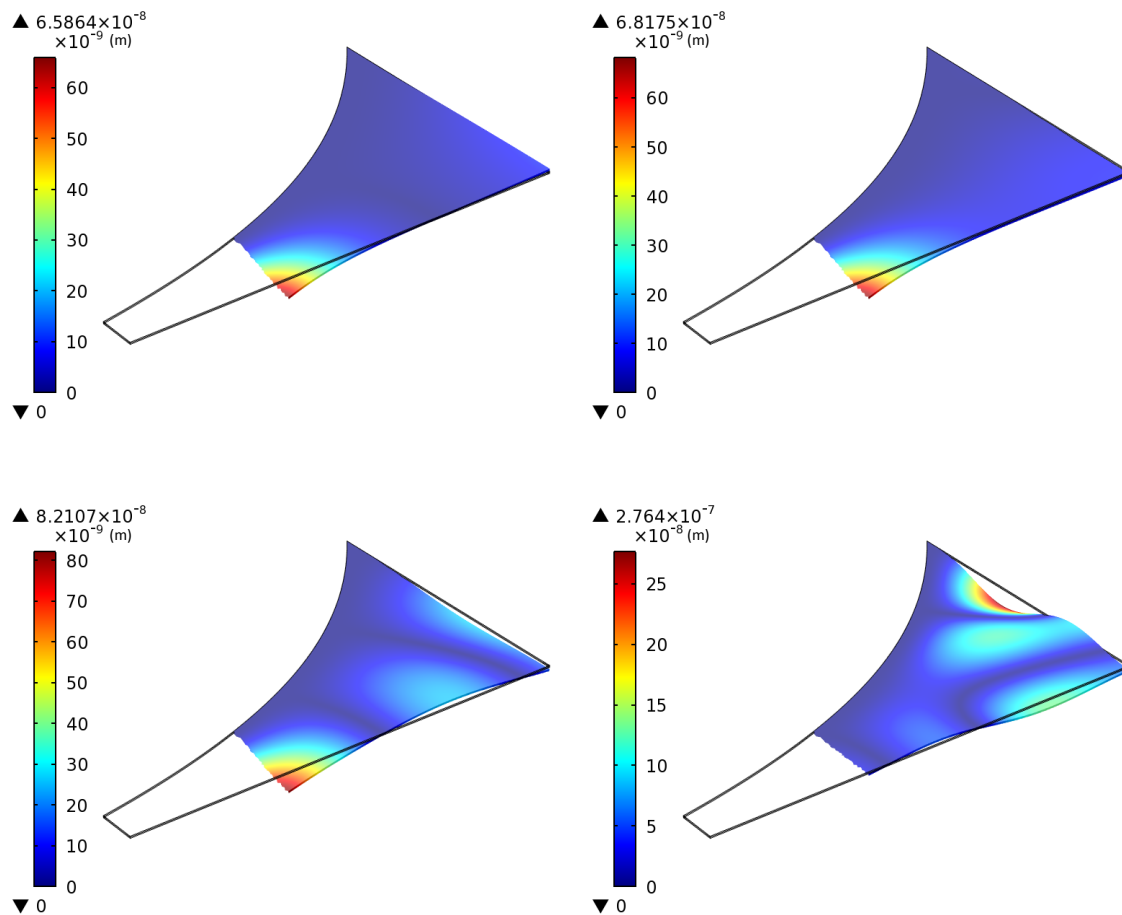
Figure 24 Displacement plots for COMSOL® piezoelectric analysis. From Top left to Bottom right: 100Hz, 550Hz, 1280Hz and 3000Hz
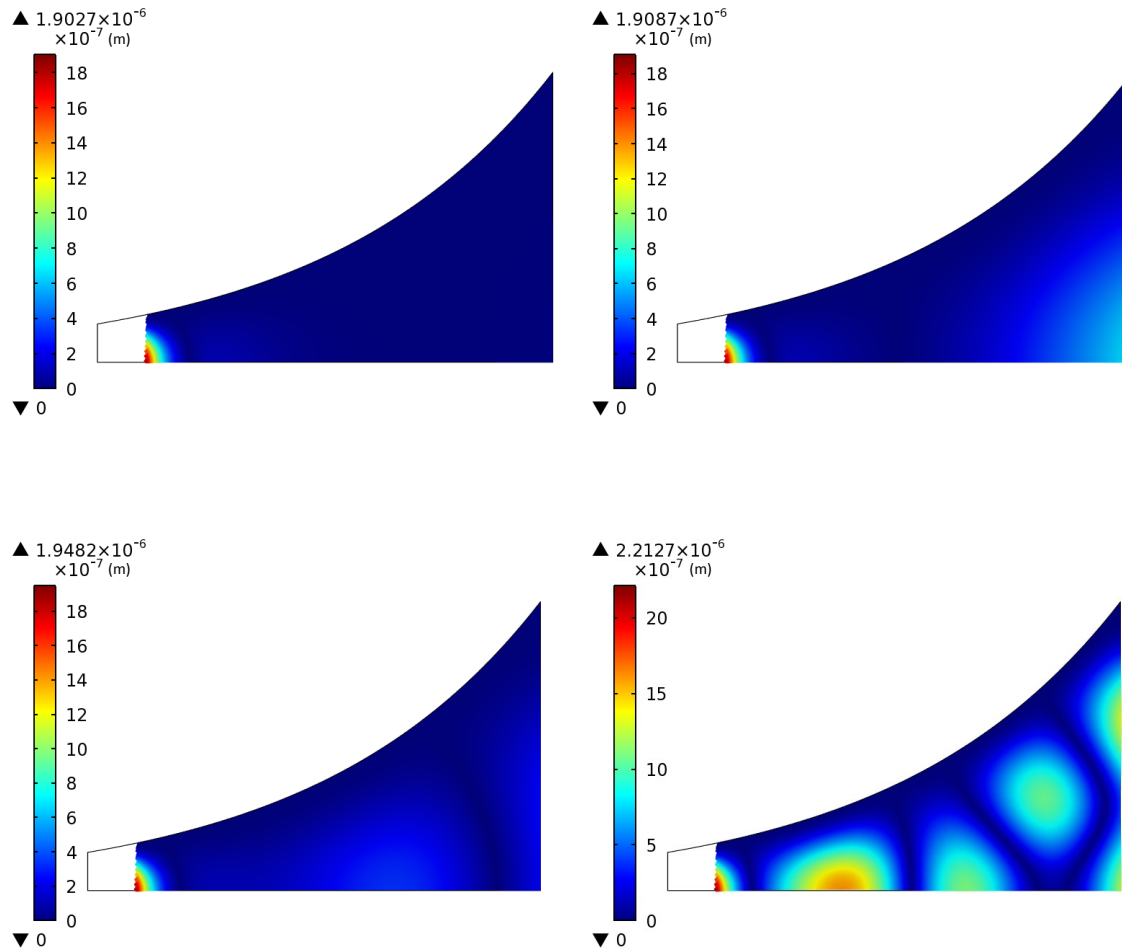
Figure 25 Plots of resonant frequencies obtain from COMSOL. Top left to Bottom right: 100Hz (not resonant), 395Hz, 1056Hz, 2807Hz

These resonant frequencies were determined by looking at the frequencies vs. voltage plot

shown in Figure 26. The plots of these frequencies are shown in Figure 25 and it should be noted that at

these frequencies the response is more pronounced, the strong evanescence of the waves still occurs

close to $x = 0$ but the excitation of the plate standing modes are quite pronounced at higher

frequencies.
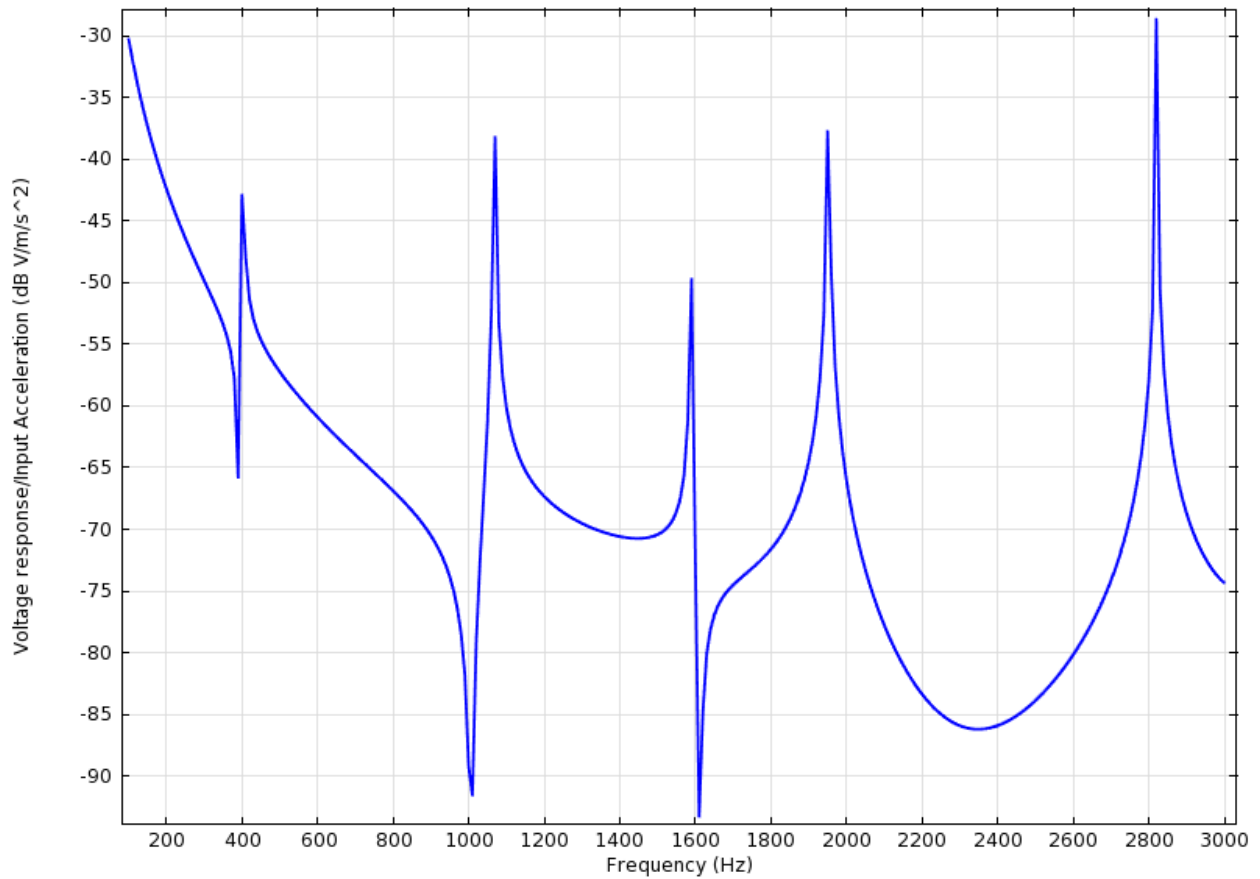
Figure 26 Voltage response/Input Acceleration vs. Frequency from COMSOL®

A similar plot to the one shown for the structural simulation is shown in Figure 27, here we see that the evanescent effect is far more pronounced when the piezoelectric effect is included in the model. It is not until around 3000 Hz that the displacement along the plate begin to approach the input displacement and it is not surpassed until around 3800 Hz.
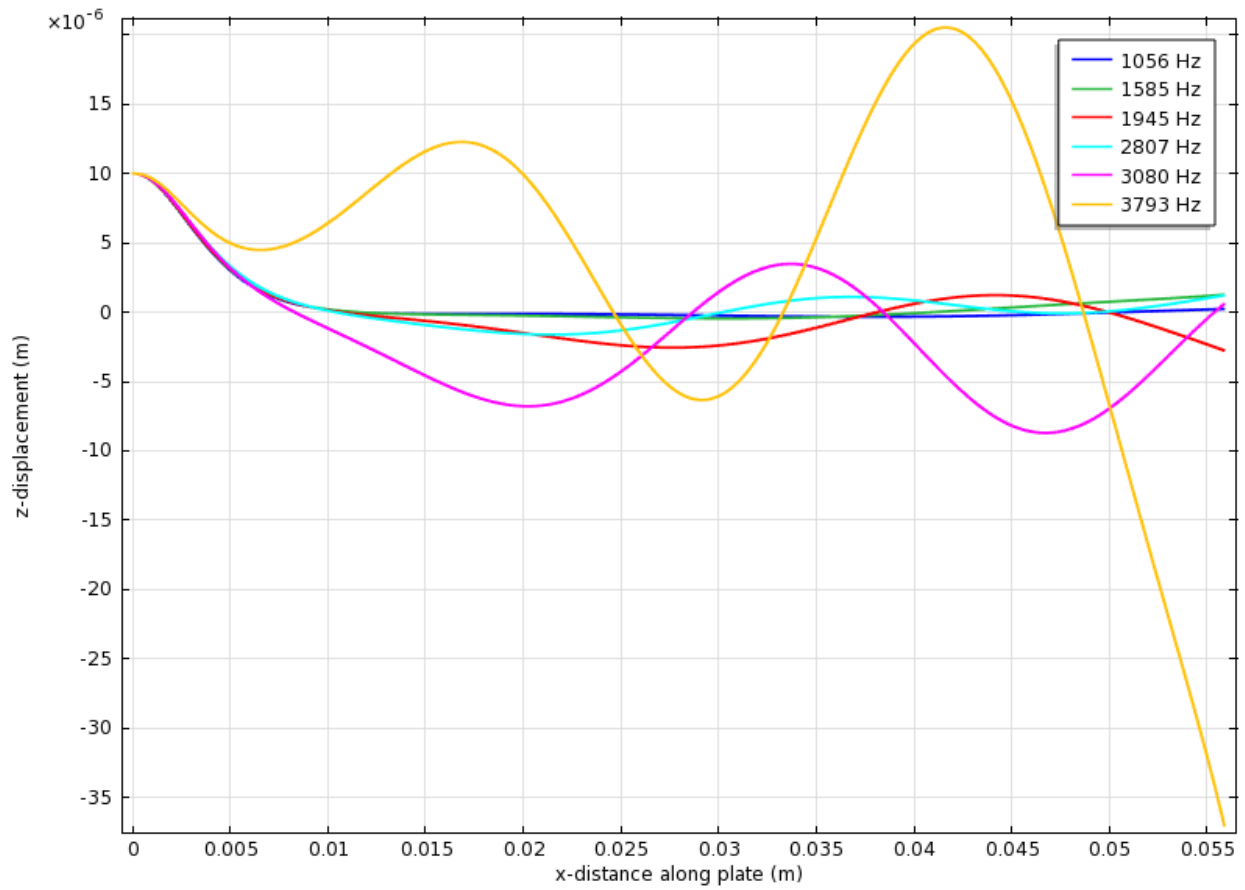
Figure 27 Displacement at centerline along length of plate near resonant frequencies for piezoelectric model

There are two additional resonances that have not been included in Figure 25, or any of the other results. Their exclusion from the general results will be discussed further in Chapter 4. The displacement plots for these two frequencies obtained from COMSOL® have been included in Figure 28 for completeness.
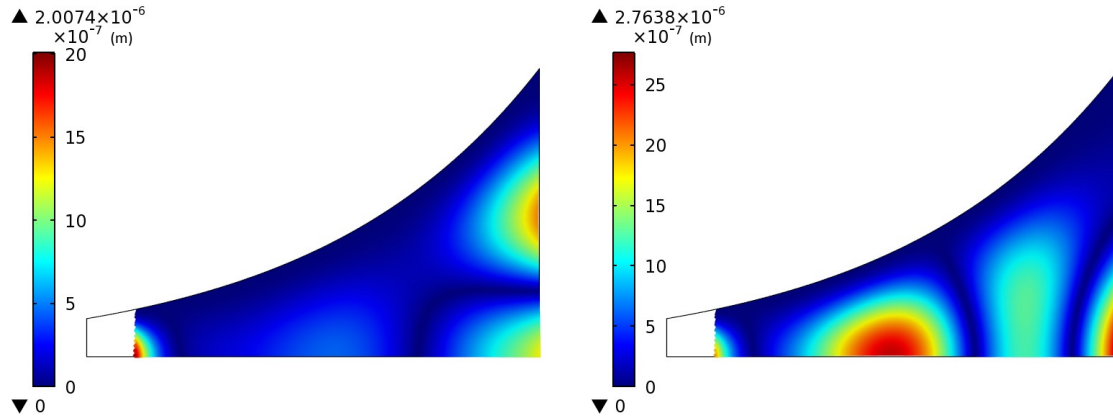
Figure 28 Additional resonant frequencies that have been excluded from overall analysis. Left: 1585Hz Right: 1945Hz

3.4 **Discussion**

It is clear from the plots shown in Figure 24 and Figure 25 that including the piezoelectric effect in the analysis has a noticeable effect on the displacement pattern generated in the plate as well as on the low frequency evanescent cut-off. This occurs due to mechanical inputs applied to the plate generating a voltage potential across the two surfaces of the piezoelectric plate, this is known as the forward piezoelectric effect. This forward piezoelectric effect in turn induces an additional mechanical response in the plate. It is this additional mechanical response that changes the frequency response of the plate resulting in the difference between the structural and piezoelectric analysis shown in the previous chapters.

Further the results show that the structural analysis alone is not sufficient as a basis for predicting resonant frequencies and therefore maximum voltage generation frequencies of the plate. The evanescence of the waves can still be seen at low frequencies and continues to be a problem in terms of the potential of this design to generate power at low frequencies. We do see a relatively high output voltage at the lower end of the frequency spectrum however this is due to the input displacement which inherently causes bending of the plate. While this cannot be dismissed as a valid source of output power

it is not what we are looking for in this case since this same phenomenon would be seen with a cantilever beam which would additionally have a much higher output voltage at its first resonant frequency. The evanescent cut-off frequency is seen to be around 3800 Hz or the 6th resonant mode of the structure.

Chapter 4   Experimental Evaluation of Exponentially varying Clamped Piezoelectric Energy Harvester

In order to explore the validity of the theoretical models presented it was necessary to devise a method by which an exponentially tapered clamped beam could be tested. In order to do this a laminated sheet of PZT5H was purchased from a manufacturer, Piezo Systems, Inc. This is a local vendor whose piezoelectric devices have been used previously for research at Tufts University yielding good results [36]. An exponential clamping structure was then used to produce the exponentially tapered plate. Vibration characterization was carried out using a scanning laser vibrometer setup, which uses a laser beam to measure velocity on the plate surface, as well as measurements of PZT voltage output.

4.1 Piezoelectric Sheet

The piezoelectric sheet purchased was series poled (see Figure 19) and was 2.2" x 2.85" (55.88mm x 72.39mm). The thickness of each of the two layers was .005" (0.127mm). This was the largest size sheet available from this manufacturer and was chosen in order to get the greatest possible variation from the small end of the taper to the large end. The two layers of PZT-5H were fully Nickel-electroded allowing for charge collection over the entire surface. On the top surface the positive terminal of the PZT was wired by soldering #32 AWG wire to the Nickel-plated surface to obtain voltage measurements. This process was performed using special flux from a Solder and Flux kit for use with Nickel-electroded PZT purchased from the manufacturer. After electroding the sheet it was painted with a reflective spray paint in order to facilitate the reflection of the laser used to gather velocity data throughout the surface of the plate. This resulted in a very significant improvement in the signal obtained from the laser vibrometer.

4.2 **Mounting Assembly**

To achieve the clamped boundary condition on three of the four sides while simultaneously creating the exponentially varying taper a mounting assembly was designed and built that consisted of two plates with an exponentially varying cut-out of the desired shape. Further a 0.01" (0.254mm) deep pocket was created in the bottom plate to accommodate the piezoelectric sheet so that it would not be compressed by the clamping force applied to keep the plates together during testing. Since the corners at the large end of the taper needed to be sharp edges the two plates were machined as two parts each. This pocket was created to be 1% larger than the PZT sheet but due to excess laminate being present on the sheet when it arrived from the manufacturer it was still necessary to manually file the sheet down to fit in the pocket. Figure 29 shows a top view of the bottom plate, while Figure 30 shows a section view in which the pocket can be seen.

The dowel pin holes shown are to keep the two plates aligned during manufacturing and the remaining ¼-20 holes are for mounting and clamping the two plates together. These holes were positioned in 1" increments so as to match the mounting holes on the vibration table used to isolate the device from ambient vibrations. Each plate is made from 0.125" (3.175mm) thick 80/20 Aluminum, the material and thickness were specifically chosen to ensure that there would be no bending in the mounting assembly during testing by virtue of the plate thickness being significantly greater than the thickness of the piezoelectric plate. This design greatly reduced the cost of the PZT plated used since custom milling of PZT by the manufacturer is very expensive; this method allowed the standard square sheet to be used without having to have it custom milled.
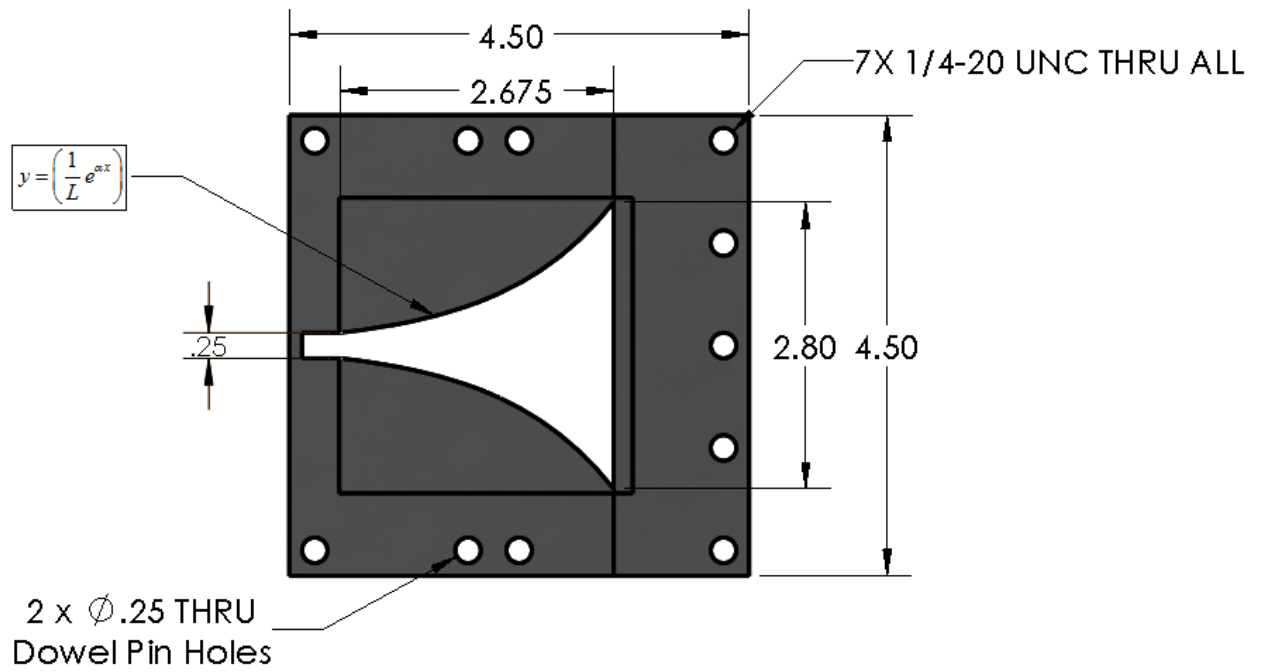
Figure 29 Top view of bottom plate
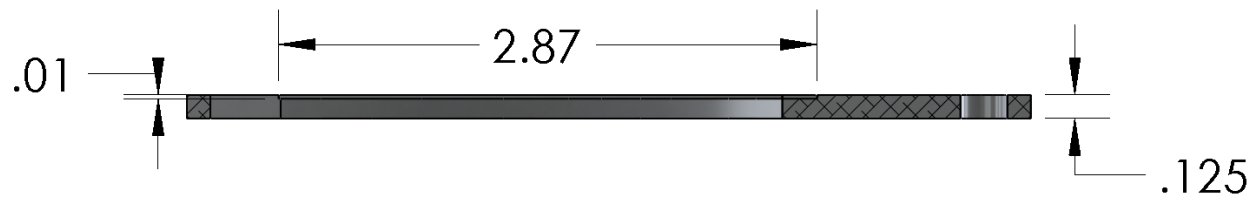
Figure 30 Section view showing plate cavity
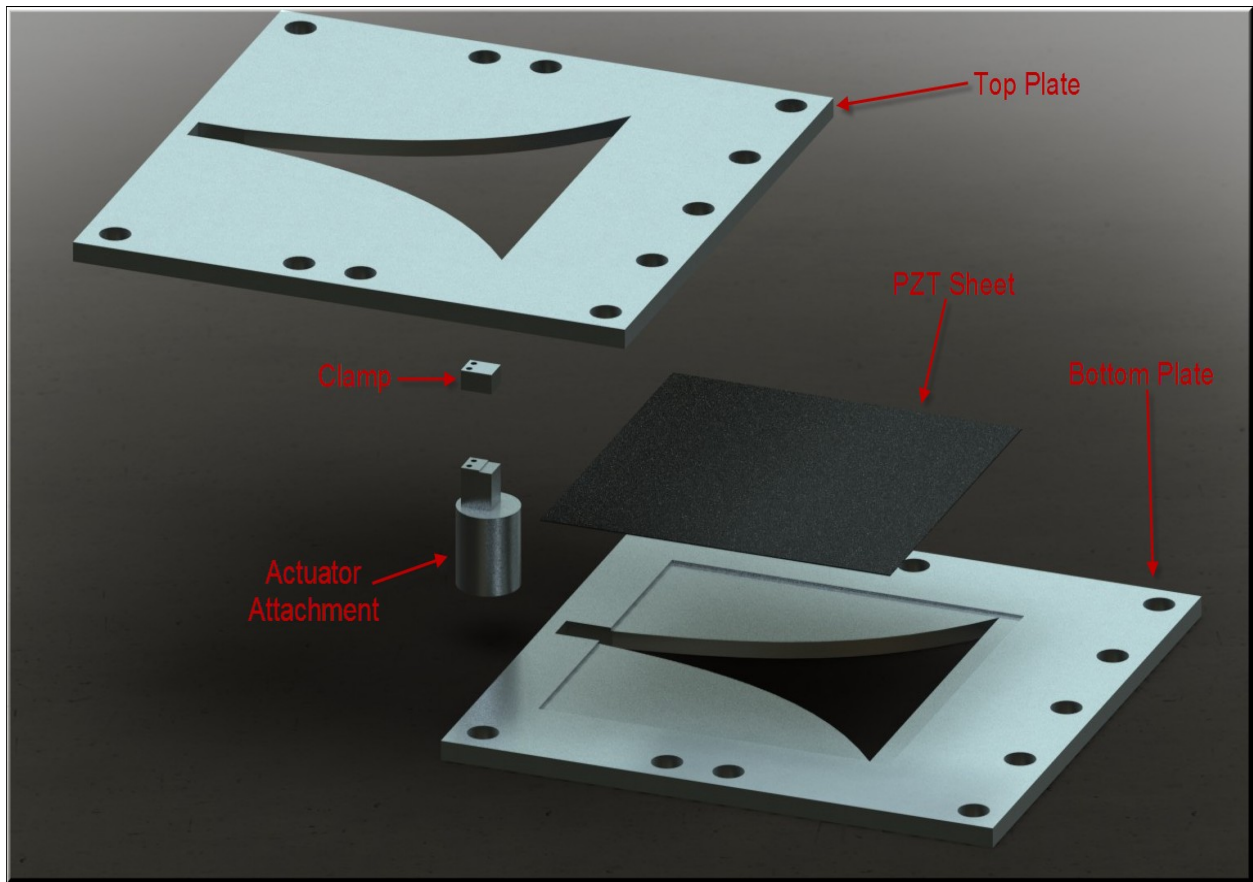
Figure 31 Exploded mounting assembly view
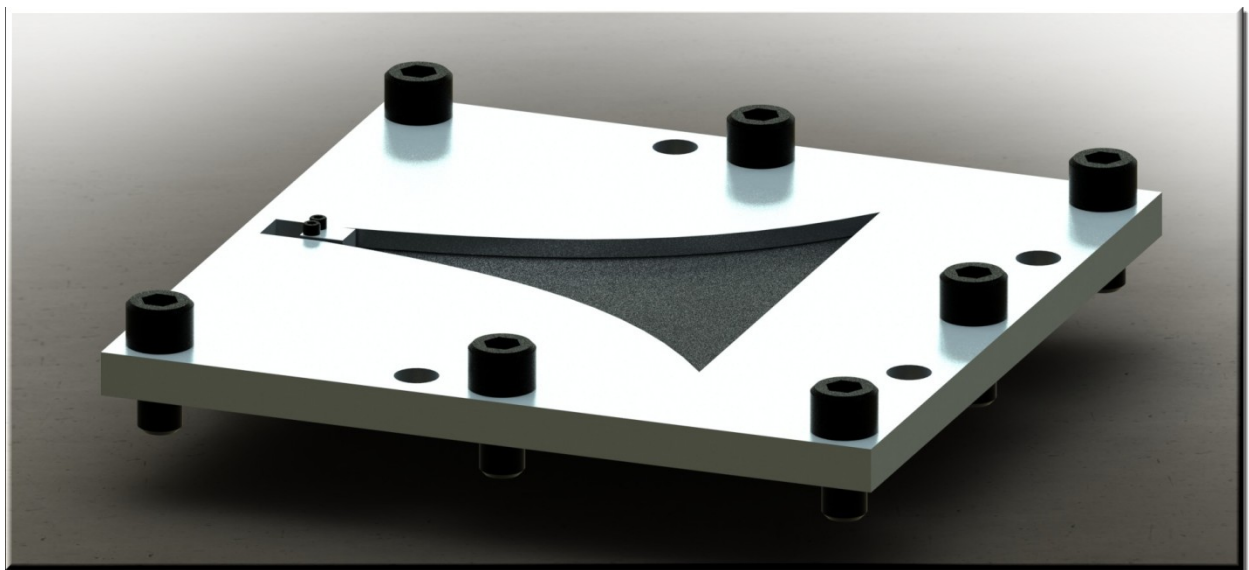
Figure 32 Mounting assembly with fasteners

4.3 Data Acquisition Setup

The voltage and power response of the device were obtained using a frequency sweep program in National Instruments LabVIEW 2009. Input vibration velocity data was obtained using a B&K Type 8001 impedance head attached to the actuator attachment shown in Figure 31. This is a single direction contact accelerometer only capable of measuring accelerations in the z-direction (vertical). Signal amplification and preconditioning was required in order to be recorded using the data acquisition hardware. This was done using a B&K Type 2635 charge amplifier set to a transducer sensitivity of $3.47 \frac{\text{pC}}{\text{m/s}^2}$, and output units of $1000 \frac{\text{mV}}{\text{UnitOut}}$ with the output units set to 0.01m/s . This amplified signal was then measured using a National Instruments M Series 6251 PCI DAQ which has an input impedance of 10 GΩ in parallel with a 100pF capacitance. CH0 was used to record the impedance signal while the voltage output from the PZT was recorded on CH1. Both measurements were made in differential mode.
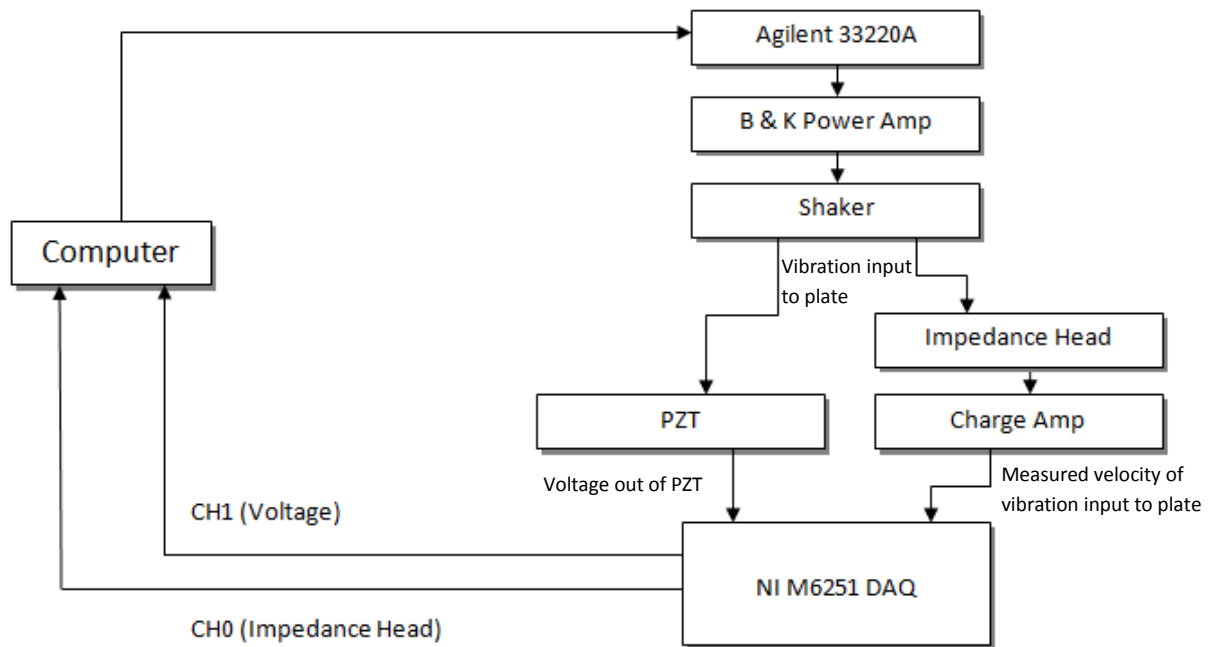
Figure 33 Voltage and power data acquisition flow chart

Additional surface vibration velocity data was also obtained from the plate using a Polytec OFV Fiber

Interferometer connected to a Polytec OFV 3001 Vibrometer Controller. This device uses a focused laser

to measure velocity or displacement at any point on the plate. The capabilities of this setup were further

enhanced by mounting the laser to two linear actuators connected to a Newport ESP300 Universal

Motion Controller which allows the laser to be moved very precisely within a 50 mm^2 area. In

conjunction with a slot scan program written in National Instruments LabVIEW 2009 this setup was used

to collect velocity data for multiple frequencies and points on the plate.
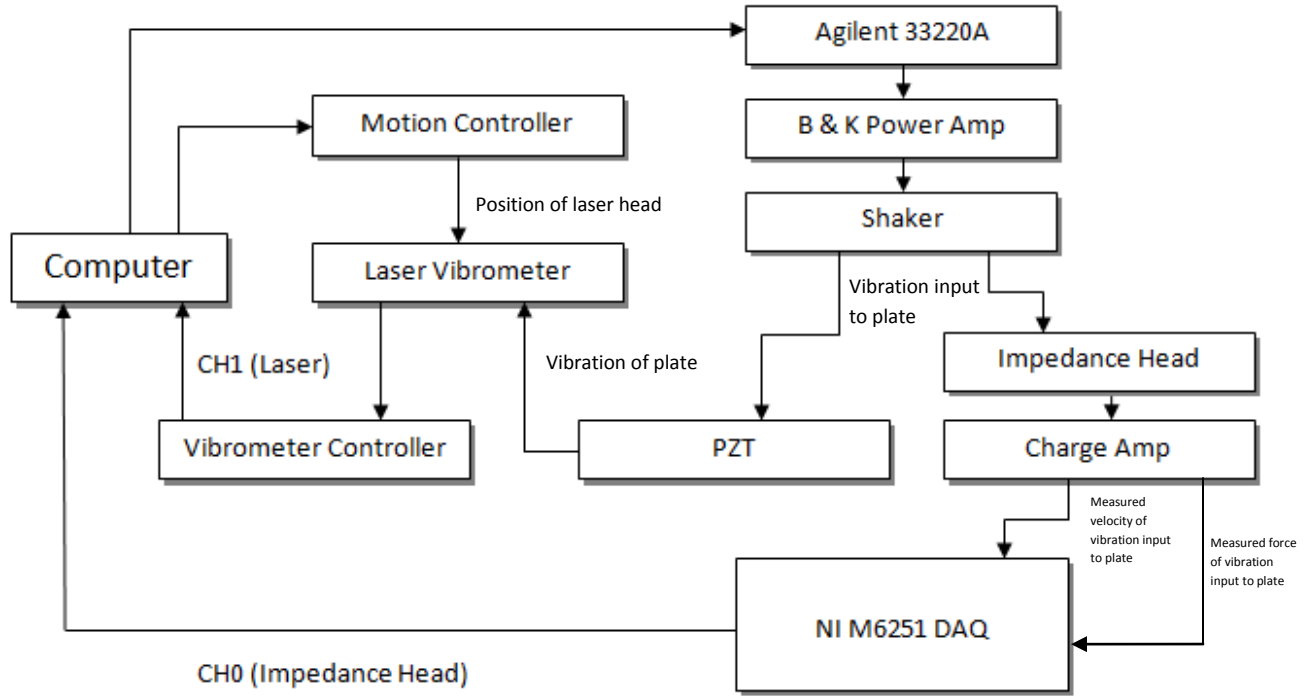
Figure 34 Laser scan data acquisition flow chart

A secondary B&K Type 2635 charge amplifier was set up to take advantage of the impedance head's

ability to collect Force data as well. This amplifier was set to a transducer sensitivity of $3.86\dfrac{\text{pC}}{\text{m}/\text{s}^2}$.

However the manual for the impedance head requires that for force data acquisition the transducer

sensitivity be $386\dfrac{\text{pC}}{\text{N}}$, since the charge amplifier cannot be set to this value the output units were set to

be $1\,\text{m}/\text{s}^2$. Because the charge amplifier was designed for acceleration data acquisition the voltage is

not integrated when the output units are set to m/s^2 so this can easily be replaced by N and the

resulting data scaled to account for the factor of 100 discrepancy in the transducer sensitivity.

A LabVIEW script was used to run an Agilent 33220A Function Generator in order to generator

the desired frequency sweep input for the B&K Type 4809 small vibration exciter. However the signal

from the function generator was not sufficient to drive the vibration exciter it was therefore first routed

through a B&K Type 2706 power amplifier in order to generate a large enough signal. Provided that a

clean output signal was obtained from the impedance head and the PZT there was no need to measure

or set the amplification parameters on the power amplifier. The impedance head serves as a

measurement of the input (velocity and force) vibration levels.

Since the outputs from each of the devices was a voltage, a conversion factor was required in order

to calculate the correct values in the desired units, this is shown in Table 5.

	Conversion Factor
Impedance Head (Velocity)	$100\,\dfrac{\text{V}}{\text{m/s}}$
Impedance Head (Force)	$10\,\dfrac{\text{V}}{\text{N}}$
Laser	$0.005\,\dfrac{\text{m/s}}{\text{V}}$

Table 5 Table of conversion factors

4.4 Experimental Setup

Beyond mounting the piezoelectric plate in a position that allowed for clamping it as an

exponentially tapered plate, it was also necessary to mount the assembly in a position where the

actuator attachment could be mounted, and the mounting assembly would be as rigidly fixed as

possible. A mounting structure was built using aluminum supports as seen in Figure 35. The height of the

mounting assembly was adjusted to accommodate the shaker, impedance head and actuator

attachment beneath it.
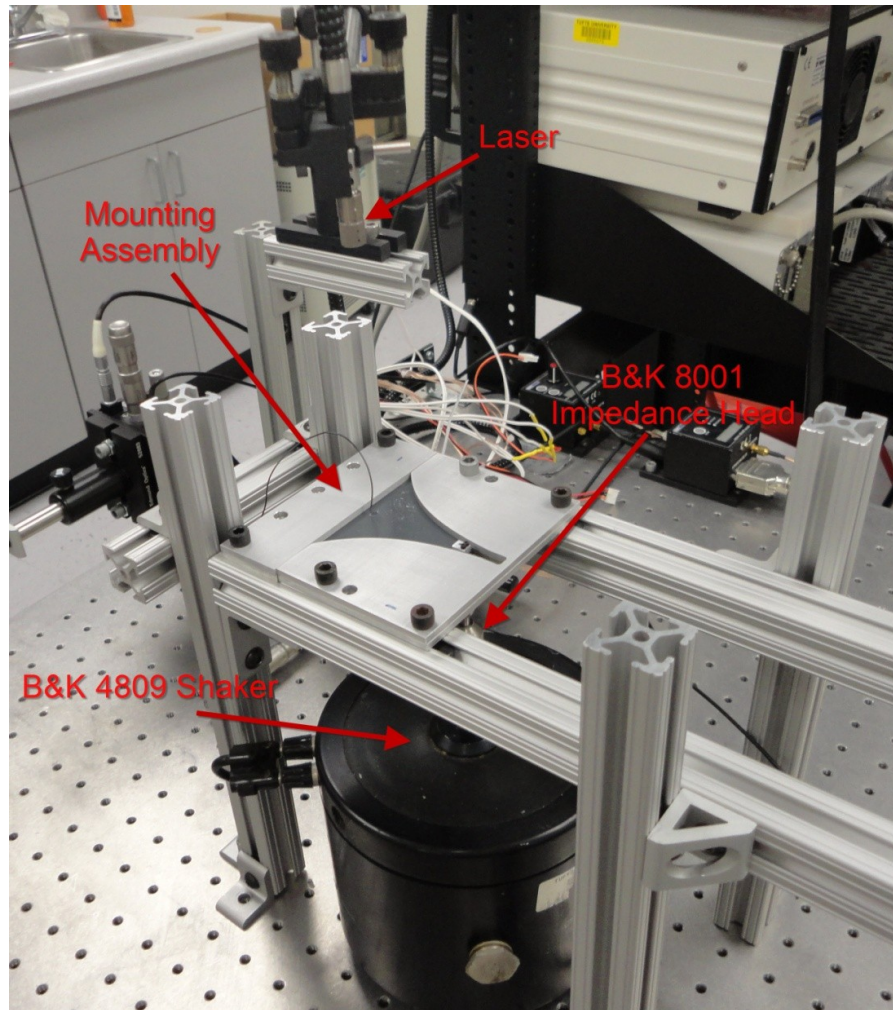
Figure 35 Experimental setup 1
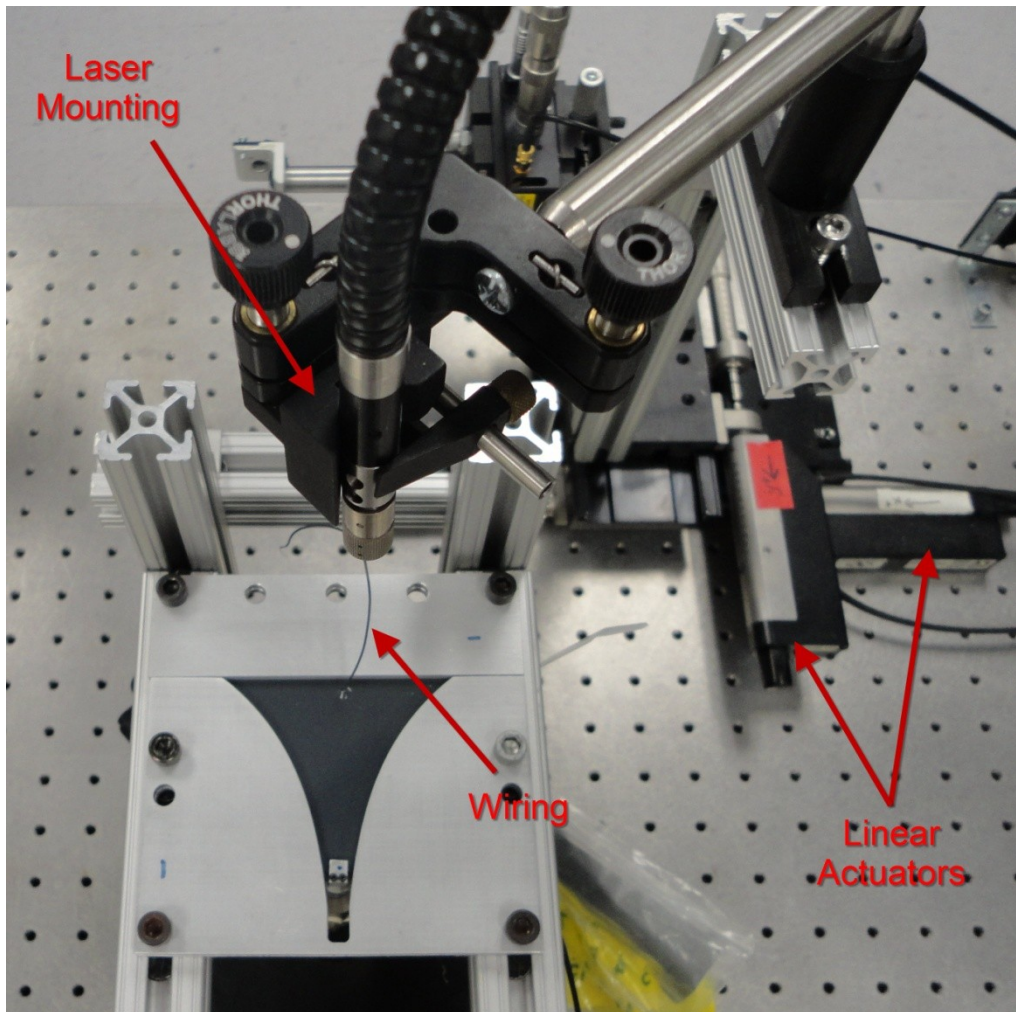
Figure 36 Experimental setup 2

During initial testing of the experimental setup it was determined that the gap left to accommodate the thickness of the plate did not fully clamp the plate within the mounting assembly. To resolve this issue, epoxy was used to fix the plate to the main part of the mounting assembly. The wide end of the plate was left free so that the experimental setup only clamped the two exponentially tapered sides of the plate.

The following experimental trials were run and results will be presented in the following section:

1. Voltage vs. Frequency

2. Displacement vs. Frequency at points along centerline

3. 2D Displacement scan of entire plate with Input vibration

4. 2D Displacement scan of entire plate with Input Voltage (electrically driving the PZT)

5. Power Output vs. Frequency for several load resistance values

4.5 Results

This section presents the results obtained for a number of different experimental trials each using all or a portion of the overall experimental setup apparatus, where applicable further setup details will are provided. For the results showing displacement plots it is important to note that while the goal was to obtain plots for the resonant frequencies obtained from simulation a problem with the reflective paint used to improve the signal quality from the laser was encountered where the paint began to produce bubbles on the surface of the plate which scattered the incoming laser and greatly reduced the returned signal. This limited the number of scans that could be preformed and we were forced to use data from non-resonant frequencies as our comparison to the simulation results for these plots.

4.5.1   Voltage/Input Acceleration vs. Frequency

The first experiment run was to obtain the voltage frequency response of the device. The results are shown in Figure 37 This data was normalized by the input acceleration since the displacement on the shaker varied significantly with frequency. This can be seen in Figure 38.

In the voltage output plot we can clearly see areas of increased output, these are the resonant frequencies of the plate and although they do not match the simulation results exactly we can see that they are reasonably close. At around 1200 Hz we see a very low output. This is likely an error in the data since it is several orders of magnitude lower than any of the other data points and can be ignored.
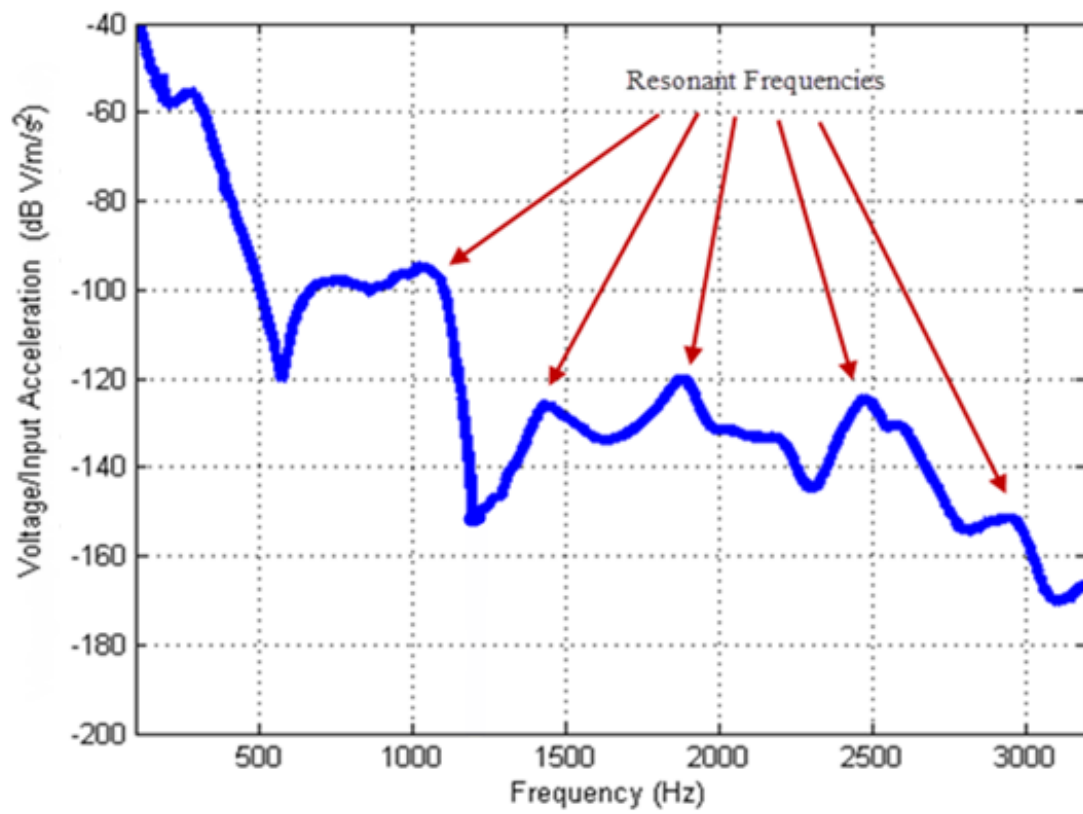
Figure 37 Voltage/Input Acceleration vs. Frequency (Experimental)
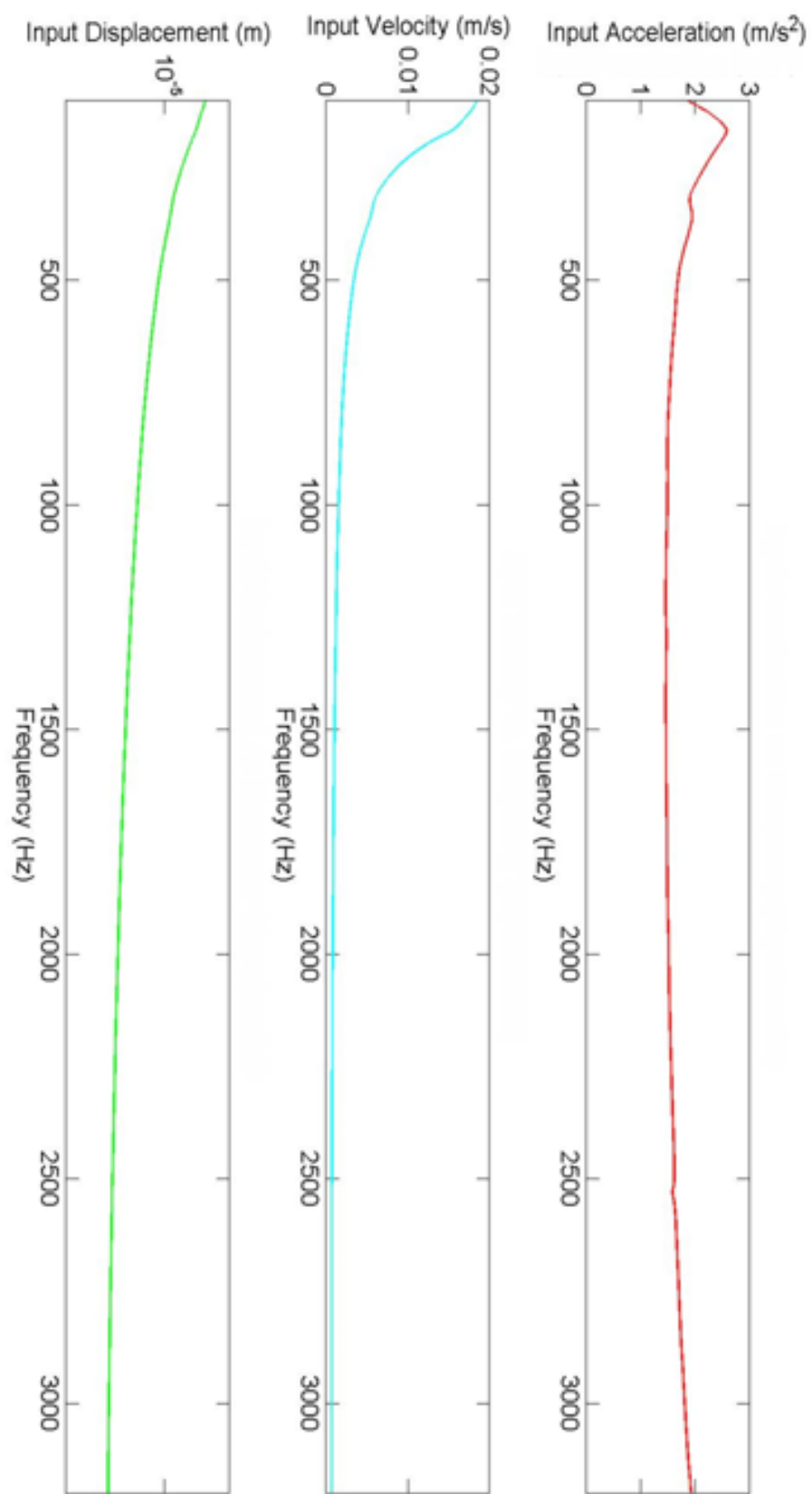
Figure 38 Acceleration, velocity and displacement vs. Frequency (Experimental)

4.5.2 Displacement vs. Frequency at points along centerline

In order to see how the displacement of the device varied along the plate the next experiment was set up using the laser vibrometer to measure the displacement of the plate at five points along the plate including one at the input allowing for a comparison between the vibrometer and impedance head accelerometer. The displacement data along the plate is shown in Figure 39. Close to $x = 0$in we only the effect of the input displacement which is to be expected. As we move along the length of the plate there are certain frequencies that induce increased displacement at different locations. This is particularly visible at $x = 1.5$in and $x = 1.0$in, which is the effect that we are looking for since we are looking for a broadband response.
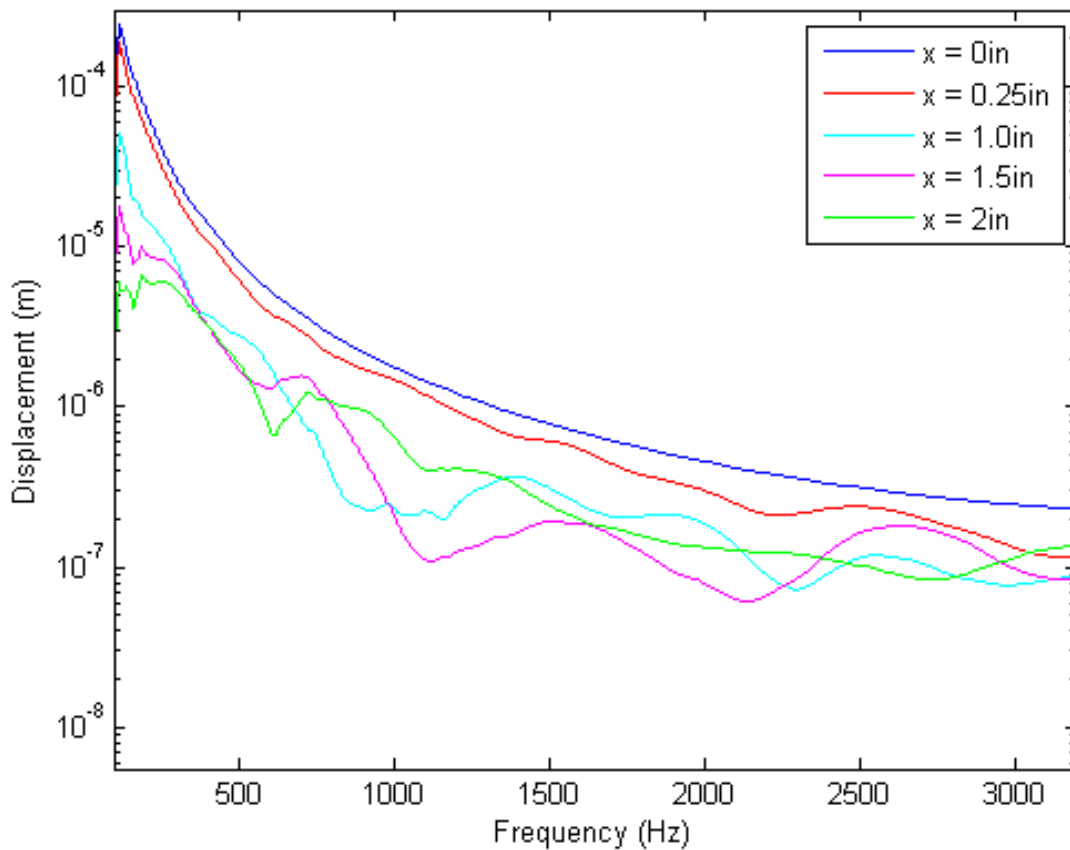
Figure 39 Displacement vs. Frequency at multiple points along center line

In Figure 40 a comparison of the laser data and the impedance head data is shown and we can see that they match fairly well except at the low end of the frequency range where the laser data seems to show a significantly higher velocity.
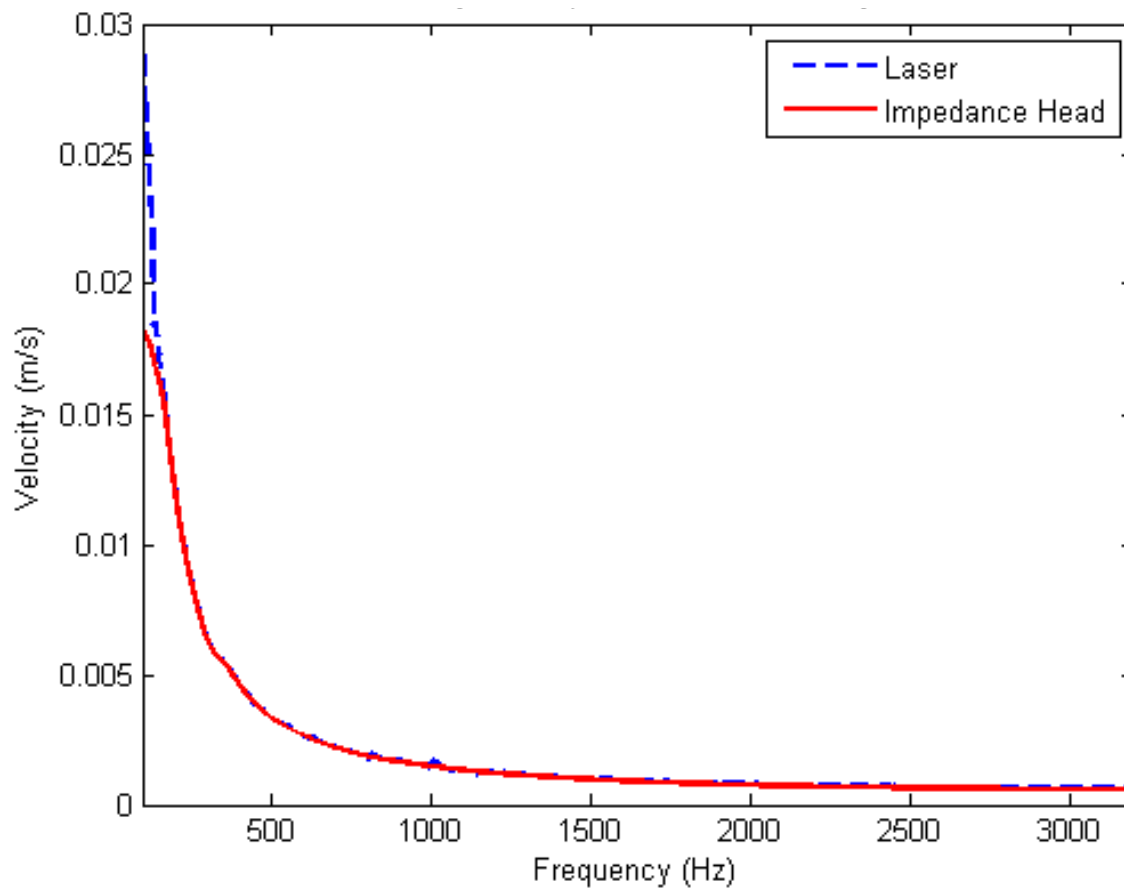
Figure 40 Comparison of velocity data from laser and Impedance head at x = 0
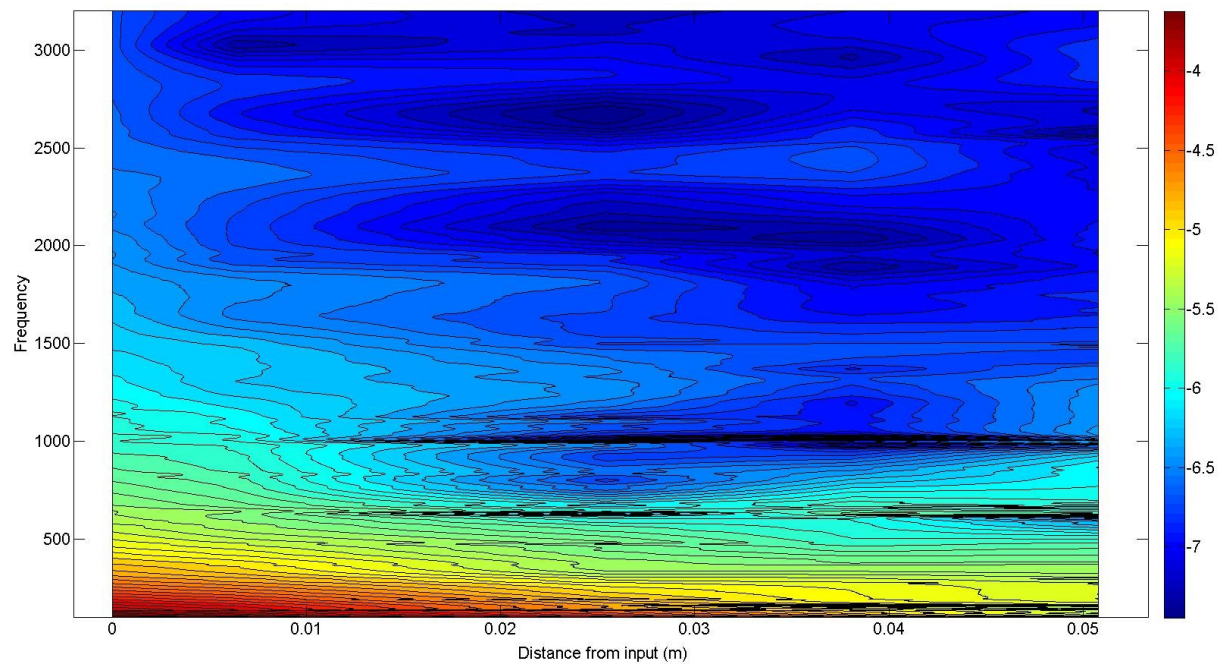
Figure 41 Contour plot of vibration displacement vs. frequency and distance from input at centerline

Finally all of the data is combined in a contour plot showing the log of the displacement along the plate for all frequencies. Again we can clearly see that at low frequencies maximum displacement is near the input. We also see that as the frequency is increased areas of increased displacement can be seen further along the length of the plate, although the maximum displacements are always at low frequency regardless of distance from the input.

4.5.3   2D Displacement Plots with Input Acceleration

The next set of data utilized the laser along with two linear motors to obtain a two dimensional scan of the plate surface showing displacement vibration amplitude for the entire plate at several frequencies. Only half of the plate is shown since the range of motion of the linear motor was limited to a 50mm x 50mm square. However, because the plate is symmetrical only one half is needed to fully define the response, similar to what was done in COMSOL®. The area that was scanned by the laser is shown in Figure 42
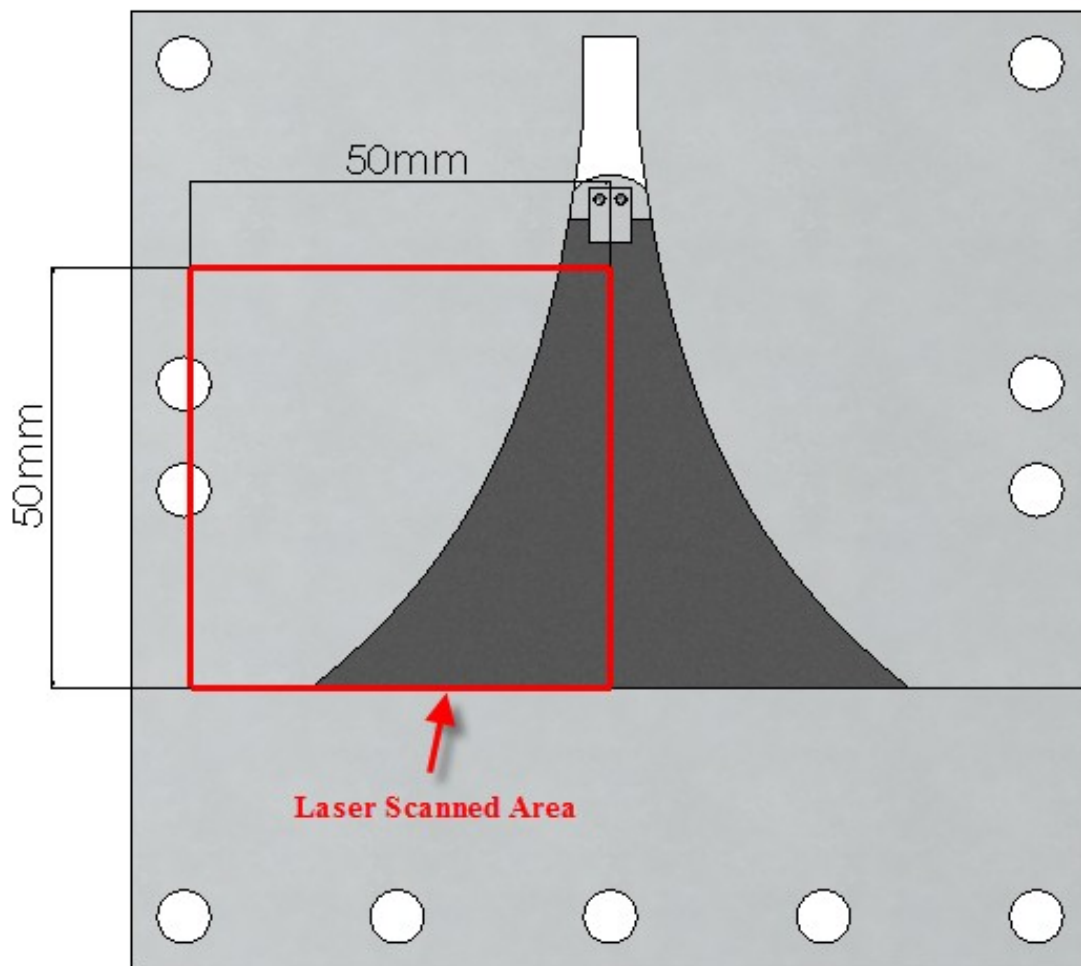
Figure 42 Area scanned by laser

In all cases the white dashed line represents the edge of the plate. These results are shown in Figure

43

Figure 43 Vibration displacement plot at 100 Hz (Experimental)
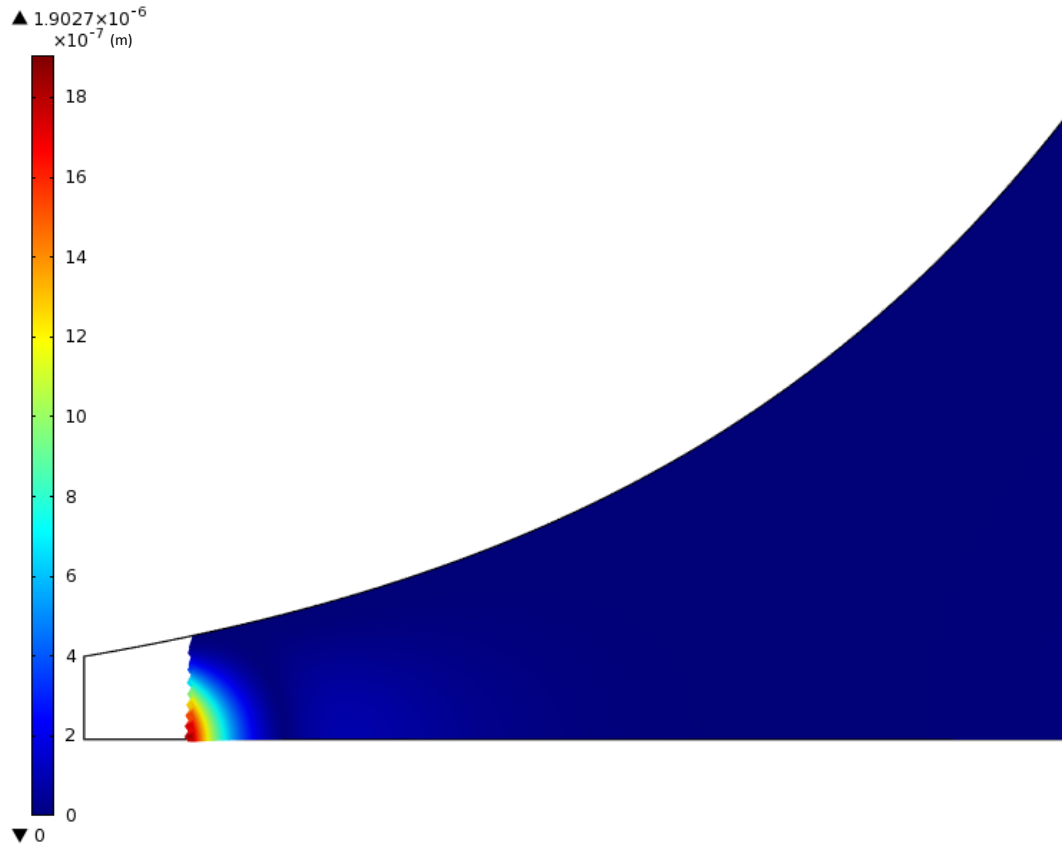
Figure 44 Vibration displacement plot at 100 Hz COMSOL®

We can see from Figure 43 the evanescent wave effect as the displacement quickly drop off as we move away from the input source. This is mirrored in Figure 44 for the simulation results. Although the displacement shape is a good match to the simulation results the magnitude is significantly higher in the experimental result though still within an order of magnitude. This could be the result of the difference in the apparent resonant frequencies of the plate in reality versus what was obtained from COMSOL®. As a result the following sets of results will be compared with the COMSOL® plots for resonant frequencies rather than with identical frequency plots.
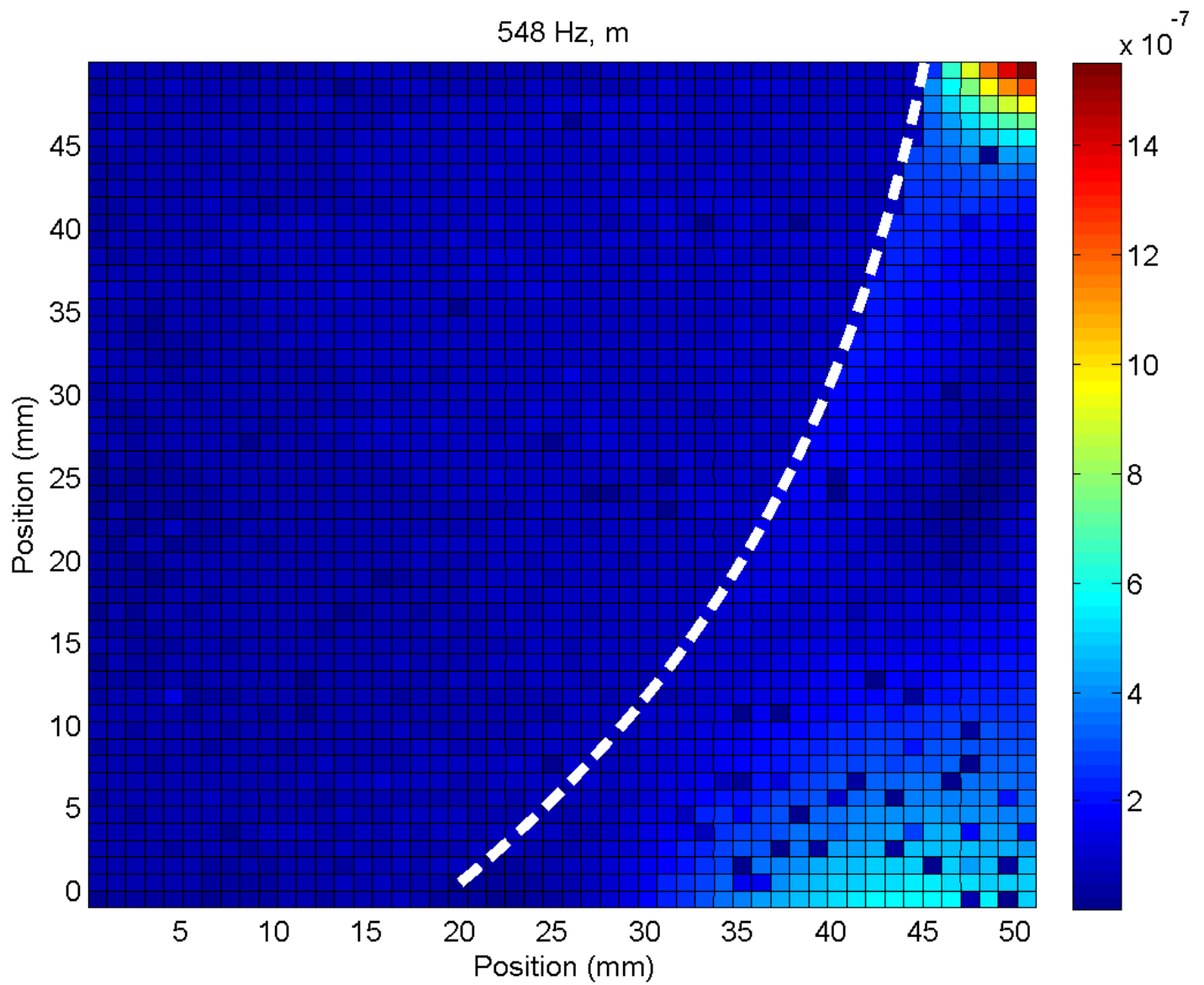
Figure 45 Vibration displacement plot at 548 Hz (Experimental)
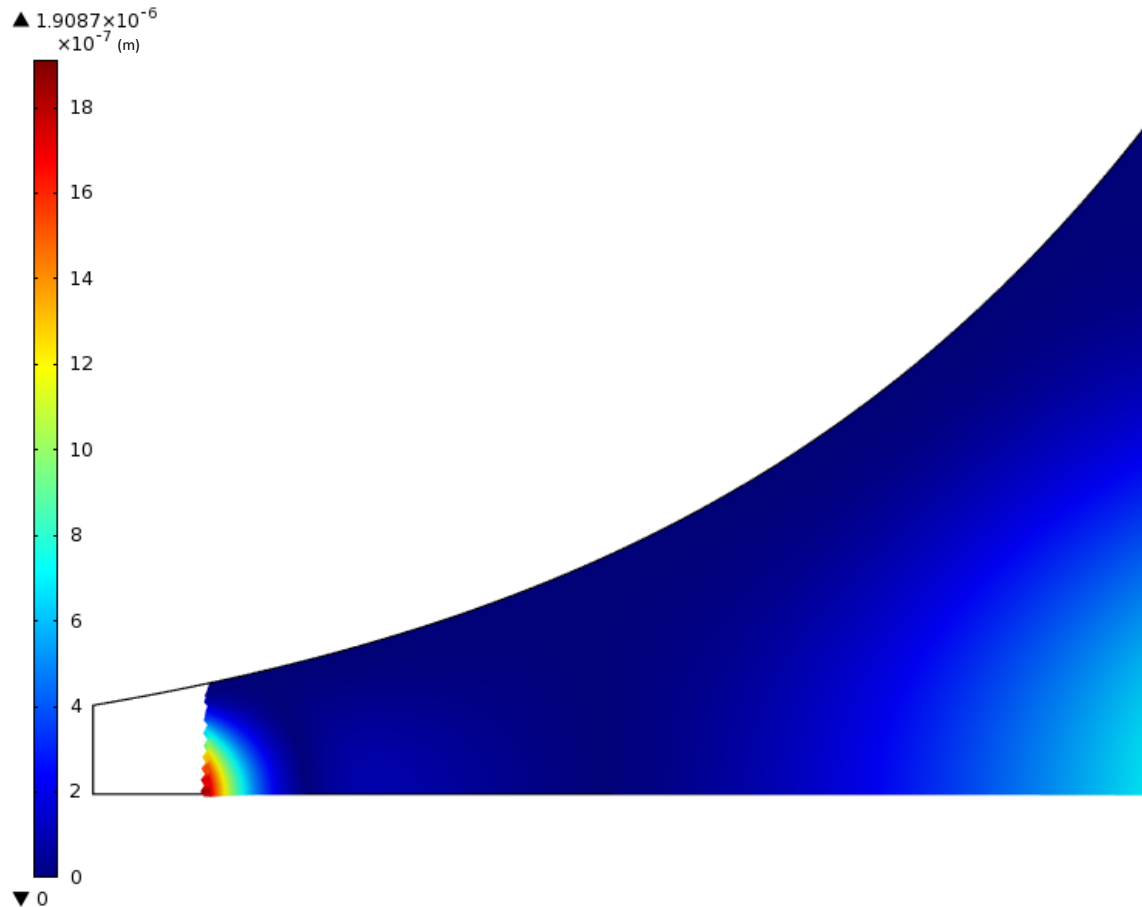
Figure 46 Vibration displacement plot at 400 Hz from COMSOL®

In this next set of results (Figure 45 and Figure 46) the displacement plots at two different

frequencies are compared to show that there is a discrepancy in the simulated resonant frequencies

versus the experimental results. It can be seen that the displacement plots for these two frequencies are

very similar in both shape and in magnitude with COMSOL® showing a maximum displacement of 1.9 x

10^{-6}m and the experimental results being approximately 1.5 x 10^{-6}m. It is not surprising that the resonant

frequencies do not match exactly since not all the material properties are precisely know, and the

clamping structure is not perfectly rigid. However, the frequency is not far off and the displacement

pattern and amplitude are well matched.

Figure 47 Vibration displacement plot at 1282 Hz (Experimental)
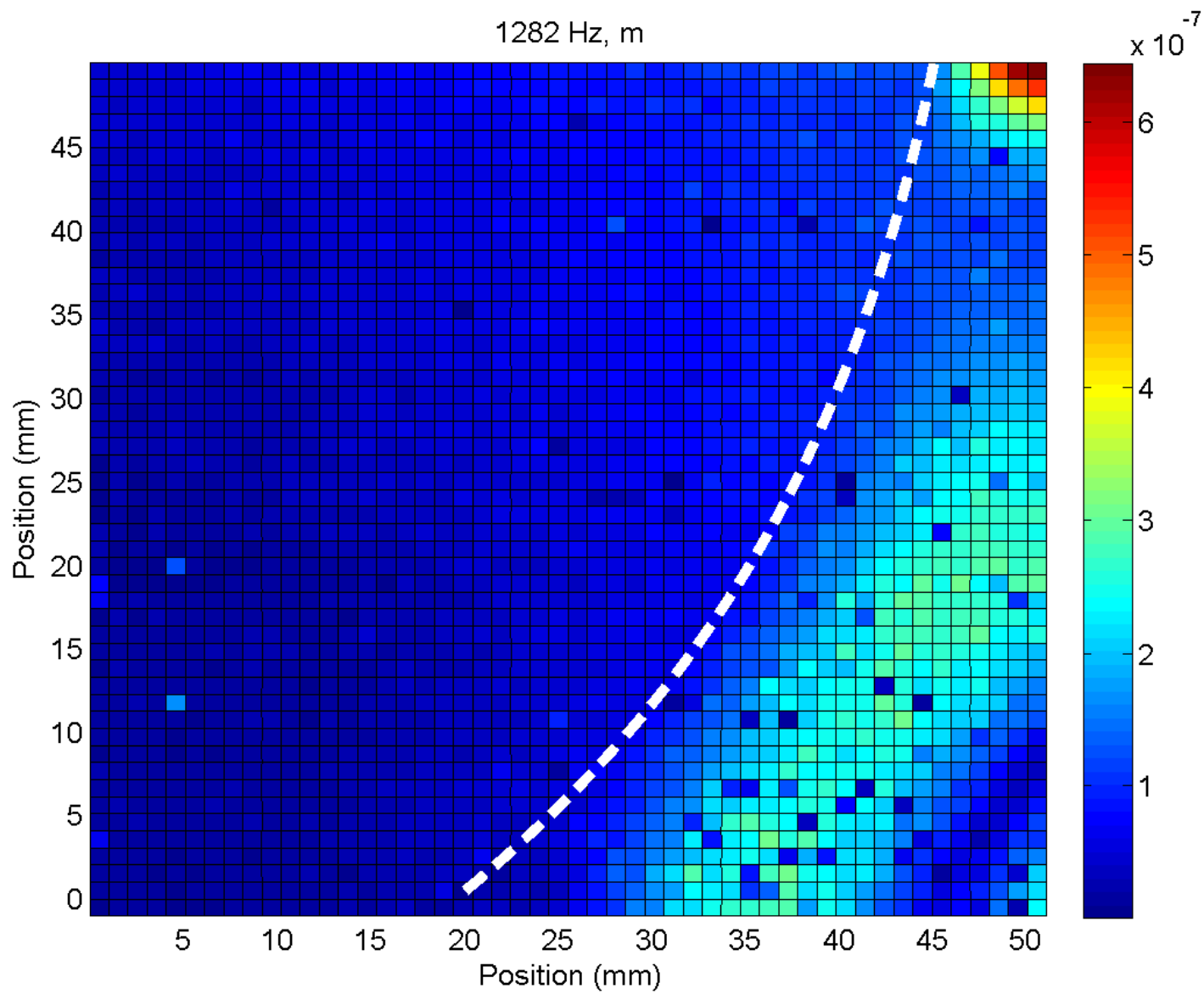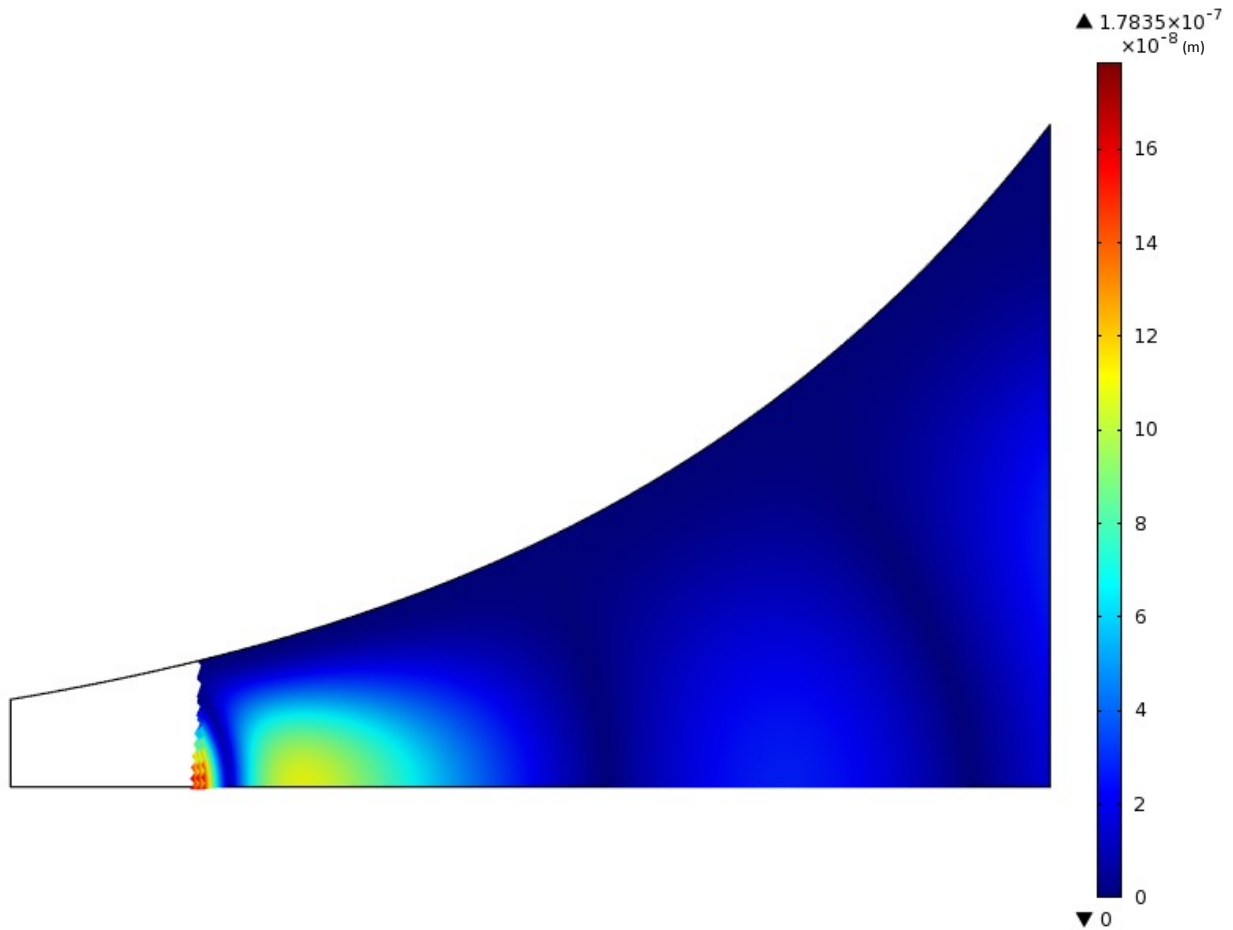
Figure 48 Vibration displacement plot at 1282 Hz COMSOL®

Figure 48 shows the displacement plot at 1282Hz obtained from COMSOL®. We can see that now the displacement plot begins to differ significantly from the experimental results for the same frequency. This could be partially due to the shift in resonant frequencies that is indicated by the results shown in Figure 46 and Figure 45. However it is likely also the result of energy propagating through the mounting assembly itself and therefore being transferred to the plate through the sides rather than strictly at the input as assumed by the simulation results.
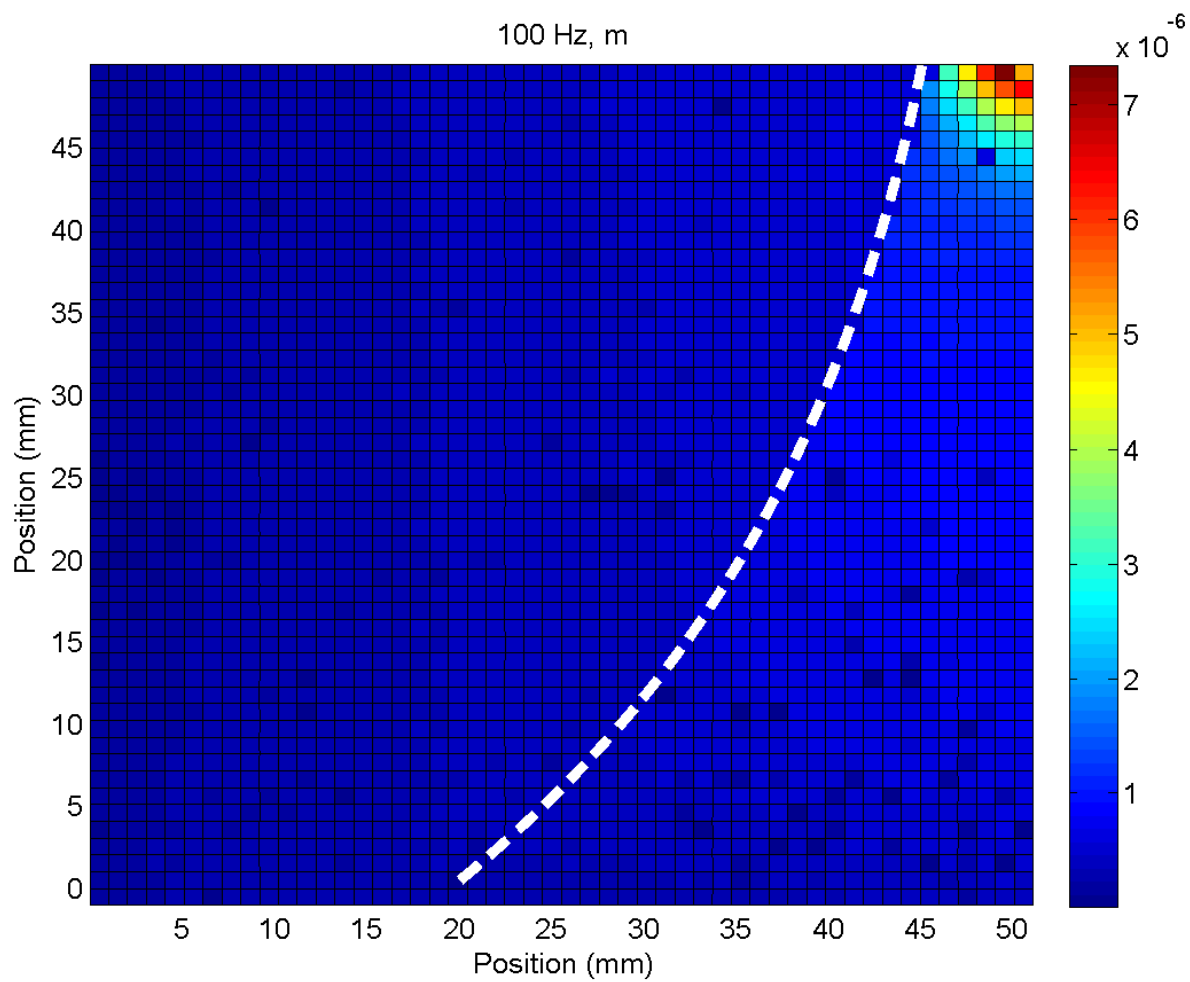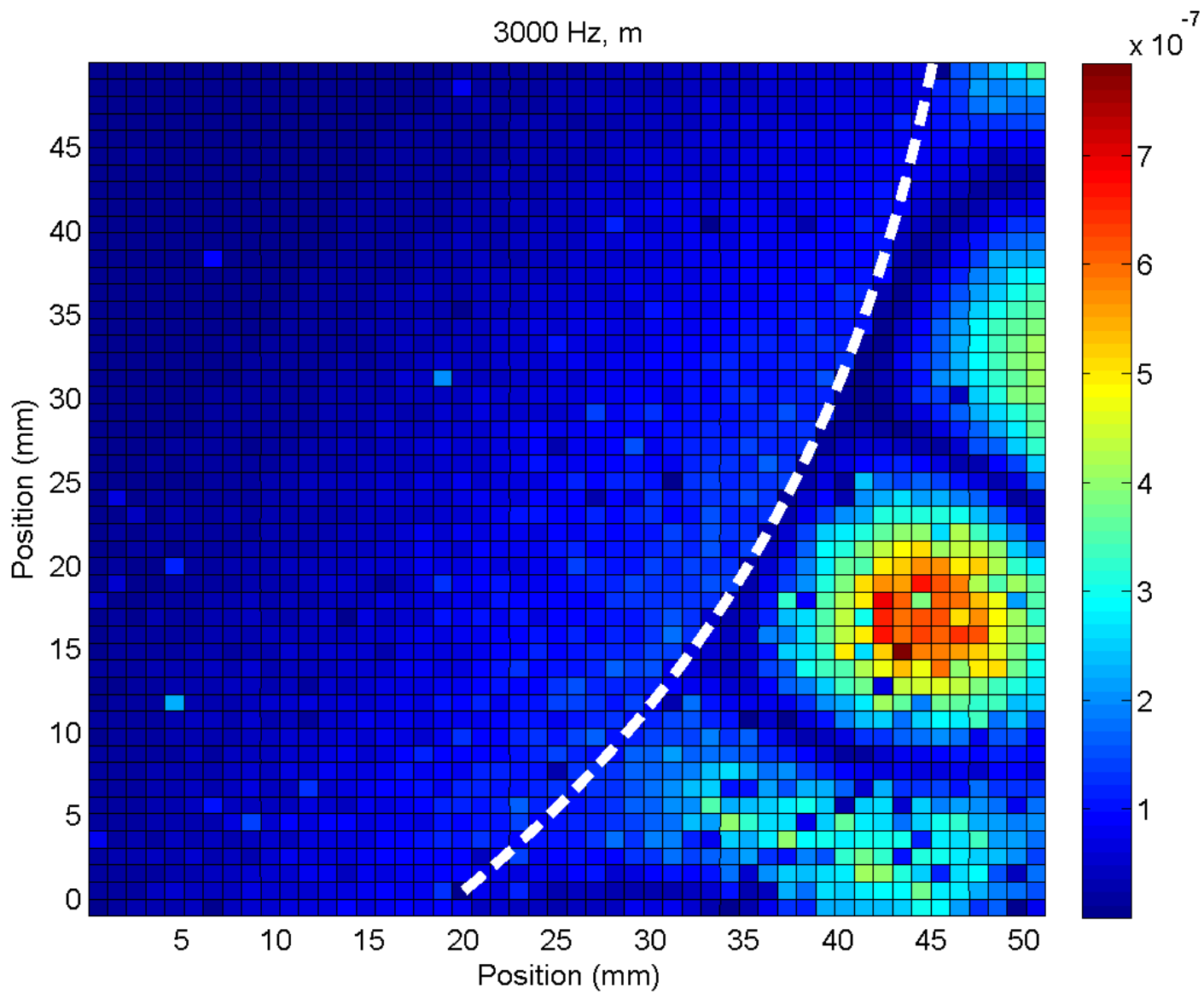
Figure 49 Vibration displacement plot at 3000 Hz (Experimental)
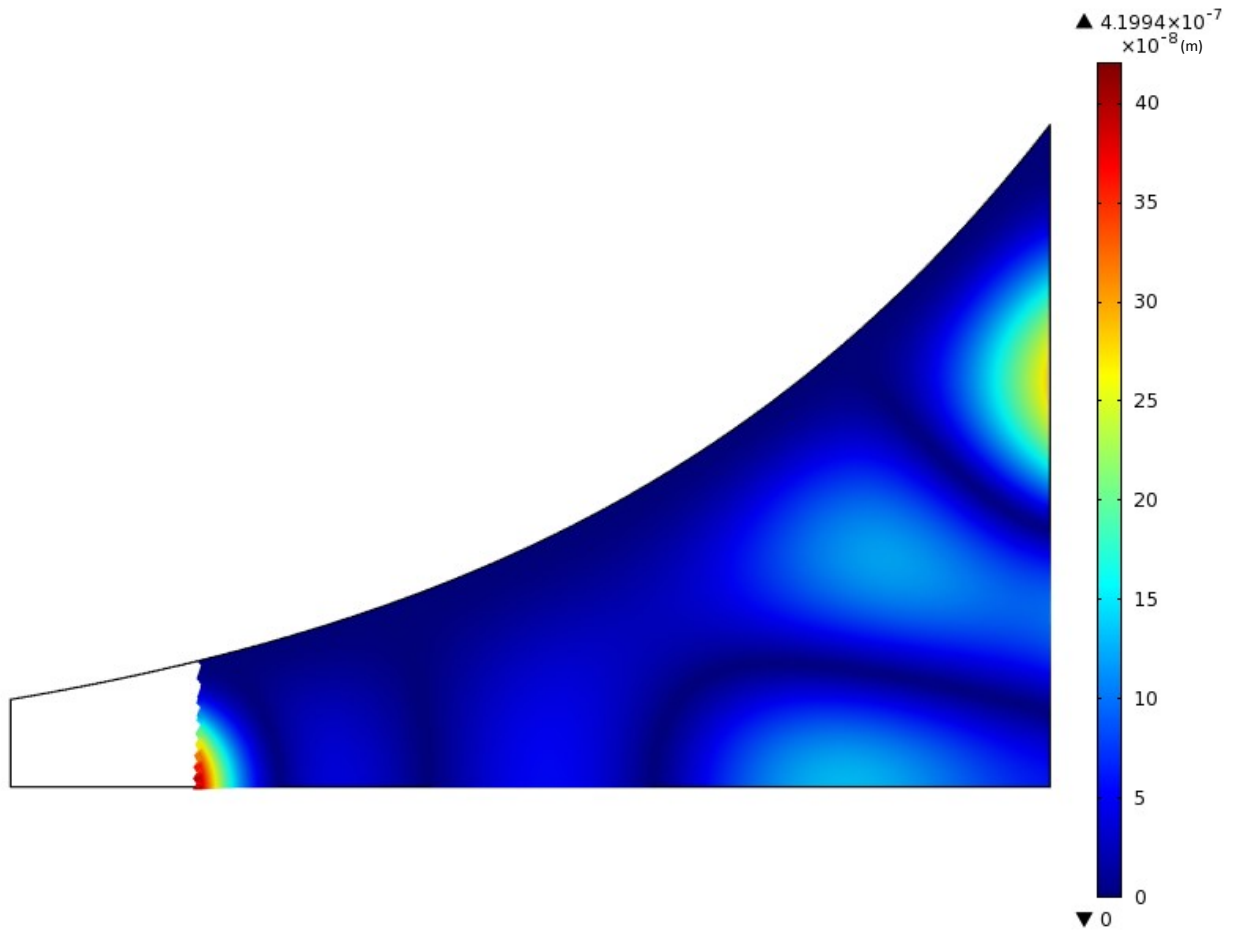
Figure 50 Vibration displacement plot at 3000 Hz COMSOL®

Figure 49 and Figure 50 further emphasize the different in the simulation and experimental results, it seems that as the frequency increases the similarities between the plots decreases. The next set of plot aims to show that this is in fact largely due to issues with directing the energy at the input through only the plate rather than the mounting assembly. To do this we took advantage of the converse effect and applying a voltage to the plate and plotting the displacement compared to the same setup run in simulation. This should be less affected by non-ideal mechanical boundary conditions.

4.5.4   2D Displacement Plots with Input Voltage

Due to the evanescence issues when the plate was excited by a mechanical input and the dissimilarities between the displacement plots obtained at higher frequencies for the experimental and simulation results, it was decided to measure the displacement response of the plate to an alternating voltage input applied to the PZT. This makes use of the converse effect, to verify that the difference in response could be the result of energy propagation through the mounting assembly. To do this, the Agilent signal generator was simply connected directly to the plate using the two wires on either side of the plate, replacing the shaker and power amplifier, as shown in Figure 51.
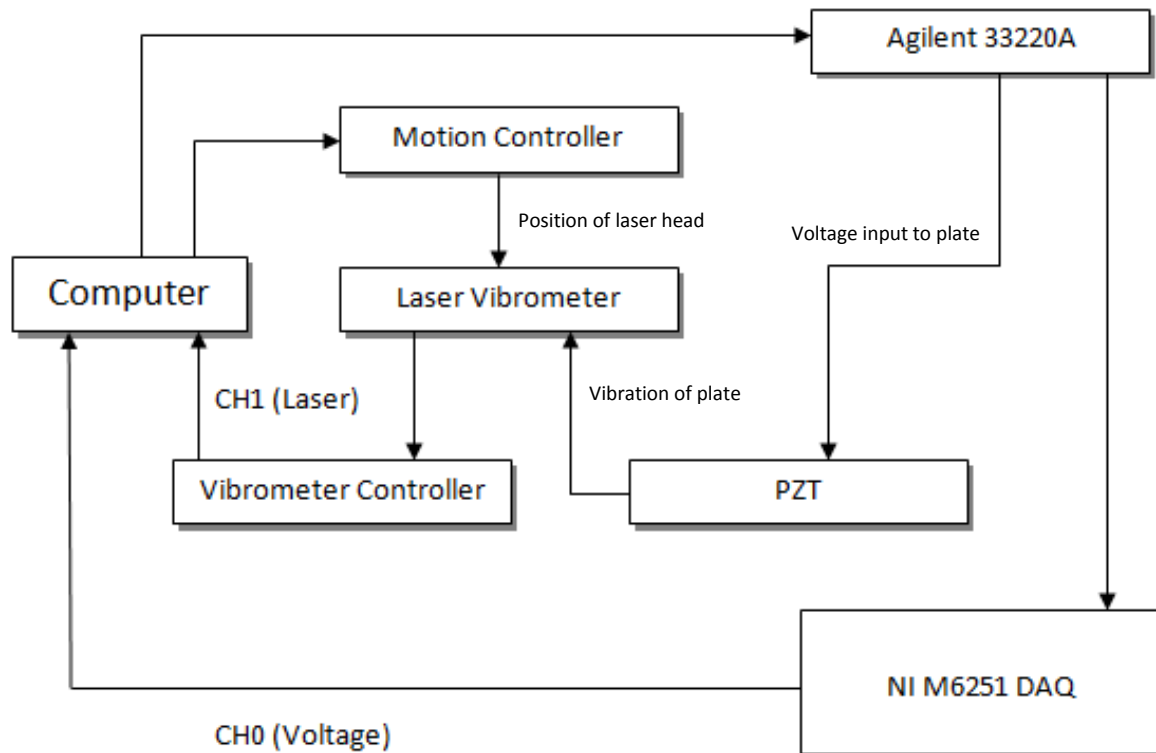
Figure 51 Applied Voltage Data Acquisition flow diagram

These results provide another source of comparison to the COMSOL® model while limiting influence from vibrations that may be introduced from the actuator to the mounting assembly.
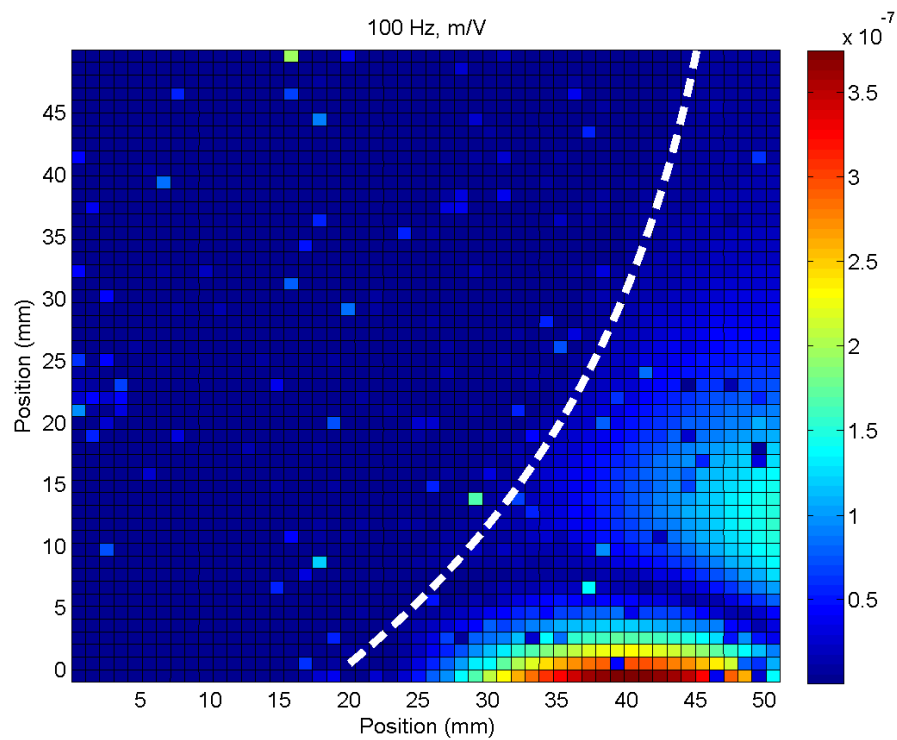
Figure 52 Vibration displacement plot at 100Hz (Experimental) for voltage input
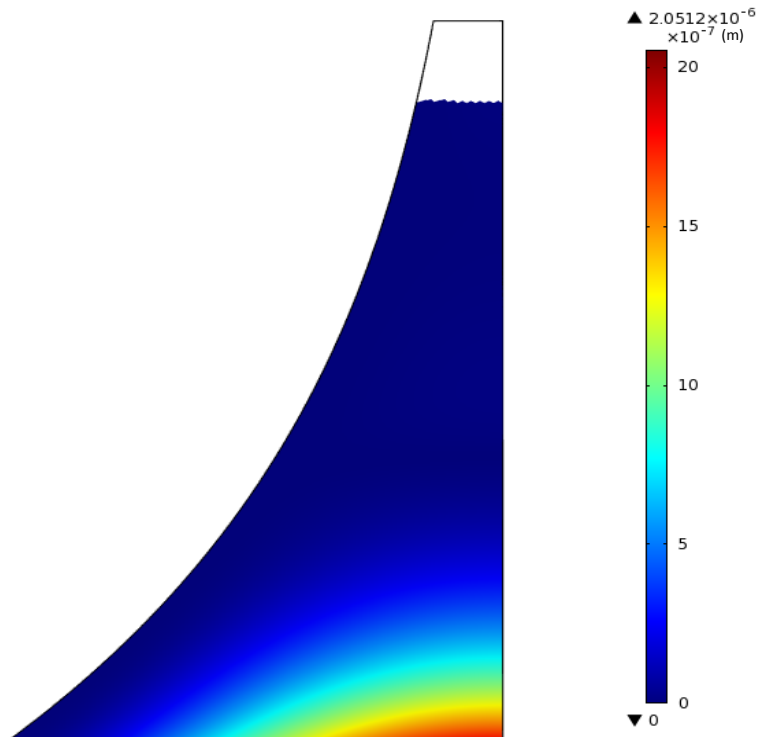
Figure 53 Vibration displacement plot at 100 Hz (COMSOL®) for voltage input

Figure 52 and Figure 53 compare the low frequency response of the plate. We can see that there is some similarity between the simulation and experimental results. The maximum displacement is now at the wide end of the beam for low frequencies, as we would expect.
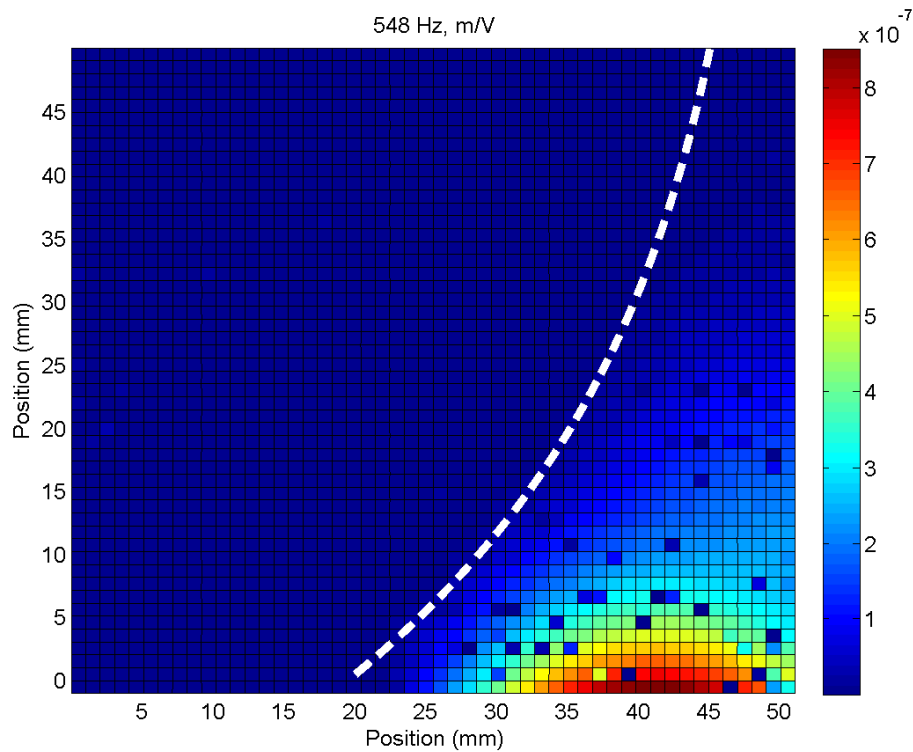
Figure 54 Vibration displacement plot at 548Hz (Experimental) for voltage input
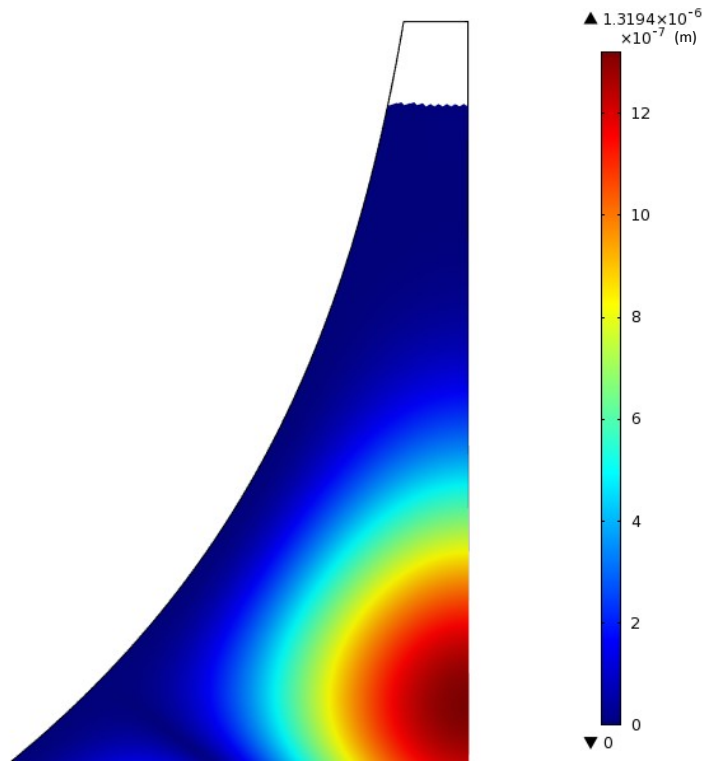
Figure 55 Vibration displacement plot at 548Hz (COMSOL®) for voltage input

In Figure 54 and Figure 55 we increase the frequency and again note that the plate is performing

as we would expect with the maximum displacement moving towards the narrow end of the plate. There

is still a discrepancy in the exact shape of the response which may be due to simplifications in the

simulation model or there may still be some transfer of energy to the surrounding mounting assembly.
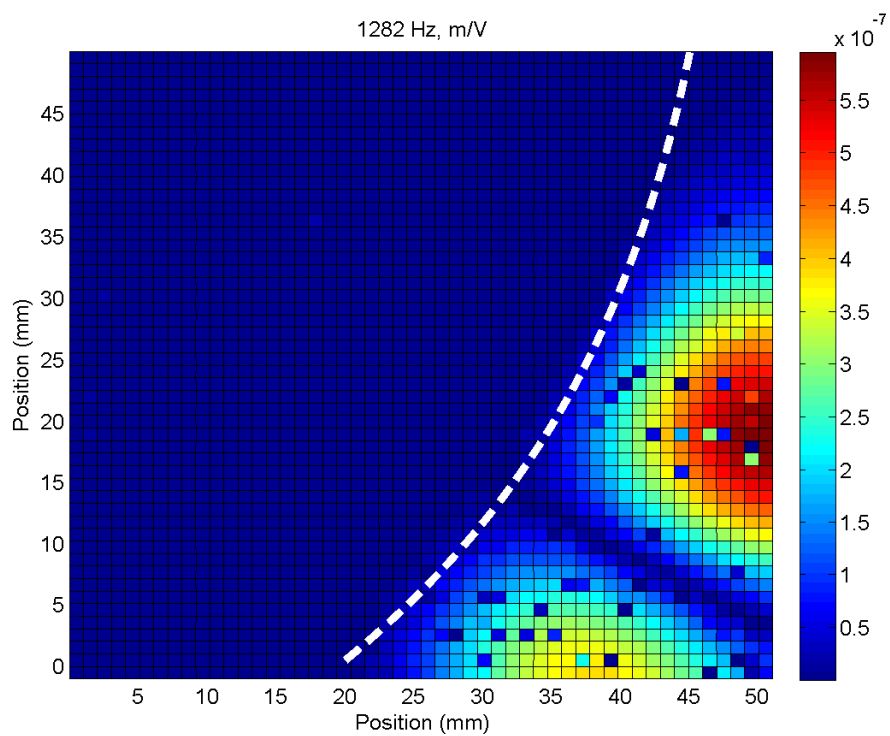
Figure 56 Vibration displacement plot at 1282Hz (Experimental) for voltage input
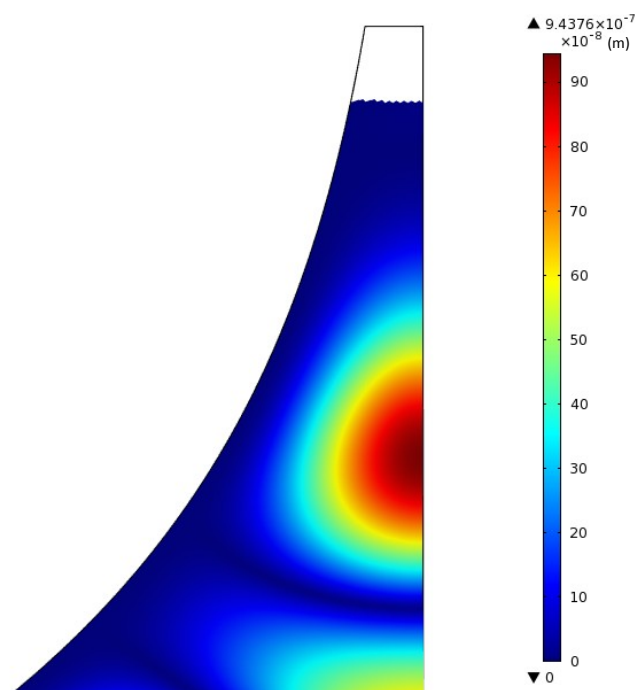
Figure 57 Vibration displacement plot at 1282Hz (COMSOL®) for voltage input

69

Interestingly, as the frequency of the applied voltage is increased the response seen in the experiment seem to align better with the simulation plots. This is most pronounced in Figure 56 and Figure 57. Once again it should be noted that the area of maximum displacement is moving towards the narrow end of the plate.
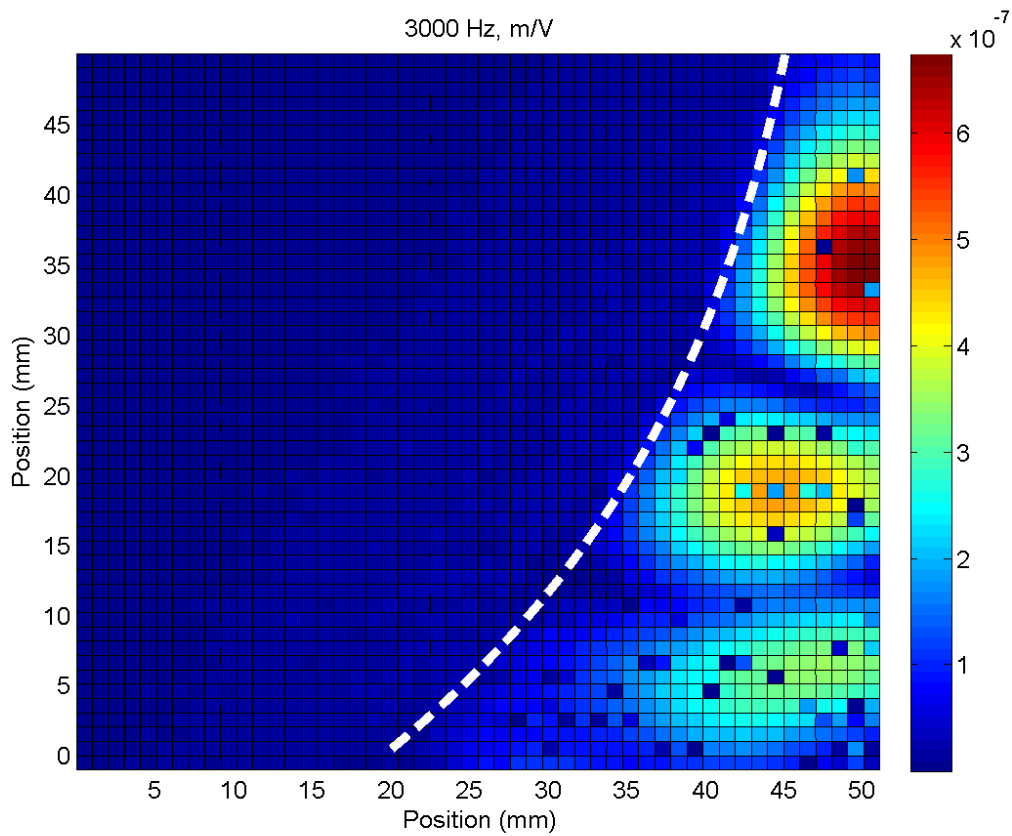
Figure 58 Vibration displacement plot at 3000Hz (Experimental) for voltage input
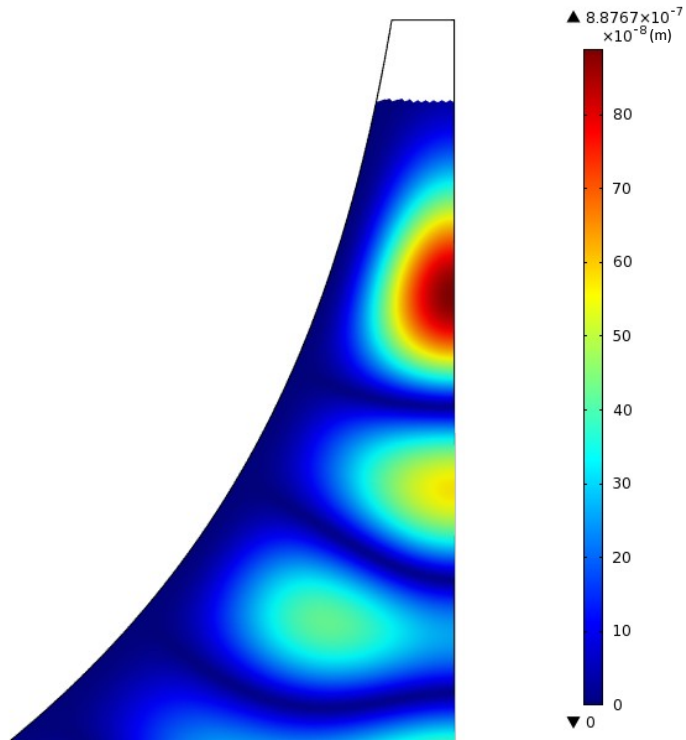
Figure 59 Vibration displacement plot at 3000Hz (COMSOL®) for voltage input

At 3000 Hz

Figure 58 and Figure 59) we again see very good correlation between the shape of the displacement plots and once again the area of maximum displacement has moved further towards the narrow end of the plate. This is a good indication that the underlying theory that the exponentially varying shape of the plate could be used as predicted provided that the material properties of the plate and/or the mounting assembly is altered to prevent the presence of evanescent waves at the input.

4.5.5 Power Output vs. Frequency and load resistance

The results shown in Figure 60 show the power output from the device as it was driven by the actuator for a number of different resistance values. Recall from Figure 21 that the load impedance is important when considering power output. There will be some optimal impedance which will lead to maximum delivered electrical power for a given vibration level. The maximum power obtained for each resistor is shown in Table 6.
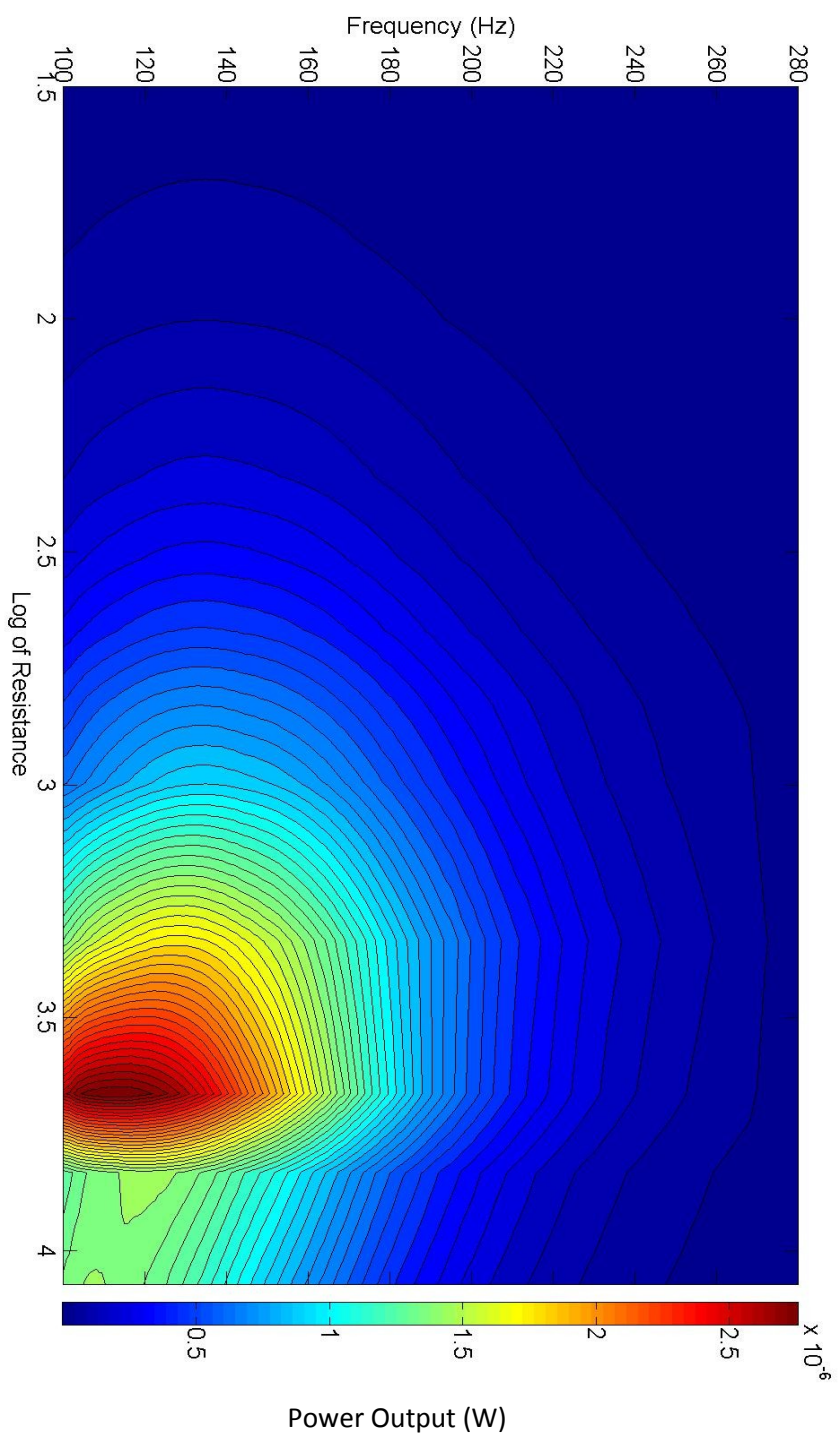
Figure 60 Power Output at low frequencies

Resistor Value (Ω)	Maximum Power (µW)	Frequency (Hz)
2.1	0.002	148
22.5	0.064	154
47	0.136	153
68.1	0.197	153
99.5	0.289	150
218	0.631	151
328	0.946	153
466	1.332	154
673	1.883	152
991	2.472	152
2160	4.489	142
4610	6.334	129
6800	3.432	132
11800	3.086	125

Table 6 Table of power outputs for low frequencies

The same experiment was also run at higher frequencies and the results can be seen in Figure 63. These results are less influenced by the direct actuator input but the power generated is also far less than at lower frequencies where the displacement is higher and is mostly due to the direct input displacement rather than any resonance in the system.

On the next pages the output power is plotted for the three frequencies at which the output power was at a maximum besides the very low frequency response. These are included to show that although we did not get large displacement of the plate at these frequencies we can still see increases in power output corresponding to the resonant frequencies of the plate.
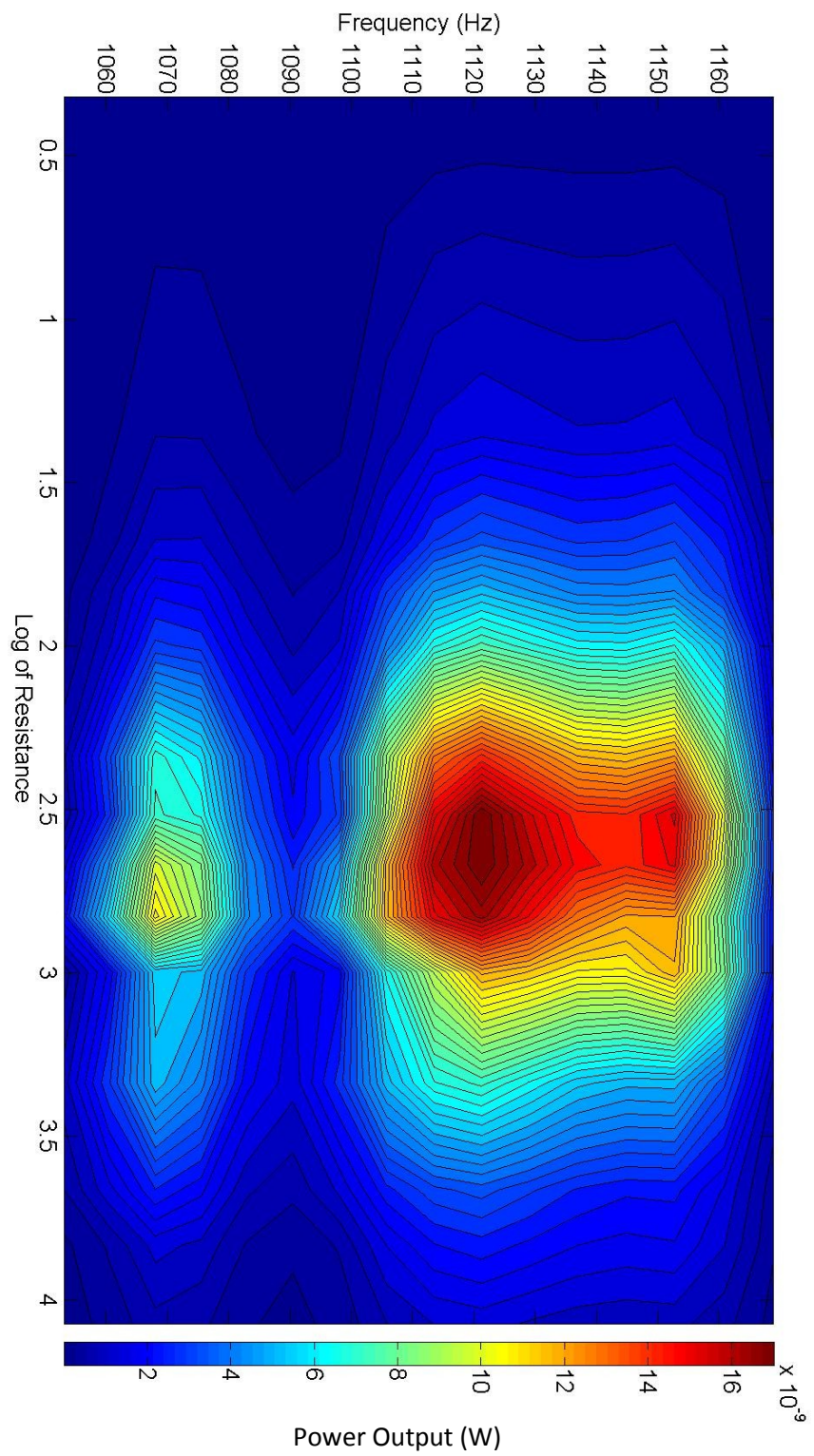
Figure 61 Power output around 1100Hz
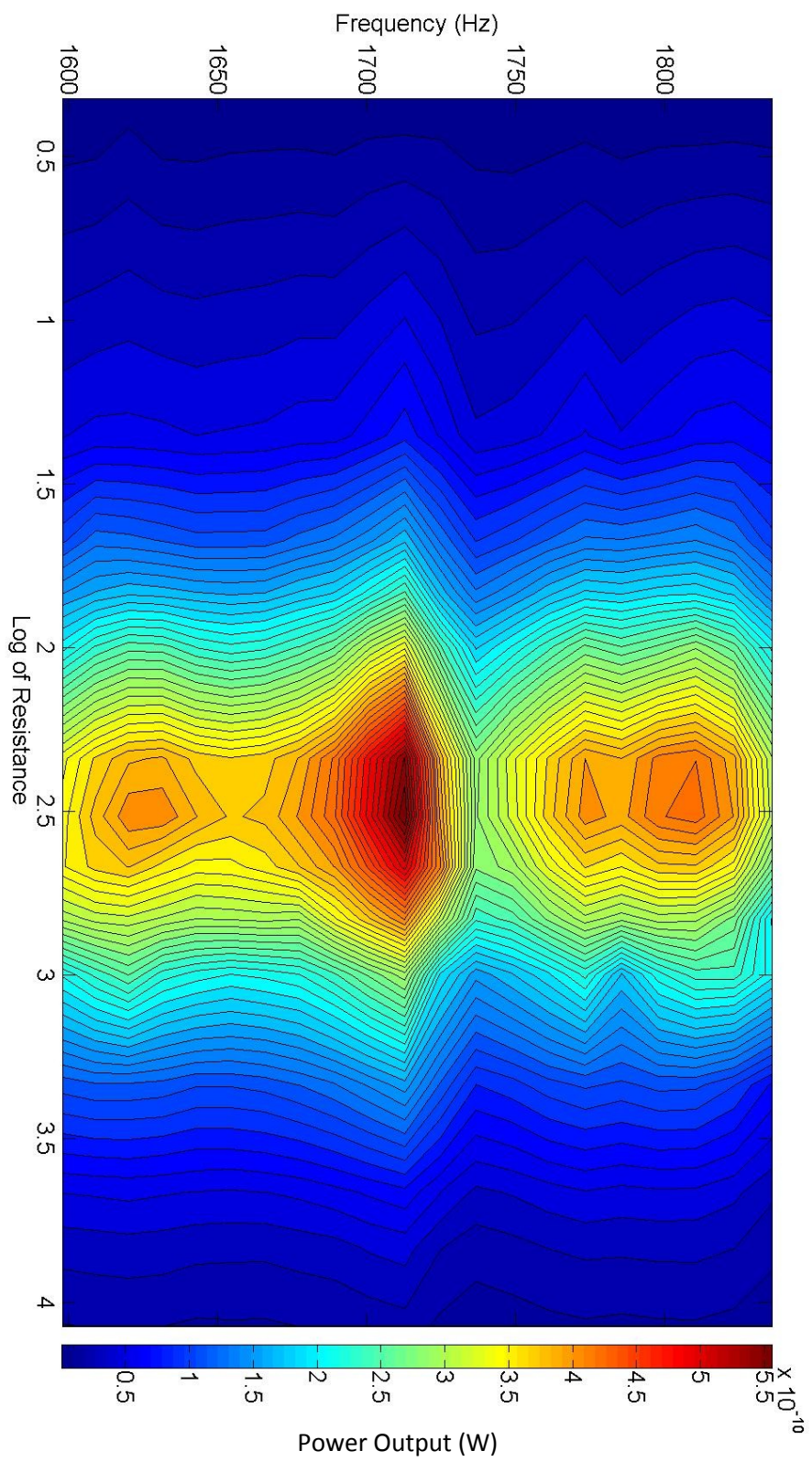
Figure 62 Power Output around 1700Hz
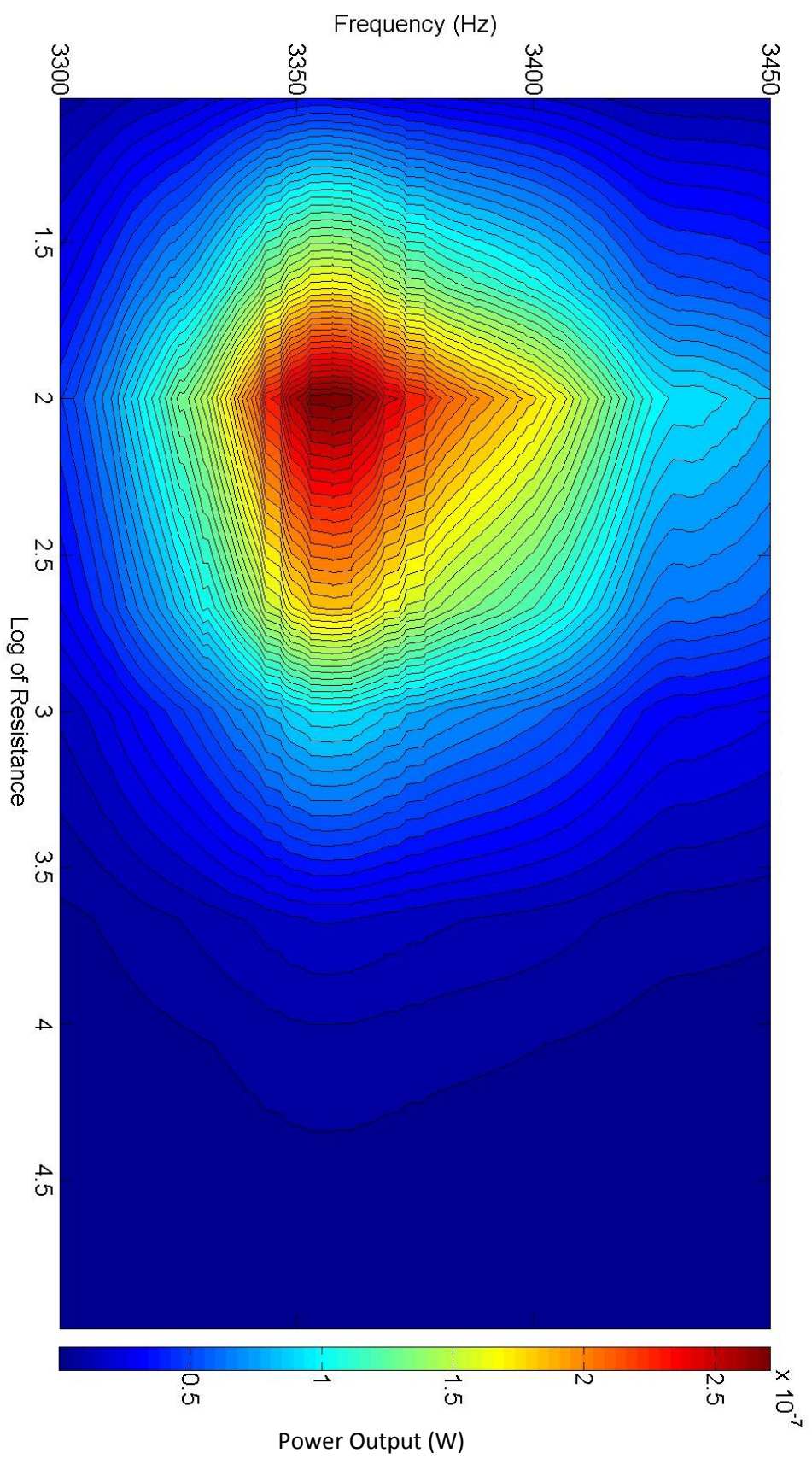
Figure 63 Power Output at over 3000Hz

Resistor Value (Ω)	Maximum Power (μW)	Frequency (Hz)
11	0.0387	3357
44	0.1737	3357
99.6	0.2767	3357
467	0.1857	3357
990	0.0988	3357
4600	0.0223	3357
11600	0.0089	3357
37100	0.0028	3357
63000	0.0017	3357
94000	0.0011	3357

Table 7 Table of power output for high frequencies

Table 7 shows the maximum output power for each of the resistor values tested, the maximum value overall is highlighted. The maximum values for power outputs shown in Figure 61 and Figure 62 have not been put into table form because it can clearly be seen that these are several orders of magnitude lower, than that obtained at 3357 Hz.

4.6 **Discussion**

There are a number of points to discuss related to the experimental results compared to the predicted results from simulation. The first comparison is between the voltage frequency response obtained from COMSOL® and the experimental results. In the simulation results a number of clear resonant peaks are seen in the voltage response plot. In the experimental results we see a reasonable match at frequencies below 500Hz in terms of the shape of the curve but the magnitudes of the experimental results is significantly lower. This difference could be attributed to losses incurred due to damping, which was not included in the simulation, and to vibrations transmitted to the mounting assembly and the mounting structure, which were observed to vibrate noticeably at all frequencies. At the lower frequencies it is likely that this had a slight effect on the location of the peak voltages observed. However, at higher frequencies it seems likely that the vibration modes of the plate mounting and structural assemblies interfered with the natural modes of the plate itself, as energy was transmitted

around the plate and not just through the actuator as intended. A contributing factor is the epoxy used to affix the PZT plate to the mounting assembly. This modified the boundary condition so that a fixed rigid condition may not represent an accurate model of the experimental setup.

There are still peaks that can be observed in the experimental data, although they are not as clear as in the simulation results. These can be seen just before 3000Hz, 2500Hz, 2000Hz, 1500Hz. In addition, between about 700Hz and 1100Hz we see a range in which the voltage output remains relatively constant. (Figure 37)

Next we have the single point laser data results which give an indication of how the displacement of the plate varies along the center line of the plate as we move further from the input over a range of frequencies. When comparing this to the laser scan data we would expect to see a correlation between the two along the far right side of the laser scan plots. It is important to keep in mind that laser scan data does not include the input location, again this is due to limitations on the range of the linear motors as discussed earlier. When comparing the two sets of data the contour plot generated from the single point data should be compared at around 5mm. As one would expect the correlation between these results is very good.

The laser scan data should then be compared to the simulation results for the same frequencies. Again we see that there is a discrepancy between the displacement pattern obtained from simulation and those from the experimental results. This variation can be reasonable expected from the voltage frequency response and occurs for the same reasons.

Additionally it should be noted that the laser scan results do not, for the most part, correspond to the peaks observed in the voltage frequency response graph. The reason for this is a problem that was encountered with the reflective spray paint applied to the PZT plate to obtain a better signal from the laser. This was done after obtaining poor reflection results using just the plain PZT. However, after

several scans were done consisting of several thousands of repetitions, the spray paint layer began to separate from the PZT plate, forming small bubbles which tended to scatter the incoming laser resulting in very poor results in the later runs. These runs have been omitted because they provided no useable data and unfortunately included these optimum frequencies. Therefore the early scans which produced the best results have been presented and still serve to show the evanescent properties of the plate at low frequencies and also a reasonable approximation of the simulation results at these same frequencies.

Laser scan results obtained for the input voltage case appear to provide a closer match to the simulation data. This result is not entirely unexpected since this setup eliminates vibrations that are entering the plate from the sides after travelling around the mounting assembly as well as the evanescence of the plate shape. This again suggests that there are non-ideal conditions, such as unintended energy transfer through the mounting assembly and vibration modes that may be introduced by the overall structural assembly when excited by an input displacement.

The results that have been shown are all based on applying an input displacement at the narrow end of the device. This was done since the model used is the cochlear and there the input is applied at the input. However given the evanescent effect seen when applying an input at the narrow end one further simulation was performed showing the displacement pattern at resonant frequencies when the device is drive from the wide end. The results are shown in Figure 64. The results show that when driving the device from the narrow end we can reduce the low frequency evanescent cut-off to below 1000 Hz. Had additional time been available it would have been interesting to further pursue this alternate configuration. This would require a new mounting assembly to be created to accommodate the actuator attachment at the wide end of the device.
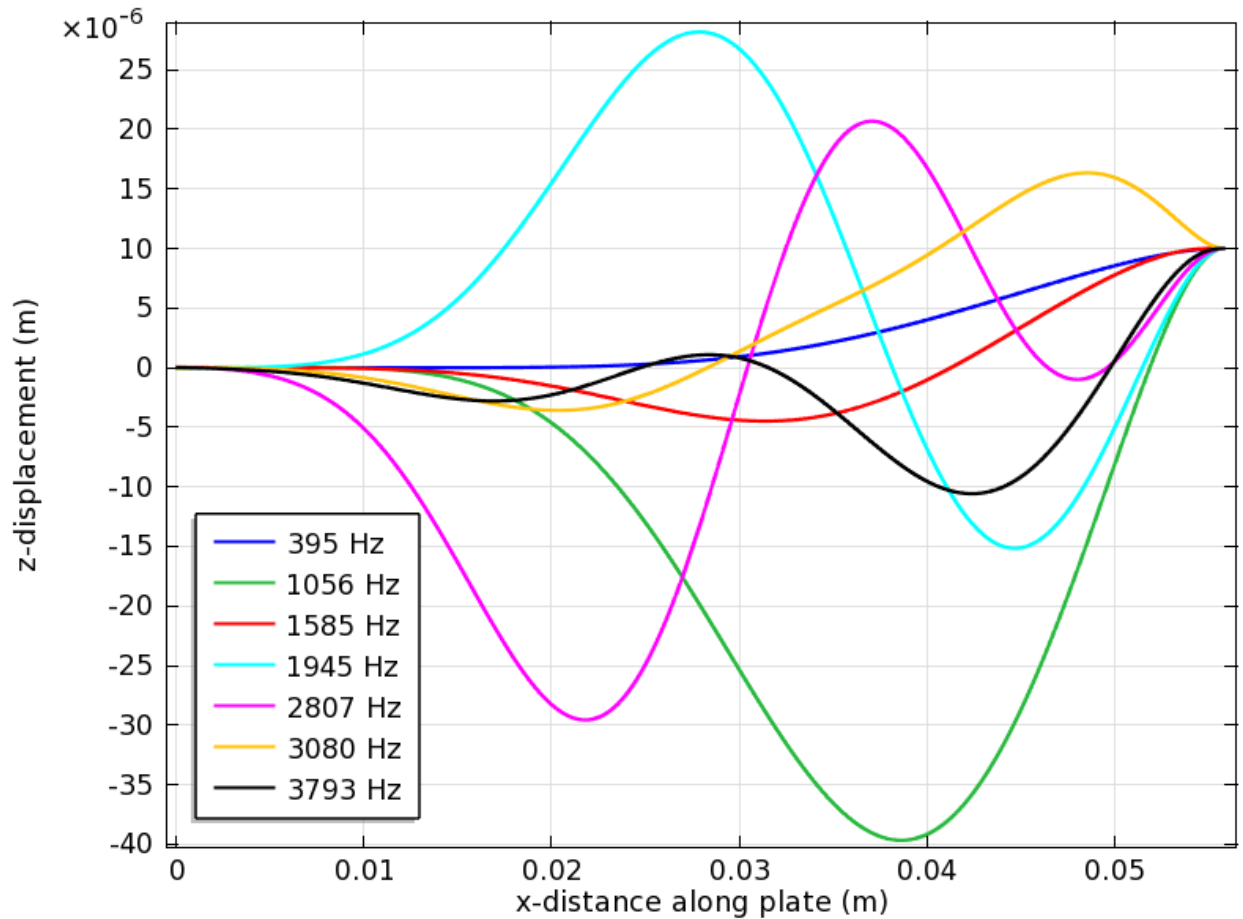
Figure 64 Displacement pattern when driven from wide end

The power output data was obtained for a wider range of frequencies than has been presented in the results section. These were split into four separate plots based on the large difference in magnitude of the resulting power output. As can be seen from the initial voltage frequency response, the voltage output at low frequencies due entirely to the direct input displacement is larger than that at higher frequencies. It is however interesting to note that the next best frequency in terms of power output is approximately 3357Hz. The power output plots shown can clearly been seen to correspond to the peaks in the voltage frequency response graph and confirm that the results obtained are consistent although they do not match the predicted simulation results particularly well. It could be that this is nearing the

frequencies at which the evanescent effect begins to lessen although the effect of vibrations transmitted through the mounting assembly at higher frequencies did not allow for higher frequencies to be investigated.

The maximum power generated from the plate at the frequencies investigated was 6.34 µW which is quite low for a plate of this size although this is not unreasonable as the displacements throughout most of the plate were also quite low. Suggesting that using a clamped plate in this configuration may not be ideal as a vibration energy harvester device. Table 8 shows a comparison of power outputs achieved by others using a variety of device structures.

Author	General shape	Volume	Power	Normalized Power
R. Aryanpur and R. White [36]	Two bimorph cantilever beams	0.153 cm^3	0.213 mW/g^2 @39kΩ & 20 Hz, not rectified	1.38 mW/g^2/cm^3
Kim *et al* [17]	Cymbal	0.661 cm^3	0.124 mW/g^2 @ 400kΩ & 100Hz, not rectified	59 mW/g^2/cm^3
S. Roundy and P.K Wright [3]	Bimorph cantilever beam with tip mass	0.023 cm^3	0.06 mW/g^2 @ 120 Hz, rectified	5.8 mW/g^2/cm^3
M. Reske-Nielsen and R. White 2012	Exponentially tapered bimorph plate	0.436 cm^3	1.09 µW/g^2 @ 4.6kΩ & 129 Hz, not rectified	2.5 µW/g^2/cm^3

Table 8 Power output comparison to piezoelectric energy harvesters in literature

Chapter 5   Conclusions and Future Work

5.1 **Conclusions**

In this thesis an exponentially tapered piezoelectric plate was investigated as a potential new design for use as a broad spectrum vibration energy harvester. First a structural model was developed for the tapered plate and compared with a structural FEA analysis of the device. It was determined that the frequencies under investigation produced evanescent waves in the device and the desired frequency response was not being generated due to this effect. This cut-off frequency was determined to be around 1500 Hz in the structural analysis which corresponds to the 3rd resonant mode of the plate.

Next the FEA analysis was repeated, this time including the piezoelectric effect, it was shown that the introduction of the piezoelectric effect has a significant effect on the evanescent cut-off frequency. The evanescent cut-off frequency was shown to have shifted to be around 3800 Hz which corresponds to the7th resonant mode of the plate. This is a significant difference in the response of the plate and has important implications for future work. The piezoelectric effect cannot be omitted during optimization of the plate shape and material properties even though this will lead to a significant increase in the time required to run FEA analysis or other optimization routines.

The experimental portion of the thesis describes the mounting system used to test the real response of an exponentially tapered piezoelectric plate. This was achieved by machining two exponentially tapered clamping plates into which the square PZT sheet could be mounted and clamped to mimic the fixed exponentially tapered sides. This setup proved to function well and the experimental results provided a good match to the piezoelectric FEA results obtained and showed the evanescence seen in simulation. Furthermore, we were able to show that the frequency response of the exponentially tapered

plate will produce the desired displacement pattern when a sinusoidal voltage is applied. Therefore, if the energy transmitted through the mounting assembly can be limited by using a thinner, less stiff piezoelectric material, damping the mounting assembly's connection to the mounting structure or by increasing the stiffness of the mounting assembly plates it should be possible to apply an input displacement and harvest energy and a number of different frequencies using this type of structure.

As dictated by the presence of the low-frequency evanescent cut-off the power generated by the device was quite low, the peak being 2.5 $\mu W/g^2/cm^3$. However the full potential of the design was not seen, primarily due to the evanescent coupling, and it is still reasonable to assume that it might be possible to use the exponentially tapered shape to generate a cochlea like frequency response in a piezoelectric vibration energy harvester, particularly with the inclusion of a fluid to act as second coupling medium analogous to the cochlear fluid. This is absolutely critical in order to avoid the evanescent cut-off that was the primary feature of the system investigated here.

5.2 Remaining Issues and Future Works

While the results generated did not provide a better alternative to existing piezoelectric energy harvesters, this is only the first case of experimentation with exponentially tapered plates for this application. It would be useful to develop a mathematical model for predicting the evanescent cut-off frequency for an exponentially tapered plate of varying dimension. Then it would be possible to predict the exact size and thickness required in order to fully investigate whether a cochlea like frequency response is achievable in a vibration energy harvester. Another possibility is to change the input method. In this work the application of force to the plate was greatly simplified from what happens in the cochlea. There the energy is first transmitted to a fluid filled chamber and the energy is then transferred from the fluid to the basilar membrane, again this might achievable using piezopolymer if the device can be made significantly thinner and a fluid chamber or analogous structure must be included.

In a case where fluid coupling was included it might be possible to use this type of device on a train where the vibrations during movement of the train would vary significantly and a narrow band energy harvester would largely go unused. One possible configuration of such a device would be an exponentially tapered plate fixed inside of a fluid chamber. The housing of the device would be mounted on damped supports and a rigid support would be fixed at the input to the device. The damped supports would serve to keep the device itself stationary while a rigid input displaced only the input area, equivalent to the stapes in the in the cochlear. In this way different frequencies of ambient vibrations would cause maximum displacements at different distances along the length of the tapered plate and allow for wider band energy harvesting than would be possible using a cantilever device.

A large area PZT plate such as the one used should be capable of generating a large amount of power and if the right design can be found it could provide a method to obtain useful amounts of power from a wide range of ambient frequencies rather than simply being tuned to a single frequency as is so often the case with vibration energy harvesters.

The experimental work generally validated the modeling approaches, although some additional work on boundary conditions may be needed. Furthermore given the results obtained from simulation when the device was driven at the wide end (Figure 64), it would be interesting to recreate the experiments for this configuration.

Appendix A MATLAB Code

A.I   Finite Difference Solution

Contents

Plots frequency response for 4th order lateral beam vibration equation

Note: omega has been defined as global in built-in bvp4c function

```
function FiniteDifference
```

Clear Screens

```
clc
close all
```

Define constants and global variables

```
global omega rho nu E b0 bf alpha L1 P ma h
rho = 7800; %Density (kg/m^3)
nu = .33; %Poisson's ratio
E = 6.2E10; %Young's Modulus (N/m^2)
b0 = 9.4e-3; %Initial Width (m)
bf = 71.12e-3; %Final Width (m)
h = .254e-3; %Thickness (m)
L1 = 55.88e-3; %Beam leangth (m)
alpha = (1/L1)*log(bf/b0); %Variation factor
ma = rho*h; %Mass per unit area (kg/m^2)
P = 1e-5; %Displacement (m)
Freq = 100; %Frequency (Hz)
omega = 2*pi*Freq; %Frequency (rad/s)
```

Run bvp4c function to numerically solve differential equation

```
X = linspace(0,L1,500);
options = bvpset('Stats','off');
solinit = bvpinit(X,[1 0 0 0]);
sol = bvp4c(@ODEFUN,@BCFUN,solinit,options);
x i = 1;
```

Format results for plotting

```matlab
NumIncrement = size(sol.y(1,:),2);
newX = linspace(0,L1,NumIncrement);
b_i = 1;
for x = newX
    bx(b_i) = b0*exp(alpha*x);
    b_i = b_i + 1;
end
for x = newX
    y_i = 1;
    for y = linspace(-bf/2,bf/2,NumIncrement);
        if (y < (0 - bx(x_i)/2)) || (y > bx(x_i)/2)
            psi(y_i,x_i) = 0;
            a = 0;
        else
            psi(y_i,x_i) = cos(pi*y/bx(x_i));
            b = 0;
        end
        y_i = y_i + 1;
    end
    x_i = x_i + 1;
end
u_i = 1;
for u = sol.y(1,:)
    Mat(:,u_i) = psi(:,u_i)*sol.y(1,u_i);
    u_i = u_i + 1;
end
```

Plot Results

```matlab
newY = linspace(-bf/2,bf/2,NumIncrement);
figure
mesh(newX,newY,Mat)
figure
plot(linspace(0,L1,size(sol.y(1,:),2)),sol.y(1,:))
end
```

Set up differential equation

Converts fourth order vibration equation to four first order equations

```matlab
function dudx = ODEFUN(x,u,omega)
global omega rho nu E b0 bf alpha L1 P ma h
% Define exponential variation
b = b0*exp(alpha*x);
psi1 = 3*b/8; %2*b/pi;
psi2 = pi^2/(2*b); %-pi*2/(b);
psi3 = 2*pi^4/(b^3); %(2*pi^3)/b^3;
psi4 = psi1;
D = (h^3*E)/(12*(1 - nu^2));
beta = (ma*omega^2*psi4)/D;
%Convert fourth order differential equation to 4 first order equations
    dudx = [u(2)
        u(3)
        u(4)
        (2*psi2*u(2) + (psi3 - beta)*u(1))/psi1
        ];
end
```

Set Boundary Conditions

```matlab
function res = BCFUN(ua,ub)
%Defines boundary conditions for fourth order vibration equation
%Fixed-Free
global omega rho nu E b0 bf alpha L1 P
%Define boundary conditions
res = [ua(1)-P
       ua(2)
       ub(1)
       ub(2)
       ];
end
```

A.II   Voltage/Input Acceleration vs. Frequency

Contents

Clear Screens

```
clc
close all
```

Load Data

```
load Volt1.txt
load Volt2.txt
```

Define constants

```
VelFactor = 100; %(V/m/s)
```

Define Variables

```
freq = Volt2(:,1); %(Hz)
Voltage = Volt2(:,4); %(V)
Velocity = Volt2(:,5)./VelFactor; %Convert voltage signal to velocity (m/s)
Accel = Velocity.*freq; %Convert velocity to acceleration (m/s^2)
Disp = Velocity./freq; %Convert velocity to displacement (m)
```

Voltage plot

```
figure
plot(freq,20*log(Voltage./Accel),'b','LineWidth',4)
axis([100 3200 -200 -40])
title('Voltage/Input Acceleration vs Frequency (Experimental)')
xlabel('Frequency (Hz)')
ylabel('Voltage/Input Acceleration vs Frequency (dB V/m/s^2)')
```

Acceleration, Velocity and Displacement plots

```
figure
subplot(3,1,1)
plot(freq,Accel,'r','LineWidth',2)
axis([100 3200 0 3])
title('Input Acceleration vs. Frequency (Experimental)')
xlabel('Frequency (Hz)')
ylabel('Input Acceleration (m/s^2)')

subplot(3,1,2)
plot(freq,Velocity,'c','LineWidth',2)
axis([100 3200 0 0.02])
title('Input Velocity vs. Frequency (Experimental)')
xlabel('Frequency (Hz)')
ylabel('Input Velocity (m)')

subplot(3,1,3)
semilogy(freq,Disp,'g','LineWidth',2)
axis([100 3200 10e-9 10e-4])
title('Input Displacement vs. Frequency (Experimental)')
xlabel('Frequency (Hz)')
ylabel('Input Displacement (m)')
```

A.III   Displacement and Acceleration Plots

Contents

- [Clear Screens](#)
- [Define constants](#)
- [Load data and define variables](#)
- [Smooth data and remove noise](#)
- [Plot Displacement](#)
- [Create Contour Plot](#)

```
% Loads and plots center line displacements at various distances from input
```

Clear Screens

```
clc
close all
```

Define constants

```
numData = 5;
VelFactor = 100; %(V/m/s)
LaserFactor = 5e-3; %(m/s/V)
filename_base = 'L';
filename_ext = '.txt';
Distance = [0 .25 1 1.5 2];
endplot = 2080;
distconv = 0.0254; %Convert inches (in) to meters (m)
```

Load data and define variables

```
for cnt = 1:numData
    L = load([filename_base num2str(cnt) filename_ext]);
    freq = L(:,1);
    VelLaser(:,cnt) = L(:,4).*LaserFactor; %Converts laser data to velocity
(m/s)
    VelInput(:,cnt) = L(:,5)./VelFactor; %Converts impedance head data to
velocity (m/s)
    DispLaser(:,cnt) = VelLaser(:,cnt)./freq; %Converts laser velocity to
displacement (m)
    DispInput(:,cnt) = VelInput(:,cnt)./freq; %Converts impedance head
velocity to displacement (m)
end
```

Smooth data and remove noise

```
windowSize = 100;
SMD1 = filter(ones(1,windowSize)/windowSize,1,DispLaser(:,1));
SMD2 = filter(ones(1,windowSize)/windowSize,1,DispLaser(:,2));
SMD3 = filter(ones(1,windowSize)/windowSize,1,DispLaser(:,3));
SMD4 = filter(ones(1,windowSize)/windowSize,1,DispLaser(:,4));
SMD5 = filter(ones(1,windowSize)/windowSize,1,DispLaser(:,5));
```

Plot Displacement

Create single plot showing frequency response at each distance

```
figure
semilogy(freq,SMD1,'b')
title('Displacement vs. Frequency at multiple points')
xlabel('Frequency (Hz)')
ylabel('Displacement (m)')
hold on
axis([100 3200 0 3e-4])
semilogy(freq,SMD2,'r')
semilogy(freq,SMD3,'c')
semilogy(freq,SMD4,'m')
semilogy(freq,SMD5,'g')
legend('x = 0in','x = 0.25in','x = 1.0in','x = 1.5in','x = 2in')
```

Create Contour Plot

Combine data and create contour plot

```
z =
cat(2,SMD1([1:endplot]),SMD2([1:endplot]),SMD3([1:endplot]),SMD4([1:endplo
t]),SMD5([1:endplot]));
figure
[C,h] = contourf(Distance*distconv,freq(1:endplot),log10(z),50);
axis([(-.1)*distconv 2.1*distconv 100 3200])
title('2D Displacement plot as function of Distance from input and
frequency (log (m))')
xlabel('Distance from input (in)')
ylabel('Frequency')
colorbar
```

A.IV 2D plots of displacement obtained from laser scan for Input Acceleration

Contents

- [Clear Screens](#)
- [Define Constants](#)
- [Load Data](#)
- [Format Data for plotting](#)
- [Make Plots](#)
- [Automatically Save Figures](#)

```
% Loads and plots laser scan data
```

Clear Screens

```
clc
close all
```

Define Constants

```
velSF=5e-3;  %Laser scale factor (mm/s/V)
%micSF= 1;%4.19e-3; %Mic scale factor (V/m/s)
numXsteps=50;  %Number of positions
numYsteps=50; %Number of positions across
thresh=-1; %Throw out data for signal level less than this value (V)
filename_base='Disp1_';
filename end='.txt';
max_position=0;  %This is the position when X=0 (mm) Plotted position is
max_position-X
X=zeros(numXsteps+1,numYsteps+1);
Y=zeros(numXsteps+1,numYsteps+1);
S=load([filename base '0 0' filename end]);
numfreqs=size(S,1); %Number of frequencies run
%Define data matrices to improve performance
f=zeros(numfreqs,numXsteps+1,numYsteps+1)*NaN;
rms0=zeros(numfreqs,numXsteps+1,numYsteps+1)*NaN;
rms1=zeros(numfreqs,numXsteps+1,numYsteps+1)*NaN;
deg=zeros(numfreqs,numXsteps+1,numYsteps+1)*NaN;
siglev=zeros(numfreqs,numXsteps+1,numYsteps+1)*NaN;
```

Load Data

```matlab
for cnt=1:numXsteps
    for cnt2=1:numYsteps
        S=load([filename_base num2str(cnt-1) '_' num2str(cnt2-1)
filename_end]);
        f(:,cnt,cnt2)=S(:,1);
        rms0(:,cnt,cnt2)=S(:,2);   %Now in m/s
        rms1(:,cnt,cnt2)=S(:,3)*velSF; %Now in m/s
        deg(:,cnt,cnt2)=S(:,4)*180/pi;
        X(cnt,cnt2)=mean(S(:,5)); %max_position-mean(S(:,5));
        Y(cnt,cnt2)=mean(S(:,6));
        siglev(:,cnt,cnt2)=S(:,7);
    end
end
```

Format Data for plotting

```matlab
%Put in a dummy line of data at the edge so it plots all the data instead
%of N-1 (Matlab pcolor faceted command)
cnt=numXsteps+1;
for cnt2=1:numYsteps
    X(cnt,cnt2)=2*X(cnt-1,cnt2)-X(cnt-2,cnt2);
    Y(cnt,cnt2)=2*Y(cnt-1,cnt2)-Y(cnt-2,cnt2);
end
cnt2=numYsteps+1;
for cnt=1:numXsteps
    X(cnt,cnt2)=2*X(cnt,cnt2-1)-X(cnt,cnt2-2);
    Y(cnt,cnt2)=2*Y(cnt,cnt2-1)-Y(cnt,cnt2-2);
end
cnt=numXsteps+1;
cnt2=numYsteps+1;
X(cnt,cnt2)=2*X(cnt-1,cnt2-1)-X(cnt-2,cnt2-2);
Y(cnt,cnt2)=2*Y(cnt-1,cnt2-1)-Y(cnt-2,cnt2-2);
%Throw out bad data:
rms1(siglev<thresh)=NaN;
%Complex ratios:
velperPa=((rms1)./(rms0)).*exp(1j*deg*pi/180); %m/s
for cnt1=1:numfreqs
    for cnt2=2:numXsteps-1
        for cnt3=2:numYsteps-1
            if isnan(rms1(cnt1,cnt2,cnt3))

velperPa(cnt1,cnt2,cnt3)=mean([squeeze(velperPa(cnt1,[cnt2-1
cnt2+1],cnt3)) squeeze(velperPa(cnt1,cnt2,[cnt3-1 cnt3+1]))']);
            end
        end
    end
end
dispperPa=velperPa./(1j*f*2*pi); %m
```

Make Plots

```matlab
%Displacement:
for cnt=1:numfreqs
    h(cnt)=figure;
    set(gca,'Linewidth',2,'fontsize',12,'fontweight','bold')
    mag=squeeze(abs(dispperPa(cnt,:,:)));
    pcolor(X,Y,mag)
    title([num2str(round(f(cnt,1,1))) ' Hz, m'])
    ylabel('Position (mm)')
    xlabel('Position (mm)')
    colorbar
end
```

Automatically Save Figures

```matlab
%Save figures if you want:
for cnt=1:numfreqs
    figure(h(cnt))
    fname=[filename_base 'Mag' num2str(round(f(cnt,1,1))) 'Hz'];
    saveas(gcf,fname,'png')
    saveas(gcf,fname,'fig')
end
```

A.V   2D plots of displacement obtained from laser scan for Input Voltage

Contents

```matlab
% Loads and plots laser scan data
clc
close all
```

Define Constants

```matlab
velSF=5e-3;  %Laser scale factor (mm/s/V)
numXsteps=50;  %Number of positions
numYsteps=50; %Number of positions across
thresh=-1; %Throw out data for signal level less than this value (V)
filename_base='Half1_';
filename_end='.txt';
max_position=0;  %This is the position when X=0 (mm) Plotted position is
max_position-X
X=zeros(numXsteps+1,numYsteps+1);
Y=zeros(numXsteps+1,numYsteps+1);
S=load([filename_base '0_0' filename_end]);
numfreqs=size(S,1); %Number of frequencies run
%Define data matrices to improve performance
f=zeros(numfreqs,numXsteps+1,numYsteps+1)*NaN;
rms0=zeros(numfreqs,numXsteps+1,numYsteps+1)*NaN;
rms1=zeros(numfreqs,numXsteps+1,numYsteps+1)*NaN;
deg=zeros(numfreqs,numXsteps+1,numYsteps+1)*NaN;
siglev=zeros(numfreqs,numXsteps+1,numYsteps+1)*NaN;
```

Load Data

```
for cnt=1:numXsteps
    for cnt2=1:numYsteps

        S=load([filename_base num2str(cnt-1) '_' num2str(cnt2-1)
filename_end]);
        f(:,cnt,cnt2)=S(:,1);
        rms0(:,cnt,cnt2)=S(:,2);  %Now in m/s
        rms1(:,cnt,cnt2)=S(:,3)*velSF; %Now in m/s
        deg(:,cnt,cnt2)=S(:,4)*180/pi;
        X(cnt,cnt2)=mean(S(:,5)); %max_position-mean(S(:,5));
        Y(cnt,cnt2)=mean(S(:,6));
        siglev(:,cnt,cnt2)=S(:,7);
    end
end
```

Format Data for Plotting

```
%Put in a dummy line of data at the edge so it plots all the data instead
%of N-1 (Matlab pcolor faceted command)
cnt=numXsteps+1;
for cnt2=1:numYsteps
    X(cnt,cnt2)=2*X(cnt-1,cnt2)-X(cnt-2,cnt2);
    Y(cnt,cnt2)=2*Y(cnt-1,cnt2)-Y(cnt-2,cnt2);
end
cnt2=numYsteps+1;
for cnt=1:numXsteps
    X(cnt,cnt2)=2*X(cnt,cnt2-1)-X(cnt,cnt2-2);
    Y(cnt,cnt2)=2*Y(cnt,cnt2-1)-Y(cnt,cnt2-2);
end
cnt=numXsteps+1;
cnt2=numYsteps+1;
X(cnt,cnt2)=2*X(cnt-1,cnt2-1)-X(cnt-2,cnt2-2);
Y(cnt,cnt2)=2*Y(cnt-1,cnt2-1)-Y(cnt-2,cnt2-2);
%Throw out bad data:
rms1(siglev<thresh)=NaN;
%Complex ratios:
velperPa=((rms1)./(rms0)).*exp(1j*deg*pi/180); %m/s
for cnt1=1:numfreqs
    for cnt2=2:numXsteps-1
        for cnt3=2:numYsteps-1
            if isnan(rms1(cnt1,cnt2,cnt3))

velperPa(cnt1,cnt2,cnt3)=mean([squeeze(velperPa(cnt1,[cnt2-1
cnt2+1],cnt3)) squeeze(velperPa(cnt1,cnt2,[cnt3-1 cnt3+1]))']);
            end
        end
    end
end
dispperPa=velperPa./(1j*f*2*pi); %m
```

99

Make Plots

```matlab
%Displacement:
for cnt=1:numfreqs
    h(cnt)=figure;
    set(gca,'Linewidth',2,'fontsize',12,'fontweight','bold')
    mag=squeeze(abs(dispperPa(cnt,:,:)));
    pcolor(X,Y,mag)
    title([num2str(round(f(cnt,1,1))) ' Hz, m/V'])
    ylabel('Position (mm)')
    xlabel('Position (mm)')
    colorbar
end
```

Automatically Save Figures

```matlab
%Save figures if you want:
for cnt=1:numfreqs
    figure(h(cnt))
    fname=[filename_base 'Mag' num2str(round(f(cnt,1,1))) 'Hz'];
    saveas(gcf,fname,'png')
    saveas(gcf,fname,'fig')
end
```

A.VI Power Output

Contents

```matlab
% Loads data and creates contour plot of maximum output power
```

Clear Screens

```matlab
clc
close all
```

Define Constants

```matlab
numData = 14;
filename_base = 'Run';
filename_ext = '.txt';
Resist = [2.1 22.5 47 68.1 99.5 218 328 466 673 991 2160 4610 6800 11800];
```

Load Data

```matlab
for cnt = 1:numData
    L = load([filename_base num2str(cnt) filename_ext]);
    freq = L(:,1);
    VoltOut(:,cnt) = L(:,5); %Output Voltage (V)
    PowerOut(:,cnt) = VoltOut(:,cnt).^2./Resist(cnt);
end
```

Create Contour Plot

```
figure
[C,h] = contourf(log10(Resist),freq,PowerOut,50);
title('Power Output (W)')
xlabel('Log of Resistance')
ylabel('Frequency (Hz)')
colormap('default')
colorbar
axis([1.5 log10(max(Resist)) 100 280])
```

Find Parameters at Max

Find Maximum output power and corresponding resister and frequency values

```
[Val MaxRow] = max(PowerOut);
[MaxPower MaxCol] = max(Val);
MaxResist = Resist(MaxCol)
MaxFreq = freq(MaxRow(MaxCol),1)
MaxPower
```

Published with MATLAB® 7.10

References

1. Erturk, A. and D.J. Inman, *An experimentally validated bimorph cantilever model for piezoelectric energy harvesting from base excitations.* Smart Materials and Structures, 2009. **18**: p. 025009.
2. Kim, M., et al., *Modeling and experimental verification of proof mass effects on vibration energy harvester performance.* Smart Materials and Structures. **19**: p. 045023.
3. Roundy, S. and P.K. Wright, *A piezoelectric vibration based generator for wireless electronics.* Smart Materials and Structures, 2004. **13**: p. 1131.
4. Wang, S.H., et al., *Design and analysis of a unimorph piezoceramic generator with cantilever structure in a low-frequency environment.* Proceedings of the Institution of Mechanical Engineers, Part L: Journal of Materials Design and Applications. **225**(1): p. 11-21.
5. Dallos, P., A.N. Popper, and R.R. Fay, *The cochlea.* 1996: Springer New York:.
6. Geisler, C.D., *From sound to synapse: physiology of the mammalian ear.* 1998: Oxford University Press, USA.
7. Anton, S.R. and H.A. Sodano, *A review of power harvesting using piezoelectric materials (2003-2006).* Smart Materials and Structures, 2007. **16**: p. R1.
8. De Marqui Junior, C., A. Erturk, and D.J. Inman, *An electromechanical finite element model for piezoelectric energy harvester plates.* Journal of Sound and Vibration, 2009. **327**(1): p. 9-25.
9. Mateu, L. and F. Moll, *Optimum piezoelectric bending beam structures for energy harvesting using shoe inserts.* Journal of intelligent material systems and structures, 2005. **16**(10): p. 835.
10. Roundy, S., *On the effectiveness of vibration-based energy harvesting.* Journal of intelligent material systems and structures, 2005. **16**(10): p. 809.
11. Baker, J., S. Roundy, and P. Wright. *Alternative geometries for increasing power density in vibration energy scavenging for wireless sensor networks.* in *3rd Int. Energy Conversion Engineering Conf.* 2005. San Francisco, CA, Aug.
12. Mossi, K., et al., *Harvesting energy using a thin unimorph prestressed bender: geometrical effects.* Journal of intelligent material systems and structures, 2005. **16**(3): p. 249.
13. Danak, A.D., H.S. Yoon, and G.N. Washington. *Optimization of electrical output in response to mechanical input in piezoceramic laminated shells.* in *Proc. ASME Int. Mechanical Engineering Congr.* 2003. Washington, DC, Nov 2003: ASME.
14. Yoon, H.S., G. Washington, and A. Danak, *Modeling, optimization, and design of efficient initially curved piezoceramic unimorphs for energy harvesting applications.* Journal of intelligent material systems and structures, 2005. **16**(10): p. 877-888.
15. Ericka, M., et al. *Energy harvesting from vibration using a piezoelectric membrane.* in *J. Physique. Coll. IV.* 2005.
16. Kim, S., W.W. Clark, and Q.M. Wang, *Piezoelectric energy harvesting with a clamped circular plate: experimental study.* Journal of intelligent material systems and structures, 2005. **16**(10): p. 855.
17. Kim, H.W., et al., *Energy Harvesting Using a Piezoelectric ``Cymbal''Transducer in Dynamic Environment.* Japanese journal of applied physics, 2004. **43**: p. 6178.

18. Adhikari, S., M.I. Friswell, and D.J. Inman, *Piezoelectric energy harvesting from broadband random vibrations.* Smart Materials and Structures, 2009. **18**: p. 115005.

19. Kim, J.E. and Y.Y. Kim, *Analysis of Piezoelectric Energy Harvesters of a Moderate Aspect Ratio With a Distributed Tip Mass.* Journal of Vibration and Acoustics, 2011. **133**: p. 041010.

20. White, R.D., *Biomimetic trapped fluid microsystems for acoustic sensing*, in *Mechanical Engineering.* 2005, University of Michigan: Ann Arbor.

21. Kim, H.S., J.H. Kim, and J. Kim, *A review of piezoelectric energy harvesting based on vibration.* International Journal of Precision Engineering and Manufacturing. **12**(6): p. 1129-1141.

22. Mason, W.P., *Piezoelectricity, its history and applications.* The Journal of the Acoustical Society of America, 1981. **70**: p. 1561.

23. Cross, L.E. and R.E. Newnham, *History of ferroelectrics.* Ceramics and Civilization, 1987. **3**: p. 289-305.

24. Ballato, A. *Piezoelectricity: history and new thrusts*. in *Proc Ultrasonics Symposium, Vol.* . 1996: IEEE.

25. Bechmann, R. *Piezoelectricity-Frequency Control*. in *Proc.18th Annu. Freq. Contr. Symp*. 1964: IEEE.

26. Jaffe, B., R.S. Roth, and S. Marzullo, *Properties of Piezoelectric Ceramics in the Solid-Solution Series Lead Titanate-Lead Zirconate-Lead Oxide: Tin Oxide and Lead Titanate-Lead Hafnate'.* Piezoelectricity, 1992. **5**: p. 159.

27. Lesieutre, G.A., *Vibration damping and control using shunted piezoelectric materials.* The Shock and Vibration Digest, 1998. **30**(3): p. 187-195.

28. Robles, L. and M.A. Ruggero, *Mechanics of the mammalian cochlea.* Physiological reviews, 2001. **81**(3): p. 1305-1352.

29. Johnstone, B.M., R. Patuzzi, and G.K. Yates, *Basilar membrane measurements and the travelling wave.* Hearing Research, 1986. **22**(1): p. 147-153.

30. Main, I.G., *Vibrations and waves in physics*. 1993: Cambridge Univ Pr.

31. Graff, K.F., *Wave motion in elastic solids*. 1975: Dover Pubns.

32. Oden, J.T. and E.A. Ripperger, *Mechanics of elastic structures//(Book).* Washington, D. C., Hemisphere Publishing Corp., 1981. 474 p, 1981.

33. Ventsel, E. and T. Krauthammer, *Thin plates and shells: theory, analysis, and applications*. 2001: CRC.

34. Dodson, J., *Efficient Finite Element Methods/Reduced-Order Modeling for Structural Acoustics with Applications to Transduction.* PhD thesis, University of Michigan, 2001.

35. *Fundamentals of Piezoelectricity and Piezoelectric Actuators.* http://www.physikinstrumente.com/tutorial/4_15.html, [cited 2012 July 1st].

36. Aryanpur, R., *Two Bimorph Piezoelectric Energy Harvester for Vibrations.* Master's of Mechanical Engineering Thesis, 2012. **Tufts University**(School of Engineering).